UC Merced

UC Merced Electronic Theses and Dissertations

Title

Microflow manipulation via symmetries

Permalink

https://escholarship.org/uc/item/5bk6w3w3

Author

Gonzalez, Jeremias Mitchell Garrett

Publication Date

2024

Supplemental Material

https://escholarship.org/uc/item/5bk6w3w3#supplemental

Peer reviewed|Thesis/dissertation

UNIVERSITY OF CALIFORNIA, MERCED

Microflow manipulation via symmetries

A Dissertation submitted in partial satisfaction of the requirements for the degree Doctor of Philosophy

in

Physics

by

Jeremias Mitchell Garrett Gonzalez

Committee in charge:

    Professor Kevin Mitchell, Chair
    Professor Bin Liu, Advisor
    Professor Ajay Gopinathan
    Professor Dustin Kleckner

2024

The Dissertation of Jeremias Mitchell Garrett Gonzalez is approved, and it is acceptable in quality and form for publication on microfilm and electronically:

_____

_____

_____

_____

Chair

University of California, Merced

2024

Dedication

This work is dedicated to my parents, without whom none of this would have been possible.

Everything which is not forbidden by symmetry must occur.

<div style="text-align: right">

Peter Palffy-Muhoray

</div>

Contents

List of Abbreviations

FEM	Finite element method
DOF	Degrees of freedom
CFD	Computational fluid dynamics
PDMS	Polydimethylsiloxane

List of Symbols

x, y, z Cartesian coordinate variables
r   Position vector
$\dot{\gamma}$ Strain rate tensor
u, v, w Flow velocity components
u   Flow velocity vector
p Pressure
r, R Radius of chamber
h, H Height of chamber
I_k Invariant of order k
N Number of independent channels, sources, sinks
f_i Flow rate in a channel i
q_i, m_i Strength of fluid source/sink i
ϕ Flow potential
L   Invariant flow coupling tensor
p_{x_i} Dipole in x_i alignment
$Q_{x_i\text{-}x_j}$ Quadrupole in x_i-x_j alignment
c_i Phase space component of directional flow mode i
ϵ Characteristic strain
t Time
v   Velocity vector
P_i Polynomial of order i
r, θ Planar polar coordinate variables
ω Angular velocity
z Complex number
a_k Interior angle of polygon at vertex k
I   Identity matrix
l Lateral length

List of Figures

Acknowledgements

Curriculum Vita

Education

2016-Present: PhD program, physics, UC Merced
2016: BS in Physics, UC Merced, highest honors

Publications

2024: "Symmetry-group-protected microfluidics", Jeremias Gonzalez, Ajay Gopinathan, Bin Liu. Phys. Rev. Research. In press.
2020: "Bundled slender-body theory for elongated geometries in swimming bacteria", Bin Liu, Jeremias Gonzalez. Phys. Rev. Fluids **5**, 053102.
2020: "Symmetry-based nonperturbative micromanipulation in a three-dimensional microfluidic device", Jeremias Gonzalez, Bin Liu. Phys. Rev. Fluids **5**, 044202.

Research experience

2016-Present: Work with Dr. Bin Liu and Dr. Ajay Gopinathan to create a microfluidic manipulatory device to be used in observation and control of bacterial behavior. This involves simulations and experimental implementation of the device to see the effect on swarming and elucidate the collective motion. A secondary project is in the examination of Moffatt vortices through experiment and simulation to examine their topological nature and their robustness through different geometrical configurations. Further application of these vortices is being made to the perturbation of bacterial swarms.
2016: Work with Dr. Sayantani Ghosh to produce nanoparticle cloaking in the visible spectrum. This involves simulations and experimental synthesis of gold nanoparticles coating a dielectric core to demonstrate the cloaking effect.
2015-2016: Work with Dr. Jay Sharping and Dr. Raymond Chiao to produce simulations of a resonating cavity, first a single cavity and then a double cavity coupled through at least one iris. The simulations of electromagnetic and mechanical resonance guide cavity design choices.

Outreach experience

2016-Present: Work with Dr. Bin Liu to have students from elementary to high school learn about and experience different parts of laboratory research as part of work with the National Science Foundation Center of Research Excellence in Science and Technology, Center for Cellular and Biomolecular Machines (NSF CREST, CCBM). This includes lab tours, talks, demonstration stands, and hands-on engagement with students making their own low-cost, in-lab fabricated microfluidic devices.

Presentations

2023: APS March Meeting Talk, "Real-time micromanipulation through 3D stress-free flows"
2022: APS Division of Fluid Dynamics Talk, " Symmetry-Protected Stressless Microfluidics"
2022: APS March Meeting Talk, "Omnidirectional treadmills on a chip for swimming microorganisms"
2020: APS Division of Fluid Dynamics Talk, "Dynamic 3D velocity control with microfluidic device"
2020: APS March Meeting Talk (Cancelled due to COVID-19), "Devising and characterizing a non-perturbative manipulator in 3D microfluidic channels"
2019: APS March Meeting Talk, "Emergence of cellular vortices in microfluidic devices"
2018: APS Division of Fluid Dynamics Talk, "3D fluid flow manipulation on a microscopic scale"
2018: APS March Meeting Talks, Invited Press and Standard, "Force-free manipulation of microorganisms in a 3D microfluidic channel"
2017: APS Division of Fluid Dynamics Talk, "Non-perturbative manipulation through a 3D microfluidic

treadmill"
2017: APS Far West Talk, "Non-perturbative manipulation through a 3D microfluidic treadmill"

Target Degree

PhD in Physics

Abstract

Microflow manipulation via symmetries

Jeremias Gonzalez

Doctor of Philosophy in Physics

University of California, Merced, 2024

Dr. Bin Liu, Advisor

Dr. Kevin Mitchell, Chair

Microfluidic devices present a versatile means of working with microscale objects. Here we present a new class of microfluidic design and devices that enable control of small objects without the use of traps. The chosen geometry enables symmetry-protected functionality, separating out 3D directional control from straining flow. An experimental implementation of this device allows for strainless, arbitrary path generation both with and without feedback control. Overall, the device provides a new means of micromanipulation to address experimental needs for precise motion and strain control.

Movie `MOV_01.mp4`: The manipulation of a few microscale particles (polystyrene beads of $2\,\mu m$ in diameter) into an equilateral-triangle pattern is visualized under the microscope (in phase contrast at a $60\times$ magnification) with a $188\,\mu m \times 188\,\mu m$ view size. Different particle images correspond to different axial distances of particles to the focal plane. The color shows the trace of a visible particle in time (blue to orange).
Movie `MOV_02.mp4`: The manipulation of a few microscale particles (polystyrene beads of $2\,\mu m$ in diameter) into a square pattern is visualized under the microscope (in phase contrast at a $60\times$ magnification) with a $188\,\mu m \times 188\,\mu m$ view size. Different particle images correspond to different axial distances of particles to the focal plane. The colored traces show the time-lapse images of all visible particles in time (blue to orange).
Movie `MOV_03.mp4`: The manipulation of a few microscale particles (polystyrene beads of $2\,\mu m$ in diameter) into a circular pattern is visualized under the microscope (in phase contrast at a $60\times$ magnification) with a $188\,\mu m \times 188\,\mu m$ view size. Different particle images correspond to different axial distances of particles to the focal plane. The colored traces show the time-lapse images of all visible particles in time (blue to orange).
Movie `MOV_04.mp4`: The manipulation of a few microscale particles (polystyrene beads of $2\,\mu m$ in diameter) into a 3D Lissajous pattern is visualized under the microscope (in phase contrast at a $60\times$ magnification) with a $188\,\mu m \times 188\,\mu m$ view size. Different particle images correspond to different axial distances of particles to the focal plane. The Lissajous pattern rotates at a period of $8\,s$ in the lateral (x'-y') plane while doubling its oscillating frequency (with a period of $4\,s$) in the axial (z') axis. The colored traces show the time-lapse images of all visible particles in time (blue to orange).
Movie `MOV_05.mp4`: The manipulation of a few microscale particles (polystyrene beads of $2\,\mu m$ in diameter) to trace out a microscale "UCM" logo is visualized under the microscope (in phase contrast at a $60\times$ magnification) with a $188\,\mu m \times 188\,\mu m$ view size. Each particle "hops" between disconnected lines by sinking

to another lateral plane before reaching the sites for the next "stroke." Those particles initially close to the focal plane exhibit individual letters "U", "C", and "M" in order (colored in time).

Chapter 1

Introduction

The capacity of the micro-scale realm for solving problems has increasingly been recognized and utilized for a multitude of valuable processes[1, 2]. A necessary component of realizing that capacity is control over micro-objects. Depending on the size of the objects in the micro- and nanoscale range, their composition, and the containing media, a number of mechanisms have been developed to achieve this control. The invention of optical tweezers exploited the use of light to apply force to control objects[3], and has since taken intriguing forms such as using the technique to create micro-hands[4]. Acoustic sources have served as a parallel means of tweezing even single cells[5]. Electrical fields have been used to orchestrate self-assembly of micro- and nanoparticles[6], while magnetic fields have likewise proven able to manipulate micro- and nanostructures with significant dexterity[7].

Still another mechanism has been found in the vast field of microfluidics. Devices within this category present an environment in which small amounts of fluid are channeled as the shape of the environment creates a function. Combinations of focusing channels and pumping can be put together to achieve stable droplets of one fluid inside another[8]. Fluids can be mixed together as they pass through networks of channels[9]. More sophisticated geometries have been used to separate out components of a fluid mixture through microstructures and channel shapes[10]. Geometry itself plays a critical role in providing experimentally desired function. Within the general class of microfluidic devices is a subcategory which uses geometry to enable manipulation of small objects similar to previously mentioned techniques that use various non-fluidic fields.

Within this subcategory there are again different functions enabled by different choices of geometry. Devices have been developed using their geometry to mimic the classic four roll mill device[11], able to impose a strain rate field on the contained objects[12]. Likewise, device geometry possessing the symmetry of a regular polygon has been able to create traps for particles via stagnation points in the flow that can move objects in planar view[13]. More recent work allows an extension of control to full 3D[14]. Such innovations provide a useful version of control over objects using fluid flow fields to complement the existing non-fluidic field techniques. From such work questions naturally arise.

What can be achieved by microfluidics that differentiates their capacity for doing work from similar non-fluidic field controls? For each of the cited microfluidic manipulation examples, particle transport can be achieved, but with that effect comes strain by necessity from the application of flow through the devices. Thus, such microfluidic devices impose force on particles which is important to specimens such as biological samples that are sensitive to force. Optical traps, as one example, likewise impose force to achieve control[15],

and hence this intertwining of positional change and force imposition is a similarity between these examples of fluidic and non-fluidic field control. In Chapter 2 we present a new microfluidic geometry that separates 3D directional functionality from straining functionality without the use of traps, differentiating it from other fluidic and non-fluidic field techniques.

What role does symmetry play in microfluidics that can be leveraged in developing a unique capability for control? Symmetry has been seen to dictate the fluid dynamics of a situation. In the swimming of microorganisms, we have previously shown that an elongated body can be divided into skeleton curves corresponding to key geometric features, and a symmetrical arrangement of those slender bodies can provide an understanding of the resulting fluid dynamics as the abstracted bundle moves through fluid[16]. For the general microfluidic devices mentioned, too, geometry did lead to specific functionality in achieving a physical outcome. The devices designed for manipulation in particular have channel geometry that allows for flow, but the symmetry of those devices requires detailed characterization to determine the resulting flow outcome, difficult to anticipate in advance. In Chapter 2 we present a symmetry-based analysis of the specific geometry discussed to show how its symmetry is purpose-selected to allow for the functionality separation. In Chapter 3 we revisit this idea from a basic perspective, using symmetry groups as a fundamental means of understanding and designing microfluidic devices for physical outcomes. We thus present a new class of microfluidic design and devices that are symmetry-protected in operation.

Having examined these devices, how do they do in actual experimental use? In Chapter 3 we show experimental results with a microfluidic manipulator and generating arbitrary 3D paths using its directional-only functionality. The device is shown while operating without supervision with good adherence to the prescribed paths, as well as with supervision which tightens up the path traversal. In Chapter 4 we discuss the digital control developed to operate the device with a variety of path traversal types all without supervision.

Chapter 2

Symmetry-based non-perturbative micromanipulation in a 3D microfluidic device

In this chapter, a version of published work[17], we introduce a microfluidic design that is desirable for 3D micromanipulation, achieved through a set of double-layer channels with embedded symmetries. For the 6-channel configuration, we show that a zero strain rate at the center of the device is protected by these symmetries, leading to a non-perturbative manipulation flow along any direction in 3D. We visualize such a non-perturbative flow structure through a finite element simulation and confirm this symmetry-protected strain-free condition. In addition to such 3D non-perturbative manipulations, we reveal 2 distinct perturbative flow modes available in this 6-channel device, corresponding to a total of 5 independent modes that agrees with the degree-of-freedom counting. This symmetry-based micromanipulation is fully compatible with conventional microscopes and can be easily extended to other channel geometries for rich biological and physical applications.

2.1   Introduction

Symmetry becomes increasingly important in determining hydrodynamic forces at decreasing length scales. This importance results from the irrelevance of the inertia of fluids at small scales, as characterized by a vanishing Reynolds number in the Stokes regime [18]. For instance, a swimming microorganism needs to exploit non-reciprocal flow structures, e.g., via undulatory or helical motions, that avoid the stagnancy of kinematic reversibility [19]. Also, the symmetry that persists in their swimming strokes dominates the hydrodynamic interactions and synchronizations among multiple swimmers [20]. Despite this importance [21], such roles played by symmetry have been of much less concern in the design of microfluidic devices. Instead, the performance of such devices is often examined directly through computational fluid dynamics [22, 23, 24]. As another important feature arising from the negligible inertia at microscales, the net force around any suspended particles must vanish: any non-zero net force will be overdamped by the instantaneous fluid motion in the limit of the Stokes flow [19, 25]. The perturbation on the suspended particles is thus only due to the finite stress associated with a non-uniform flow structure. In principle, one can utilize a uniform flow to achieve a stressless condition that leads to a surprising regime of nonperturbative manipulations of entrained particles. This regime supplements the available manipulation methodologies, including optical tweezers [26], fluid stress-based remote manipulation techniques [27, 13] and their combination [28].

   A generic way to realize such a nonperturbative manipulation in 3D is through three orthogonal microfluidic channels that form an intersected zone (Fig. 2.1(a)). A superposition of the flow along all three axes generates a flow in any direction within this zone. Provided that such a flow is uniform (similar to that in a wind tunnel), it can be used to move suspended particles without imposing any perturbations in the Stokes regime. However,
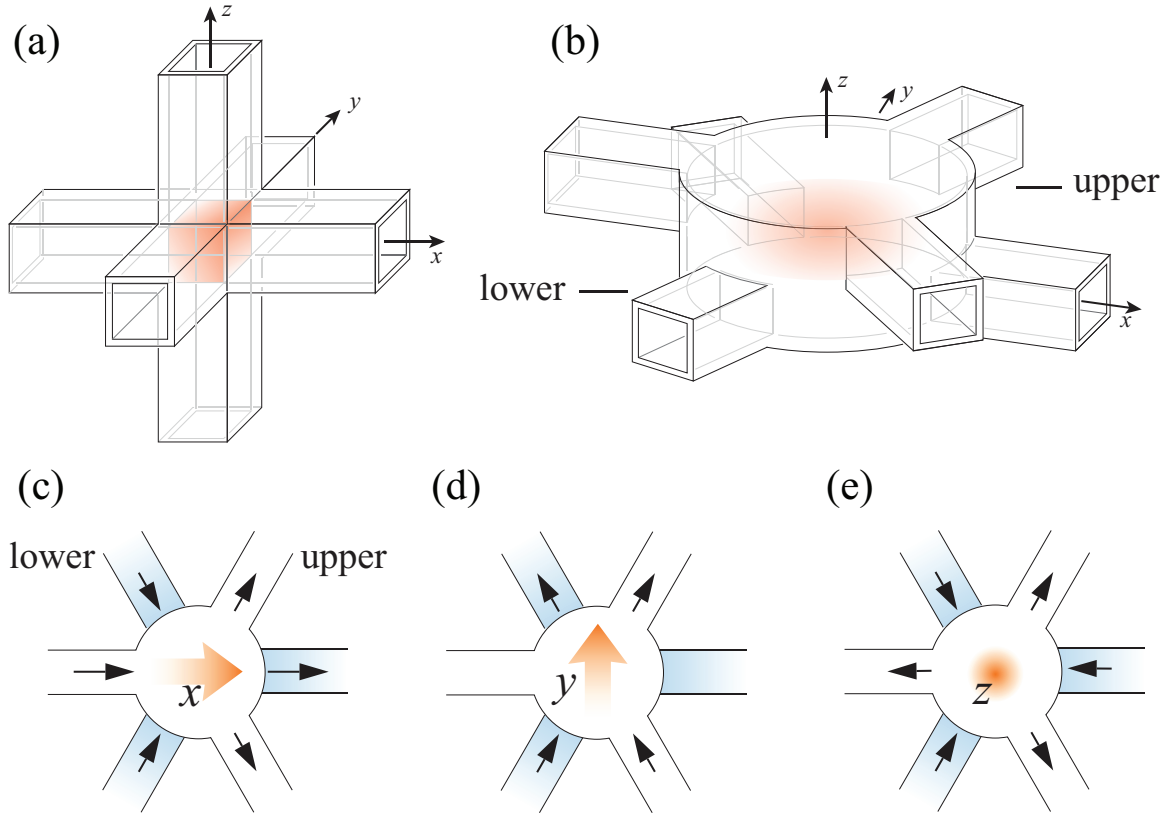
Figure 2.1: Microfluidic designs for 3D non-perturbative manipulations. (a) An orthogonal-channel design allows flow generation in any direction in the intercepted volume (shaded zone), but interferes with the imaging axis. (b) A multi-layer based design of the microfluidic channels accounts for 3D flow generation in the centric region (shaded zone) and is compatible with most microscopes and imaging techniques (along the z-axis). (c)-(e) Three different sets of input flows in the multi-layer channels (upper:white, lower:blue) leads to three orthogonal flows (orange markers) along the x, y, and z axes, respectively.

most of these designs require bulky working spaces associated with the 3D alignments of the microfluidic channels [29, 30, 31]. Such design limits their applications to nonperturbative micro-manipulations, especially to those requiring high spatial and temporal resolutions.

Here, we show a symmetry-based approach to design a 3D nonperturbative manipulation chip that is compatible with most microscopes and microscale imaging techniques. Different from the aforementioned orthogonal-channel design, the 3D flow generation is achieved by incorporating multiple layers of microfluidic channels (Fig. 2.1(b)), which introduce an additional dimension in flow controls. The 6 channels in our present work lie in the x-y plane, intercepted in a center chamber. Relegation of the channels away from the z-axis makes it fully compatible with most conventional microscopes. As the relatively trivial cases, an x- or y-direction flow can be generated by flushing the fluid in all layers along the x- or y- axis, respectively (Fig. 2.1(c) and (d)). To generate an upward z-flow (perpendicular to the x-y plane), flows are converging in all lower channels and diverging in all upper channels, leading to an upwelling net flux (Fig. 2.1(e)). In addition to the generation of flows in any directions, we show both analytically and numerically that the symmetry persisting in the channel geometry and the controlling flow patterns guarantees a zero strain rate at the center of the chip, corresponding to 3D nonperturbative manipulations. We also show that the above strain rate can be manipulated by using the extra degrees of freedom that are available from the design, leading to richer microfluidic applications.

2.2   Symmetry-based design of 3D microfluidic manipulations
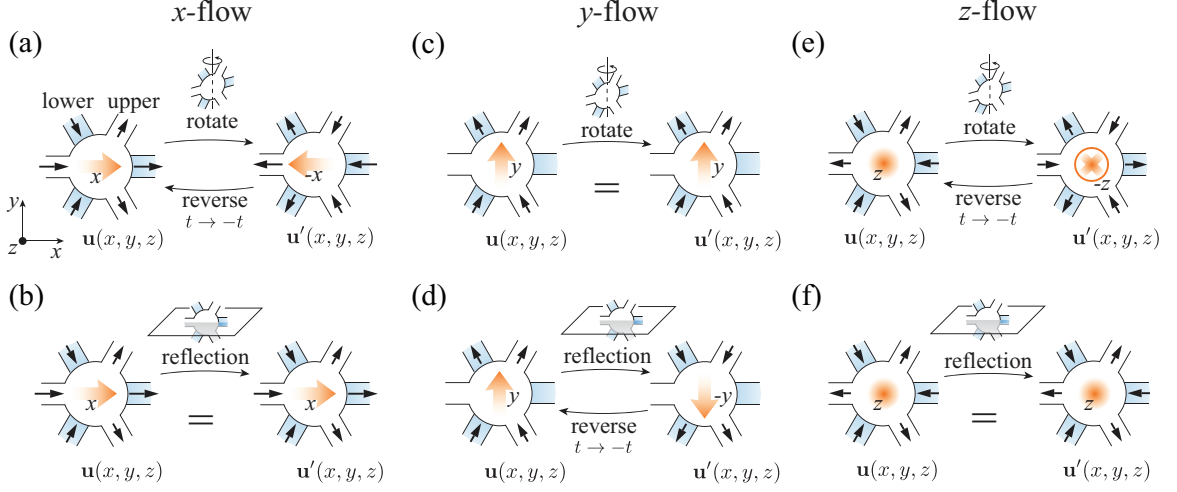
Figure 2.2: Symmetry in the 6-channel 3D microfluidic device. (a) In the x-flow mode, a rotation transformation of $180°$ about the y-axis leads to a reversed velocity field, which can be cancelled by a time reversal. (b) The x-flow mode also contains a reflection symmetry about the $y = 0$ plane. (c) In the y-flow mode, a rotation transformation of $180°$ about the y-axis leads to an identical velocity field. (d) In the y-flow mode, a reflection transformation about the $y = 0$ plane leads to a reversed velocity field, which can be cancelled by a time reversal. (e) and (f), The z-flow mode and the x-flow mode contain the same symmetries, shown in (a) and (b).

We explicitly choose the above 6-channel design for useful symmetries, which is sufficient for maintaining a zero strain rate at the center of the device. Here, we consider a 3D rate of strain tensor $\dot{\gamma}$ at the center of the chamber $\mathbf{r} = (x, y, z) = (0, 0, 0)$ defined as [18]

$$
\dot{\gamma}|_{(0,0,0)} = \begin{pmatrix} \frac{\partial u}{\partial x} & \frac{1}{2}\left(\frac{\partial u}{\partial y} + \frac{\partial v}{\partial x}\right) & \frac{1}{2}\left(\frac{\partial u}{\partial z} + \frac{\partial w}{\partial x}\right) \\ \frac{1}{2}\left(\frac{\partial u}{\partial y} + \frac{\partial v}{\partial x}\right) & \frac{\partial v}{\partial y} & \frac{1}{2}\left(\frac{\partial v}{\partial z} + \frac{\partial w}{\partial y}\right) \\ \frac{1}{2}\left(\frac{\partial u}{\partial z} + \frac{\partial w}{\partial x}\right) & \frac{1}{2}\left(\frac{\partial v}{\partial z} + \frac{\partial w}{\partial y}\right) & \frac{\partial w}{\partial z} \end{pmatrix}\Bigg|_{(0,0,0)} , \tag{2.1}
$$

where $\mathbf{u} = (u, v, w)$ is the flow velocity. The symmetries persistent in all three orthogonal (x-, y-, and z-) flow modes are illustrated in Fig. 2.2.

For the case of the x-flow mode (Fig. 2.1(c)), we consider a sequence of linear transformations to determine the symmetries of the flow velocity. Setting up our coordinate system relative to the center of the chamber, we take the original configuration and rotate the flow about the y-axis by $180°$ (Fig. 2.2(a)). The velocity after this transformation becomes

$$
\mathbf{u}'(x, y, z) = \left(-u(-x, y, -z), v(-x, y, -z), -w(-x, y, -z)\right) . \tag{2.2}
$$

As shown in Fig. 2.2(a), such a transformation simply leads to a reverse of the velocity field. As a consequence, this velocity (Eq. 2.2) can be restored to the original one by applying a time reversal as

$$
-\mathbf{u}'(x, y, z) = \left(u(x, y, z), v(x, y, z), w(x, y, z)\right) . \tag{2.3}
$$

This pair of identities leads to one set of symmetries of the velocity field in the x-flow mode, i.e.,

$$
\begin{cases} u(x, y, z) = u(-x, y, -z), \\ v(x, y, z) = -v(-x, y, -z), \\ w(x, y, z) = w(-x, y, -z). \end{cases} \tag{2.4}
$$

Also, considering the reflection symmetry of the configuration across the $y = 0$ plane (Fig. 2.2(b)), we obtain another set of symmetries of the velocity, i.e.,

$$\begin{cases} u(x, y, z) = u(x, -y, z), \\ v(x, y, z) = -v(x, -y, z), \\ w(x, y, z) = w(x, -y, z). \end{cases} \tag{2.5}$$

With these two sets of symmetries persistent in the velocity field, we determine that all components of the rate of strain tensor vanish at the center of the geometry ($\mathbf{r} = (0, 0, 0)$). For instance, the first identity in Eq.(2.4) leads to $u(x, 0, 0) = u(-x, 0, 0)$ along the x-axis, giving rise to a vanishing $\frac{\partial u}{\partial x}|_{(0,0,0)}$ at the center. Also, the second identity in Eq.(2.4) can be written as $v(0, y, 0) = -v(0, y, 0)$ along the y-axis, giving rise to a null $v(0, y, 0)$, and thus a vanishing $\frac{\partial v}{\partial y}|_{(0,y,0)}$ along the y-axis. All other components of the rate of strain tensor can be determined in the same fashion. After all, the result leads to a null tensor $\dot{\gamma}|_{(0,0,0)} = 0$.

For the case of the y-flow mode (Fig. 2.1(d)), we again consider a sequence of transformations to determine the symmetries of the flow velocity. Taking the original configuration, we rotate the flow about the y-axis by $180°$ (Fig. 2.2(c)). The velocity after the transformation becomes

$$\mathbf{u}'(x, y, z) = \left(-u(-x, y, -z), v(-x, y, -z), -w(-x, y, -z) \right). \tag{2.6}$$

As shown in Fig. 2.2(c), such a transformation simply leads to the original velocity field. This identity leads to a set of symmetries of the velocity field in the y-flow mode, i.e.,

$$\begin{cases} u(x, y, z) = -u(-x, y, -z), \\ v(x, y, z) = v(-x, y, -z), \\ w(x, y, z) = -w(-x, y, -z). \end{cases} \tag{2.7}$$

Next, taking the original configuration we mirror the flow about the $y = 0$ plane (Fig. 2.2(d)). The velocity after the transformation becomes

$$\mathbf{u}' = \left(u(x, -y, z), -v(x, -y, z), w(x, -y, z) \right). \tag{2.8}$$

As shown in Fig. 2.2(d), such a transformation simply leads to a reverse of the velocity field. As a consequence, this velocity can be restored to the original one by applying a time reversal as

$$-\mathbf{u}'(x, y, z) = \left(u(x, y, z), v(x, y, z), w(x, y, z) \right). \tag{2.9}$$

This pair of identities leads to a set of symmetries of the velocity field in the y-flow mode, i.e.,

$$\begin{cases} u(x, y, z) = -u(x, -y, z), \\ v(x, y, z) = v(x, -y, z), \\ w(x, y, z) = -w(x, -y, z). \end{cases} \tag{2.10}$$

As before, these relations show that all components of the rate of strain tensor go to 0 at the center, i.e., $\dot{\gamma}|_{(0,0,0)} = 0$. Finally, the same set of symmetries of the x-flow mode apply to the z-flow mode (Fig. 2.1(e)), and thus give rise to the same zero rate of strain tensor at the center (Fig. 2.2(e) and (f)).

2.3 Numerical simulations of 3D non-perturbative manipulations

To validate the above three modes of manipulation in an actual device, we perform a 3D simulation of the flow field in the 6-channel microfluidic chip by solving an incompressible Stokes equation via the finite element method (FEM),

$$\begin{aligned} \nabla^2 \mathbf{u} - \nabla p = \mathbf{0}, \\ \nabla \cdot \mathbf{u} = 0, \end{aligned} \tag{2.11}$$

where p is the fluid pressure.
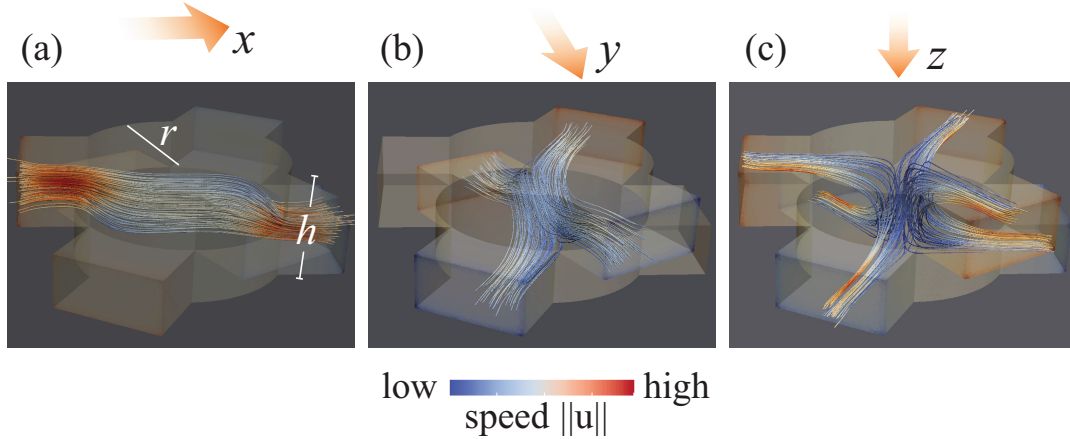
Figure 2.3: The velocity fields of the three orthogonal flow modes from the finite-element simulation. (a) - (c) The characteristic streamlines (colored in flow speed) are shown for x-, y-, and z-flow modes, respectively. Here, the aspect ratio of middle chamber $r/h = 1$. The colors on the domain walls indicate the low- (blue) and high-pressure (orange) regions.

The domain of computation is shown in Fig. 2.3, which is generated by GMSH [32]. A uniform boundary velocity $\mathbf{u}_b$ is prescribed on the opening of each channel and a no-slip boundary condition is applied to all solid walls. The velocity and pressure fields are then solved by the FEM solver FreeFEM++ [33]. Figure 2.3(a), (b), and (c) show the corresponding streamlines (shown in ParaView [34]) for the x-, y-, and z-flow modes, respectively. In each of the three modes, streamlines are parallel near the center, which indicate a uniform manipulation flow along the desired axis.

To quantify the flow velocity at the center $\mathbf{u}_0$ (for any nonperturbative manipulation), we perform the numerical simulation with various radii of the middle chamber and evaluate the corresponding flow speed. Figure 2.4 shows the center flow speed as a function of the aspect ratio (r/h) for each mode, where r and h are the radius and height, respectively. In all three modes, the center flow speed $\|\mathbf{u}_0\|$ (as normalized by the prescribed boundary speed at the channel opening $\|\mathbf{u}_b\|$) decreases monotonically with the increasing aspect ratio of the middle chamber. This decreasing speed compensates for the increasing cross section area (normal to the direction of the flow mode) for larger chamber radius, as required by a fixed net flux.

To validate the above zero rate of strain at the center and show how it varies in space, we compute the rate of strain tensor within the entire simulation domain. Here, the rate of strain $\dot{\gamma}$ is normalized by the characteristic speed ($\|\mathbf{u}_0\|$) and length (r), i.e., $\tilde{\dot{\gamma}} = \dot{\gamma}r/\|\mathbf{u}_0\|$. To avoid the complexity of tracking all 6 independent components of the tensor [18], we characterize the intensity of the rate of strain by its invariants (I_1, I_2, and I_3) [35] that are independent of the choice of coordinate systems,

$$I_1 = \mathrm{Tr}\left(\tilde{\dot{\gamma}}\right), \tag{2.12}$$

$$I_2 = \frac{1}{2}\left(\left(\mathrm{Tr}\left(\tilde{\dot{\gamma}}\right)\right)^2 - \mathrm{Tr}\left(\tilde{\dot{\gamma}}^2\right)\right), \tag{2.13}$$

$$I_3 = \det\left(\tilde{\dot{\gamma}}\right). \tag{2.14}$$

For our case where the fluid is considered incompressible, I_1 is automatically 0, and I_2 reduces to only its second term. By considering the magnitude of I_2 (I_3 behaves similarly), and taking its square root, we get a dimensionless quantity that serves as an intrinsic strain rate for assessing the quality of nonperturbation in the volume of the chamber.

Figure 2.5 shows this intrinsic strain rate $|I_2|^{1/2}$ in the representative x- and z-flow modes. As shown in Fig. 2.5(a) and (b), I_2 is always zero at the origin (or the center of the chamber). This vanishing I_2 is consistent with the conclusion from our earlier symmetry-based arguments, where all components of the rate of strain tensor are strictly zero due to the persistent symmetries. Near this point of zero rate of strain, $|I_2|^{1/2}$ grows
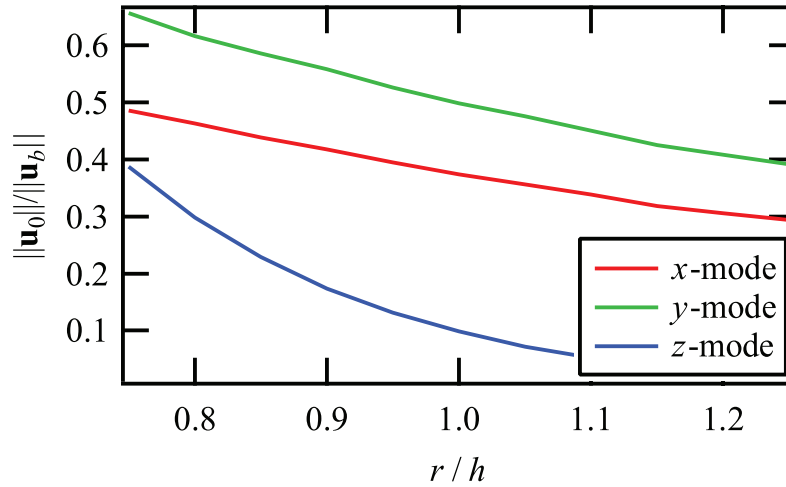
Figure 2.4: The center flow speed $||\mathbf{u}_0||$ normalized by the prescribed speed $||\mathbf{u}_b||$ at the channel opening is shown as a function of the aspect ratio of the middle chamber r/h for x- (red), y- (green) and z-flow (blue) modes.

gradually as an approximately second order dependency on the distance from the origin (Fig. 2.5(c) and (d)). To further characterize the geometries of these low-strain zones near the origin, we show the isosurfaces of these relatively low values of $|I_2|^{1/2}$. In case of the x-flow mode, such an isosurface forms an oval shape with its principal axis lying in the $y = 0$ plane. In case of the z-flow mode, this isosurface is ellipsoid-like at relatively low $|I_2|^{1/2}$, and eventually turns into a double-sided vase that connects the top and bottom boundaries of the middle chamber. Depending on the tolerance of the perturbations, such a low strain rate zone (enclosed by an isosurface of a desired $|I_2|^{1/2}$) provides a working space for effectively nonperturbative manipulations.

2.4   Extra degrees of freedom in flow controls

The above three independent modes of nonperturbative manipulations in our 3D microfluidic device correspond to only three degrees of freedom in our multi-channel configuration. To explore the full capacity in its 3D micromanipulation, we examine all degrees of freedom (DOF) that are available in this device. The number of DOF is in principle equivalent to the number of independent microfluidic channels N. Here, the 6-channel configuration leads to $N = 6$ DOF by considering the fluxes through all channels to be independent. However, the conservation of fluid volume requires the fluxes from these channels to sum up to zero, which leads to a constraint. This leads to the total number of DOF = $N - 1 = 5$, exceeding the 3 independent modes of nonperturbative manipulations corresponding to the x-, y-, and z-flow modes.

Indeed, these two additional DOF correspond to another set of flow manipulations that are embedded with non-zero strain rate at the center of the microfluidic device. Figure 6 shows these two additional perturbative modes, which can be achieved by reversing the flows in one of the two layers of the x- and y-flow modes. We term these two additional configurations the opposing x- and y-flow modes, respectively (Fig. 2.6(a) and (c)). Figure 2.6(b) and (d) show the corresponding flow fields obtained by the FEM simulation. In both cases, the flow domains are visually split into four quadrants by the streamlines, forming a stagnation point at the center of the middle chamber.

To confirm the orthogonality between these two perturbative modes, we compare the rate of strain tensors obtained from their velocity fields. By applying symmetry arguments similar to those in the nonperturbative modes (Fig. 2.2), we can show that the velocity field in both cases satisfy different sets of identities.
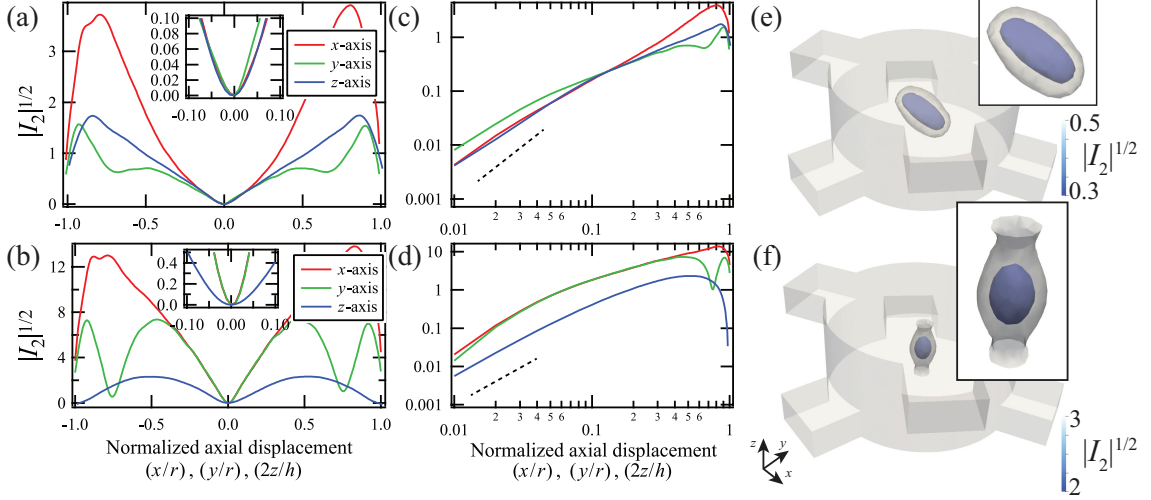
Figure 2.5: Spatial distributions of the intrinsic strain rate $|I_2|^{1/2}$. (a) The distributions of $|I_2|^{1/2}$ along all axes converge to show a zero-strain region at the center in the x-flow mode (with a zoomed-in view as inset). (b) Similar convergence of $|I_2|^{1/2}$ near the center in the z-flow mode. (c) and (d) Log-log versions of (a) and (b) show a quadratic increase (indicated by the dashed lines) of $|I_2|^{1/2}$ away from the center. (e) and (f) The representative geometries of the low strain rate zones are shown in isosurfaces (with their zoomed-in views as insets) for the x- and z-flow modes, respectively.

In the opposing x-flow mode, the symmetries in the velocity lead to

$$\begin{cases} u(x, y, z) = -u(-x, y, -z), \\ v(x, y, z) = v(-x, y, -z), \\ w(x, y, z) = -w(-x, y, -z). \end{cases} \tag{2.15}$$

and

$$\begin{cases} u(x, y, z) = u(x, -y, z), \\ v(x, y, z) = -v(x, -y, z), \\ w(x, y, z) = w(x, -y, z). \end{cases} \tag{2.16}$$

Distinct from the nonperturbative flow modes, these identities restrict the center flow velocity to be zero, i.e., $\mathbf{u}_0 = 0$. Additionally, it can be easily shown that these identities give rise to a number of zero components of the rate of strain tensor at the center of the device, i.e., $\dot{\gamma}_{yz} = \dot{\gamma}_{zy} = \frac{1}{2}\left(\frac{\partial v}{\partial z} + \frac{\partial w}{\partial y}\right) = 0$ and $\dot{\gamma}_{xy} = \dot{\gamma}_{yx} = \frac{1}{2}\left(\frac{\partial u}{\partial y} + \frac{\partial v}{\partial x}\right) = 0$, while leaving the rest of the components finite.

Similarly, in the opposing y-mode, the symmetries in the velocity lead to

$$\begin{cases} u(x, y, z) = u(-x, y, -z), \\ v(x, y, z) = -v(-x, y, -z), \\ w(x, y, z) = w(-x, y, -z), \end{cases} \tag{2.17}$$

and

$$\begin{cases} u(x, y, z) = -u(x, -y, z), \\ v(x, y, z) = v(x, -y, z), \\ w(x, y, z) = -w(x, -y, z). \end{cases} \tag{2.18}$$

In addition to a zero $\mathbf{u}_0$, these identities guarantee a distinct set of zero and non-zero components of the rate of strain tensor at the center from the opposing x-mode, i.e., $\dot{\gamma}_{xz} = \dot{\gamma}_{zx} = \frac{1}{2}\left(\frac{\partial w}{\partial x} + \frac{\partial u}{\partial z}\right) = 0$, $\dot{\gamma}_{xx} = \frac{\partial u}{\partial x} = 0$, $\dot{\gamma}_{yy} = \frac{\partial v}{\partial y} = 0$, and $\dot{\gamma}_{zz} = \frac{\partial w}{\partial z} = 0$.
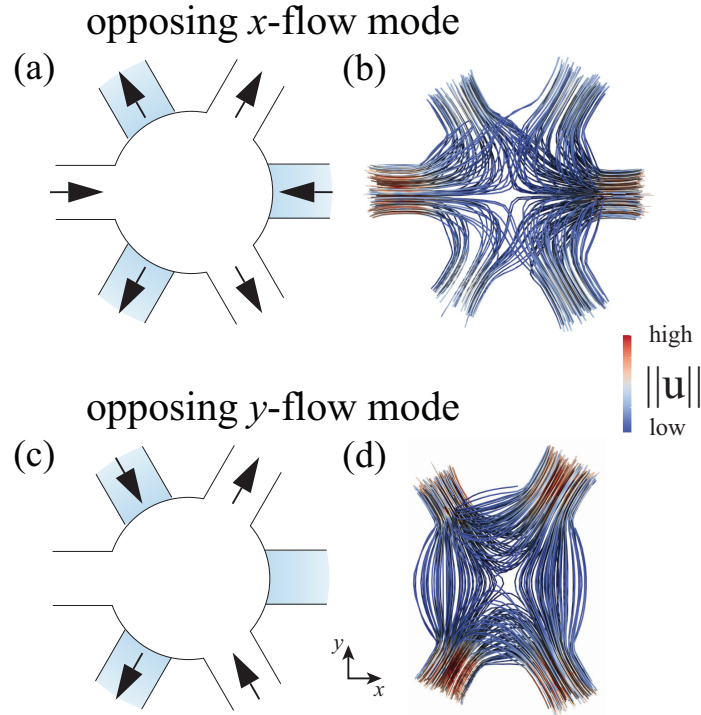
Figure 2.6: Perturbative modes in the 3D 6-channel microfluidic device. (a) Reversing the flows in all lower channels of the x-flow mode (Fig. 2.1(c)) yields a hyperbolic flow at the center of the device, as shown by the corresponding stream lines (b). (c) Reversing the flows in all lower channels of the y-flow mode (Fig. 2.1(d)) yields another type of hyperbolic flow that is stretched along the y-axis, as shown by the corresponding stream lines (d).

These distinct sets of zero components demonstrate the orthogonality between the opposing x- and opposing y-flow mode: the rate of strain tensor from one mode cannot be reproduced by the other.

To validate this orthogonality in the actual 3D device, we compute the above characteristic strain-rate components for various middle chamber geometries. As shown in Fig. 2.7, the normalized component $\tilde{\gamma}_{xz}$ decreases monotonically with increasing aspect ratio of the middle chamber for the opposing x-flow mode (Fig. 2.7(a)) while it is consistently zero within the computational resolution for the opposing y-flow mode (Fig. 2.7(c)). For the $\tilde{\gamma}_{yz}$ component, this time the opposing y-flow mode shows a similar geometric dependency with a monotonic decrease (Fig. 2.7(d)), and the opposing x flow mode is consistently zero (Fig. 2.7(b)). Such binary dependencies of the rate of strain tensor on these two flow modes agree with the orthogonality predicted from the symmetry arguments. These two distinct sets of rate of strain tensor also suggests two types of perturbative manipulations that are available in this microfluidic device.

2.5 Discussion

Our study demonstrates that the symmetries in a 6-channel 3D microfluidic device can be exploited to generate desirable flow structures for nonperturbative micromanipulation. While capable of moving suspended particles along any direction in 3D (through a superposition of 3 orthogonal flow modes), the manipulation flow structure is endowed with a vanishing rate of strain tensor at the center of the working zone. This strain rate also grows quadratically with the distance to the center, which indicates a surprisingly uniform flow as compared to the linear dependency of a parabolic flow that is found in typical microfluidic transport. In addition to these non-perturbative manipulation modes, we illustrate two additional manipulation modes that are accounted for by the degree-of-freedom counting. By analyzing their symmetries, we show that these
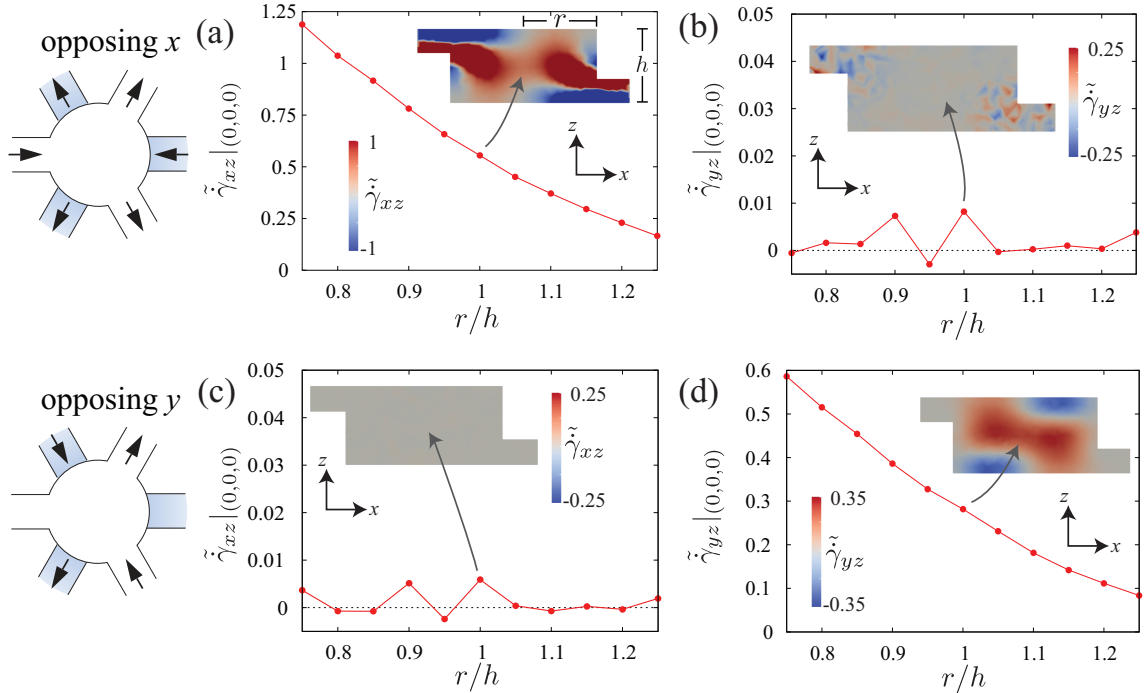
Figure 2.7: Distinct strain-rate characteristics in two perturbative manipulation modes from the FEM simulations. (a) A non-zero component of the rate of strain tensor at the geometric center in the opposing x-flow mode, here $\dot{\gamma}_{xz}|_{(0,0,0)}$, is shown as a function of the aspect ratio (r/h) of the middle chamber. (b) In the same flow mode, the component $\dot{\gamma}_{yz}$ at the geometric center is consistently zero within computation resolutions. (c) The above non-zero $\dot{\gamma}_{xz}$ in the opposing x-flow mode becomes zero in the opposing y-flow mode, regardless of r/h. (d) The above zero $\dot{\gamma}_{yz}$ in the opposing x-flow mode becomes non-zero in the opposing y-flow mode, showing a similar dependency on r/h as in (a). The distribution of $\dot{\gamma}_{xz}$ and $\dot{\gamma}_{yz}$ over the $y = 0$ plane at $r/h = 1$ in each case is shown in the inset. Here, these components of rate of strain tensors are made dimensionless by normalizing $\dot{\gamma}$ with the same factors used in the corresponding x- and y-flow modes, i.e., $\tilde{\dot{\gamma}} = \dot{\gamma}r/||\mathbf{u}_c||$.

two manipulation modes are orthogonal by their rate of strain tensor. Overall, our analysis identifies all 5 orthogonal manipulations (3 for non-perturbative and 2 for perturbative manipulations) in this 6-channel chip, which are potentially useful for different types of microfluidic applications.

So far, only a double-layer chip has been discussed. It is expected that incorporating more layers of channels will introduce richer designs of symmetries for desired flow structures. Meanwhile, the completeness in orthogonal modes here is achieved by trying different combinations of flow directions in all channels and investigating the resultant strain rate through the presented symmetry. A more general approach is desired to recognize such orthogonal manipulation modes, especially for arbitrary number of channels. Our success in the symmetry-based analyses suggests that a map of such a 3D multi-channel device to a symmetry group may lead to all orthogonal modes directly, which will be explored in the future.

The symmetry arguments here are justified by a Stokesian Newtonian fluid. It is expected that such arguments can not be directly applied to a non-Newtonian fluid, e.g., particle suspensions, where the time reversal symmetry typically does not hold. For instance, this time reversal symmetry can be easily broken by the viscoelasticity that emerges in a polymeric suspension [36, 37]. However, from a perturbation-theory point of view, a symmetry-protected zero strain rate also leads to a vanishing polymer stretch and thus a negligible polymeric stress. This implies that our non-perturbative manipulations can be potentially extended to non-Newtonian fluids, especially in the limit of a low concentration of suspended particles.

This multi-layer microfluidic design is fully compatible with conventional microscopes, and can be realized by several microfabrication means [38, 39, 40]. This device can thus be applied to direct manipulation of microparticles that are sensitive to mechanical perturbations, e.g., due to a non-uniform flow [41, 42, 43]. As such, this advanced level of manipulation leads to many biophysical applications in both perturbative and non-perturbative manners.

Chapter 3

Symmetry-group-protected microfluidics for multiplexed stress-free manipulations

Modern micromanipulation techniques typically involve trapping using electromagnetic, acoustic or flow fields that produce stresses on the trapped particles thereby precluding stress-free manipulations. In this chapter, a version of work accepted for publication[44], we show that by employing polyhedral symmetries in a multichannel microfluidic design, we can separate the tasks of displacing and trapping a particle into two distinct sets of flow operations, each characterized and protected by their unique groups of symmetries. By combining only the displacing uniform flow modes to entrain and move targeted particles in arbitrary directions, we were able to realize symmetry-protected, stress-free micromanipulation in 3D. Furthermore, we engineered complex, microscale paths by programming and controlling the flow within each channel in real-time, resulting in multiple particles simultaneously following desired paths in the absence of any supervision or feedback. Our work therefore provides a general symmetry-group-based framework for understanding and engineering microfluidics and a novel platform for 3D stress-free manipulations.

3.1   Introduction

Microfluidics enables the study of the behavior, control, and manipulation of microscale flows typically using device architectures comprising channels and junctions as their building blocks [45, 46, 47, 48]. Desired flow structures and microfluidic functions such as transporting and mixing chemicals [49], shaping flow profiles [50, 51], encapsulating multiphase fluids [52, 53], and trapping microparticles [27, 13] are incorporated through the geometry of these building blocks and the topology of their assemblies [54, 55, 56, 57]. Despite this increased complexity, our understanding of these microfluidic functions is mostly achieved in a case-by-case fashion relying on actual experimental measurements or on computational fluid dynamics (CFD) studies using detailed experimental geometries. A unified framework that allows us to understand how these complex flow structures emerge from simpler, more fundamental flows would prove extremely useful for the fast, modular development of rationally designed flow structures and associated microfluidic functions.

Symmetry is a concept that has been used to understand phenomena and structures in disciplines ranging from fundamental physics to viral structure [58, 59, 60]. In the realm of microscale flows, symmetries are essential features of representative flow structures, such as the helical symmetry in swimming microorganisms [61, 25] and the reflection symmetry applicable in many hydrodynamic interactions [62, 20]. These symmetries have profound implications with helical symmetry giving rise to swimming motility in bacterial species due to the breaking of kinematic reversibility while the reflection symmetries possessed by a pair of microswimmers constrain their synchronization and thus their collective motion. Such considerations applied to microfluidic systems could allow us to uncover very general results independent of system details. Recent work on multi-channel microfluidic junctions and open-space microfluidics have shown that their main flow structures can be obtained from the potential flows around charges representing the channels' ports, without consideration of detailed channel geometries [13, 63]. This simplification has revealed intriguing flow structures that enable

rich microfluidic applications, such as flow-driven traps for particle manipulation and dynamic confinements of fluid into multipole-like networks. Additionally, certain combinations of rotation and reflection symmetries have been applied both analytically and numerically to a multi-port microfluidic junction to eliminate strain components at the junction center, giving rise to potentially perturbation-free micromanipulations [17]. All the above implications of symmetries suggest the feasibility of using a more generalized symmetry-based approach, i.e., the symmetry group, for a more fundamental understanding of the origins of these symmetries and ways to manipulate them for specific functions.
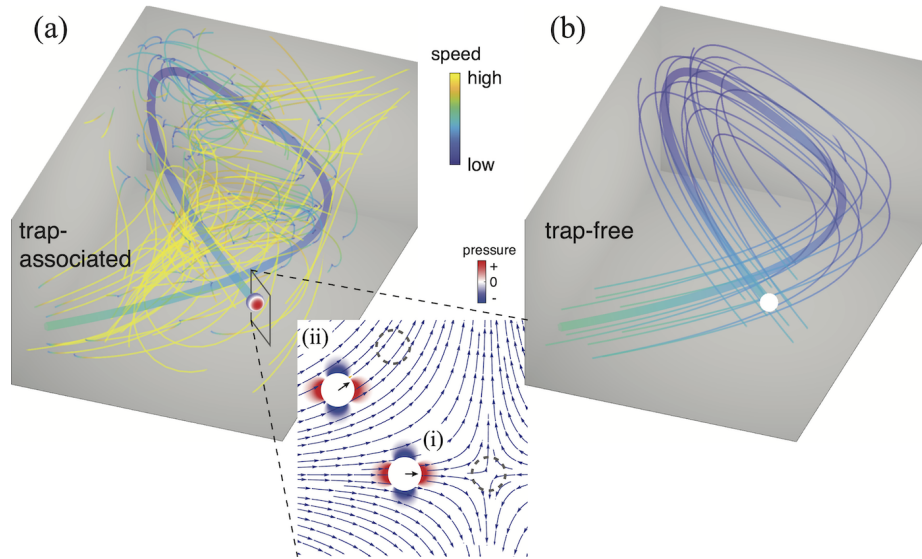
Figure 3.1: Trap-associated v.s. trap-free manipulations of microscale particle through surrounding flows. (a) In trap-associated manipulations, a manipulated particle is led by a fluid "trap" or guided by the local flow director (zoomed-in 2D views (i) and (ii) in the inset, respectively) along the desired pathway (shown in the thick curve), surrounded by overall divergent flows (with speeds of fluid tracers shown in colors) due to its trapping nature. The stress distribution around the particle (with dashed circles showing target positions) is intrinsic to the far-field flow topology (inset), with compression (in red) and extension (in blue) along orthogonal axes, independent of its relative position to the trap. (b) An ideal perturbation-free manipulation is achieved by entraining the particle in a uniform flow field. All surrounding fluid flows in parallel paths at identical velocities and leaves the entrained particle stress-free (in blank color).

One of the most desirable of these microfluidic functions is manipulating flow structures that allow the displacement of individual microscale objects along arbitrary paths [64]. Typically, micromanipulation techniques involve trapping particles using electromagnetic, acoustic, or flow fields that produce restoring forces in the vicinity of the trap [65, 66, 67, 68]. For example, in cases where hydrodynamic flow alone is used for trapping, previous studies have shown that a Stokes trap can be achieved by managing the locations of hyperbolic points through multiple channels that intersect at a middle junction [13]. The location of such a trap can be dynamically adjusted to realize the direct manipulation of trapped particles, which has also been extended to 3D flows very recently [14].

Computation-assisted feedback-control has also enabled manipulations of particles along local flow fields without the explicit employment of a hyperbolic point [69, 64]. The displacements of particles can be adjusted by aligning the local flow field with the moving directions of particles. However, even without the presence of a local hyperbolic point, trapping and displacement are inextricably coupled. As illustrated in Fig. 3.1a, flow fields far from these locally hyperbolic-point-free flows can be divergent, leading to inevitable stress perturbations on any manipulated objects. It is worth noting that the stress distribution on the particle is intrinsic to the far-field hyperbolic topology [70]. Even for a flow field that appears uniform, e.g., within a locally trap-free zone in Fig. 3.1a inset, the stress distribution on the entrained particle is identical to that within the trap, regardless of their relative displacement. These stressful perturbations thus restrict such

approaches to studying stress-insensitive phenomena. Scaling such approaches with traps or local flow vector fields to simultaneously manipulate large numbers of particles is also a challenge. Here, we explore the use of symmetry groups to guide the design of microfluidics that enable multiplexed and stress-free manipulation, which is characterized by a truly uniform flow field around the manipulated particle(s) [Fig. 3.1b]. Distinct from the above locally uniform flows (as exemplified in [69]), the instantaneous flow field here is strictly parallel and straight, avoiding any hyperbolic point in the far field or even outside the microfluidic boundaries (as depicted through symmetries, shown below). Specifically, we identify and characterize microfluidic flow structures based on symmetry groups, which allow us to distinguish and robustly realize fundamentally different microfluidic functions.

3.2 Symmetries in microfluidic systems

3.2.1 2D Microfluidic symmetries

We start with a cross-channel junction for its well-understood microfluidic functions and relatively simple symmetries. Here, the four ports of identical channels (with flow rates $f_i, i = 1, 2, 3, 4$) form a square [Fig. 3.2a], and therefore its flow structures in the plane are restricted by the symmetry of a square. An arbitrary flow pattern generated by a combination of $\{f_i\}$ at this junction corresponds to a set of identical flow manipulations through certain rotations or reflections (Appendix A.2). All such possible rotations or reflections (including the trivial identity operation) form a dihedral-4 (D4) symmetry group [58], which restricts the possible flow patterns. This D4 group thus represents the flow manipulation functions in a cross-channel junction. How
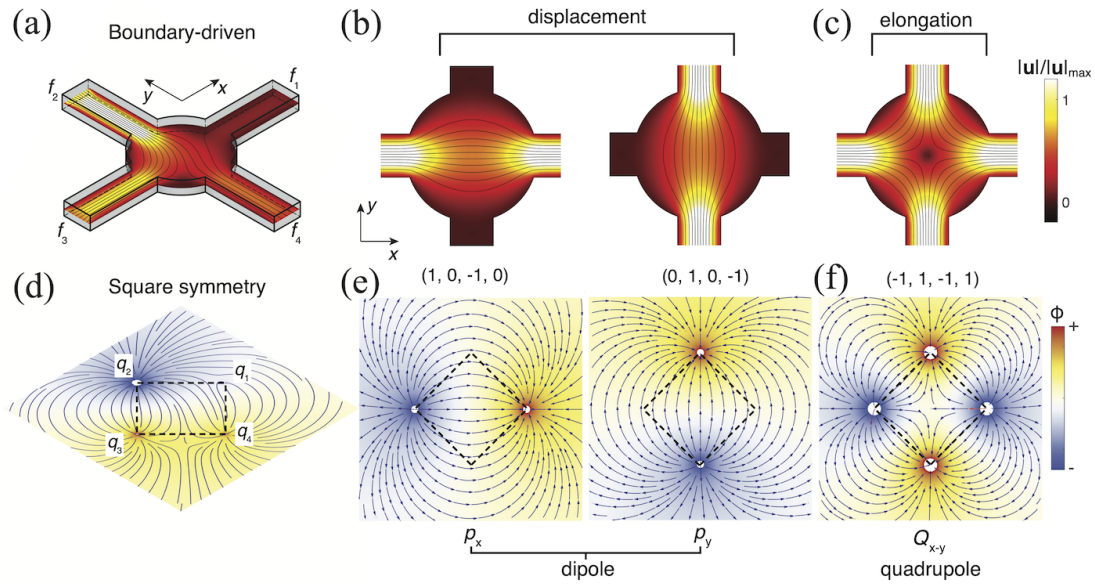
Figure 3.2: Functional classification of a cross-channel microfluidic junction. (a) A 2D CFD simulation of the flow pattern (with streamlines in solid curves and speed $|\mathbf{u}|$ in colors) from an arbitrary flux setting (f_1 - f_4 at four ports) can be decomposed into three linearly independent flow modes: (b) two orthogonal displacement flow modes, and (c) one elongation flow mode. (d) The flow pattern in (a) is reproduced by a flow potential ϕ associated with fluid sources (or sinks) at the four corners of a square (q_1 - q_4). The square symmetry gives rise to (e) two degenerate dipole modes equivalent to two displacement modes in orthogonal directions, and (f) one quadrupole mode equivalent to elongation flow.

do the D4 group elements map to the actual flow functions? Analogous to the subgroups contained in one

symmetry group, these flow manipulation functions are reducible into smaller classes with unique features. We note first that there are only three independent flow modes, resulting from the number of controls (four channels) minus the number of constraints (one associated with the conservation of volume, i.e., $\sum_{i=1}^{4} f_i = 0$). Through inspection, one can readily identify these three modes, forming two classes of flow functions. First, fluxes with opposite signs through a pair of opposing channels give rise to displacement flows along two orthogonal directions (x and y), corresponding to two fundamental modes [Fig. 3.2b]. Second, fluxes with same sign through both pairs of opposing channels provide one more fundamental elongation flow mode [Fig. 3.2c]. Any flow profile produced in this junction [with an example shown in Fig. 3.2a] must be a combination of these three flow modes. However, none of these fundamental modes can be generated by combining any of the rest, a consequence of their linear independence. Importantly, the two displacement modes have a reflection symmetry (along 45° from the x axis), forming a reflection group D1 or a cyclic group C2, which is known to be a subgroup of the D4 group [71]. The single elongation flow mode also represents a trivial subgroup of D4 that contains only the identity operation. In addition to forming different subgroups,
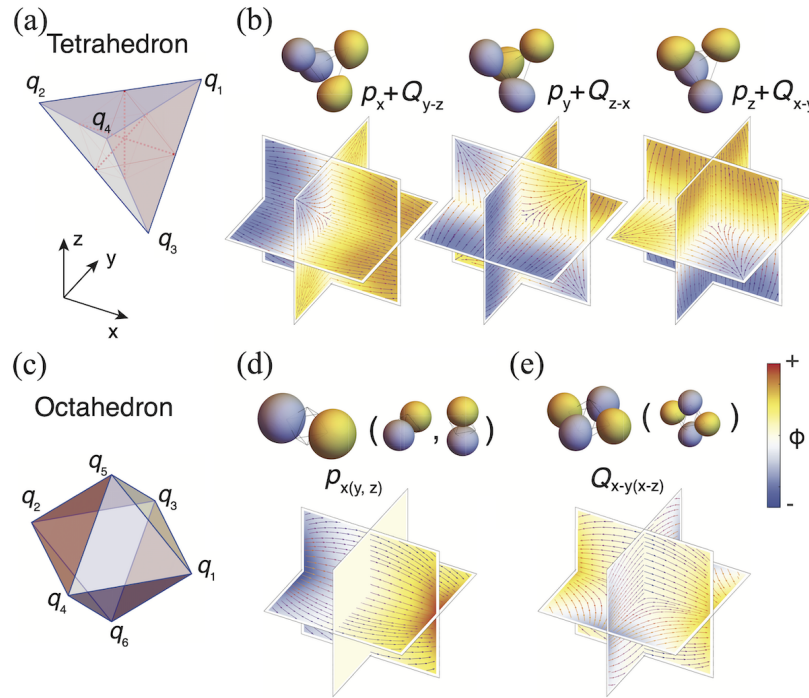
Figure 3.3: Microfluidic devices with 3D symmetries. (a) Fluid sources (or sinks) following a tetrahedral symmetry (q_1 - q_4) can be classified into three degenerate functions, (b) a mix of dipole p and quadrupole Q in each of the three orthogonal directions, representing simultaneous displacement and elongation of the fluid. (c) Fluid sources (or sinks) following an octahedral symmetry (q_1 - q_6) can be classified into two subgroups: (d) three dipoles along orthogonal directions (x, y and z) and (e) two quadrupoles in orthogonal planes (e.g., x-y and x-z), contributing to separate displacement and elongation functions.

these two classes of flows also have distinct characteristic functions, here displacement *vs.* elongation. To abstract these functions from the detailed flow geometries, we map the cross-channel junction to a square, where the flux at each channel is mapped to an effective charge at each lattice site (q_1, q_2, q_3, q_4), representing a point-like fluid source (positive) or sink (negative). The flow field is thus well-defined as a potential flow, with the flow velocity $\mathbf{u}$ given by the gradient of the potential ϕ, i.e., $\mathbf{u} = \nabla\phi$. Since the classes of flow functions are independent of the choice of coordinates, the candidate quantities for such purposes are the strain rate invariants [72] that do not change under any rotation of the microfluidic device. The first-order invariant I_1, which is the trace of the rate of strain tensor $\dot{\gamma}$, is trivial and vanishes for incompressible fluids.

We therefore consider the first non-trivial invariant $I_2 = -\frac{1}{2}\text{Tr}(\dot{\gamma}^2)$. For a 2D potential flow with a total number of $N = 4$ sources and sinks (with magnitudes $\{q_i\}$, located at $\{\mathbf{r}_i\}$), the scalar potential can be expressed as $\phi(\mathbf{r}) = \sum_{i=1}^{4} q_i \ln(|\mathbf{r} - \mathbf{r_i}|)$. Since the rate of strain is linearly related to the magnitudes of sources (or sinks), we can show (Appendix A.3) that the invariant I_2 at the center of the junction has a quadratic form with respect to q_i, i.e., $I_2 = \sum_{i,j=1}^{4} L_{ij} q_i q_j$, where L_{ij} is the element of a coupling tensor, depending on the distance between the pair of q_i and q_j. On a square, there are only two possible types of pairs: pairs along the lateral sides or along the diagonals. With these considerations, we can show (Appendix A.3) that the $\mathbf{L}$ tensor has the form

$$\mathbf{L} = \begin{bmatrix} 0 & a & b & a \\ a & 0 & a & b \\ b & a & 0 & a \\ a & b & a & 0 \end{bmatrix}. \tag{3.1}$$

Elements "a" and "b" are symbolic representations of the above lateral and diagonal couplings, respectively, forming a symmetric circulant matrix for $\mathbf{L}$. A circulant matrix has all the same rows with each row being rotated one element to the right relative to the row above. One mutual eigenvector for any circulant matrix corresponds to the trivial mode where all four charges are identical, i.e., $(q_1, q_2, q_3, q_4) = (1, 1, 1, 1)$. This mode cannot be accessed by a fluid system due to the invalidation of the continuity condition. This leaves $N - 1 = 3$ nontrivial eigenmodes (all satisfying $\sum_{i=1}^{4} q_i = 0$), in agreement with the degrees-of-freedom argument. Every nontrivial mode exhibits a one-to-one map to the fluidic manipulation function as previously classified through subgroups of the D4 group [Fig. 3.2d]. It is worth noting that a hyperbolic point outside the original fluid boundary [indicated by dashed lines in Fig. 3.2d] becomes visible through this symmetry representation of the flow, identifying any potential "trapping" component of a flow pattern. More specifically, the degeneracy of two orthogonal dipoles corresponds to a common displacement function of the flow along orthogonal directions [Fig. 3.2e]. The remaining quadrupole-like mode is nondegenerate and maps to the elongation function [Fig. 3.2f].

3.2.2 3D Microfluidic symmetries

As demonstrated above, the eigenvalue analysis of the stress invariant (I_2) provides an automatic strategy of classifying microfluidic functions, which we now extend to 3D structures to incorporate more sophisticated symmetries. The potential flow now adopts its 3D form with N sources, $\phi(\mathbf{r}) = \sum_{i=1}^{N} -\frac{q_i}{|\mathbf{r}-\mathbf{r}_i|}$. For relatively more practical applications in microfluidics, we consider here the 3D symmetries contained in structures with fewer vertices, namely the tetrahedron ($N = 4$) and the octahedron ($N = 6$).

A tetrahedron has a permutation S4 symmetry [71], corresponding to an unaltered structure (identical through rotation and reflection) by permuting all four vertices [Fig. 3.3a]. The eigenvalue analysis shows that all three eigenmodes for this tetrahedron are degenerate [Fig. 3.3b], due to equivalent neighbors for every vertex. These three modes together represent a threefold rotation symmetry group (C3) (achieved by 120° rotation about any of the face norms), which is a subgroup of S4. Notably, the potential flow of such a mode exhibits a mixture of dipole and quadrupole moments [upper Fig. 3.3b], leading to a microfluidic function corresponding to simultaneously displacing and elongating (transverse to the displacement axis) the fluid within the junction. To obtain a purely displacing flow in 3D, we therefore look to the next available polyhedral symmetry, i.e., the octahedral symmetry.

An octahedron [Fig. 3.3c] can be formed by the middle points of the six edges of a tetrahedron [Fig. 3.3a]. Its symmetry group is isomorphic to S4×C2, with the additional symmetry arising from an extra 2-fold rotation symmetry that is absent for a tetrahedron [Fig. 3.3a] [71]. A similar eigenvalue analysis leads to two groups of degenerate modes, corresponding respectively to dipoles and quadrupoles. The three degenerate dipole modes (p_x, p_y, p_z) are orthogonal in direction, corresponding to a C3 group (through 120° rotation about any of the face norms), one subgroup of the octahedral symmetry group [71]. In such dipole modes, a pair of effective charges along the diagonal (e.g., q_1 and q_2 for p_x) have opposite signs (with the rest of the charges being neutral), corresponding to the activation of a pair of a source and a sink. The two degenerate quadrupoles are distributed in two perpendicular planes (here, x-y and x-z planes), forming a D1 subgroup (switchable by a reflection along the middle plane between x-y and x-z plane). In such quadrupole modes, a
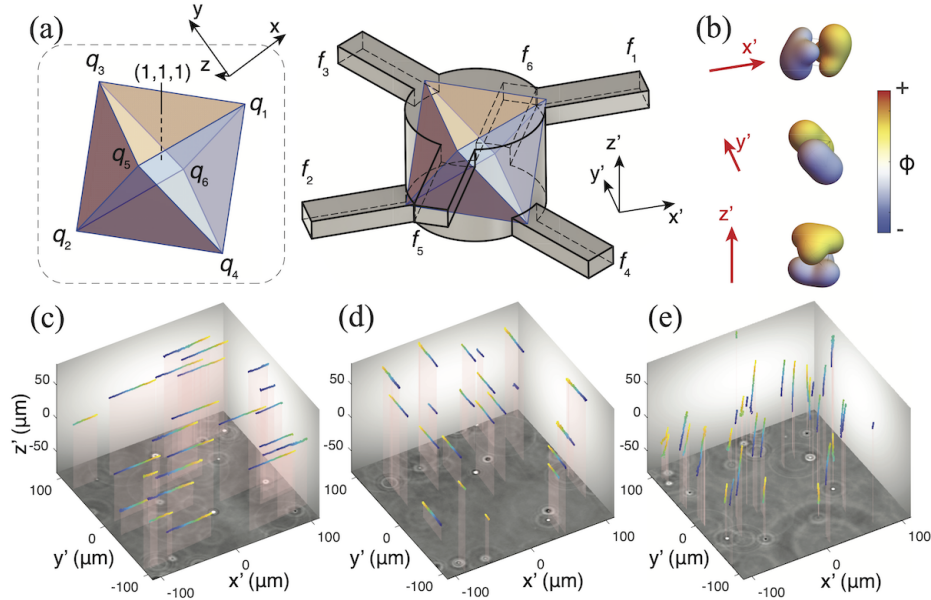
Figure 3.4: Realization of the octahedral symmetry in 3D microfluidics. (a) An octahedron viewed along its original $(1, 1, 1)$ axis (inset) is converted into a microfluidic junction with all sources (or sinks) distributed at two planes perpendicular to the imaging axis z'. (b) The dipole flows in microscope coordinates (x', y', z') are obtained by linear combination of the three orthogonal dipole modes [Fig. 3.3d], with their experimental realizations shown in c, d, and e, respectively. The axial z' positions of the seeding particles are obtained by correlating their phase-contrast images (projected in the bottoms of volumes) with a calibrated library of diffraction patterns.

pair of sources and a pair of sinks along two diagonals are activated. It should be noted that an equivalent quadrupole in the y-z plane can be achieved by superimposing the above two quadrupoles, and is thus not one of the eigenmodes. Analogous to the square symmetry in the 2D case, the octahedral symmetry gives rise to completely separate displacement and elongation flow functions [Fig. 3.3d and e], classified by distinct symmetries. The pure-dipole-like potential in the displacements also ensures that the rate-of-strain invariant I_2 is zero in the middle of the junction. Thus, a superposition of these three displacement flow modes generates 3D omnidirectional flows while preserving the stress-free condition (at least in the middle of the junction).

3.3 Realizing 3D Stress-free microfluidic manipulations

3.3.1 Omnidirectional stress-free flows

To realize such a stress-free microfluidic junction while enabling microscope observation, we rotate the octahedron so that one of its faces (e.g., $(1, 1, 1)$ axis) is aligned along the visualization axis (z'). This rotated geometry fits well into a double-layer microfluidic design [17]: six channels (0.5 mm wide and 0.3 mm deep in cross-sections) at two elevations intersecting a middle cylindrical chamber (with radius $R = 1.0$ mm and height $H = 1.6$ mm) along the radial directions, with the locations of intersections matching that of the octahedral vertices [Fig. 3.4a]. This rotation is also determined by the coordinates of the laboratory frame of reference (x', y', z'), with a radial channel (here, f_1) aligned along the x' axis. We fabricated the microfluidic channel part of this device by fusing multiple sheets of laser-etched glass (Citrogene, see Appendix A.1), which was then mounted on a customized adapter for flow control and microscopy.

To ensure that a displacement flow can be robustly created in all possible directions, we first considered flows along the three orthogonal axes (x', y', z') of the laboratory coordinates forming the basis of the velocity space. The potential representations (isosurfaces) of these orthogonal flows (along x', y', and z') are shown in
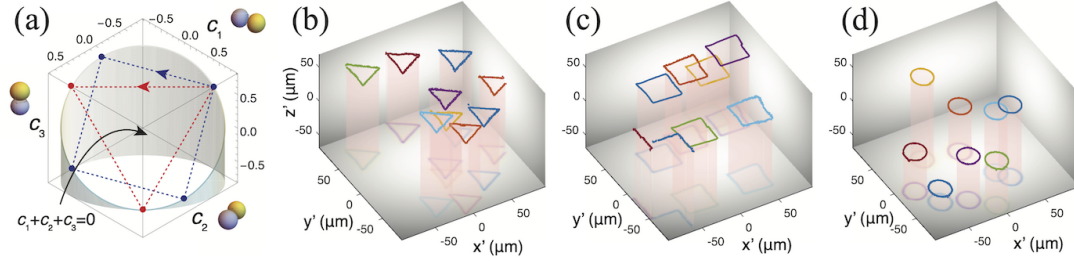
Figure 3.5: Dynamic stress-free displacement flows in 2D. (a) Stress-free displacement flows were controlled in a phase space (c_1, c_2, c_3), as the components of three orthogonal dipole modes. Traces in the $c_1+c_2+c_3 = 0$ plane of this phase space correspond to in-plane flows (in the x'-y' plane) in the real space. The dashed lines correspond to instantaneous transitions between discrete states (dots) of the flow with the arrow showing the transition directions, forming a triangle, a square, and a circle in the continuous limit. The corresponding motions of the flow are shown in (b), (c), and (d), respectively, with individual seeding particles shown in different colors. The periods of these patterns are 3 s, 4 s, and 4 s, respectively.

Fig. 3.4b, which are linear combinations of the above three degenerate dipole modes with their coefficients (c_1, c_2, c_3) being $\frac{1}{\sqrt{6}}(2, -1, -1)$, $\frac{1}{\sqrt{2}}(0, 1, -1)$, and $\frac{1}{\sqrt{3}}(1, 1, 1)$, respectively. In experiments, these effective charges are realized by independently offsetting the fluid pressure on the corresponding channel using two 4-channel piezoelectric regulators (Elveflow OB1 MK3+), with a positive offset for a positive charge (or source) and a negative offset for a negative one (or sink). Custom software was programmed to convert the above flow coefficients into actual pressure settings for flow generation (Appendix A.1). The three orthogonal flows (x', y', z') were successfully generated in our microfluidic device, within the same volume near the center [Fig. 3.4c-e], as demonstrated by the 3D traces of the seeding particles (Appendix A.1). Despite their different geometries in flow dipoles [Fig. 3.4b], these flows are all uniform over almost the entire 3D volume ($\approx 200\ \mu m \times 200\ \mu m \times 150\ \mu m$) captured by the microscope, demonstrating the experimental realization of a robust "stressless" condition that is guaranteed by symmetry.

3.3.2 Dynamic stress-free micromanipulations

To further investigate the experimental capacity of such stress-free microfluidics, we incorporated temporal dependence in the flow by dynamically varying the pressures on all channels (Appendix A.4). To facilitate this time-dependent control, we represented each possible configuration of the displacement flow by its coefficients (c_1, c_2, c_3) when expressed in terms of three degenerate dipole modes, which essentially form a 3D phase space [Fig. 3.5a]. Any time-dependent flow manipulation can thus be generated by a series of points in this phase space. Noting that an axial (z') flow is represented by a vector along the $\frac{1}{\sqrt{3}}(1, 1, 1)$ direction in the phase space, all orthogonal flows must satisfy $c_1 + c_2 + c_3 = 0$, which restricts all horizontal (or in-plane) displacement flows to a plane in the phase space. Hopping in this plane with equal angular separations and distances with respect to the origin $(0, 0, 0)$ gives rise to polygon-shaped flow patterns, for instance, a triangle, a square and a circle in the continuum limit (Fig. 3.5b-d, Movies `MOV_01.mp4`, `MOV_02.mp4`, `MOV_03.mp4`). Such patterns are almost identical for all seeding particles, with the fluid in the bulk translating like a piece of solid.

By incorporating phase spaces out of the $c_1 + c_2 + c_3 = 0$ plane, we also generated time-dependent flows in 3D. For instance, imposing an oscillatory z' motion (with doubled frequency) to the above circular mode gives rise to a 3D flow that represents a Lissajous curve (Fig. 3.6a, Movie `MOV_04.mp4`). Invariably, individual seeding particles within the volume of observation trace out the same pattern as desired. demonstrating the robustness of the stressless condition even under 3D dynamic control.

To assess the flow uniformity, we center the trajectory of every seeding particle within the entire volume and show them side by side. It is clear that these trajectories overlap with each other very well over a full period. In perfectly stress-free flows, all trajectories must be identical, leaving no deviation from the mean
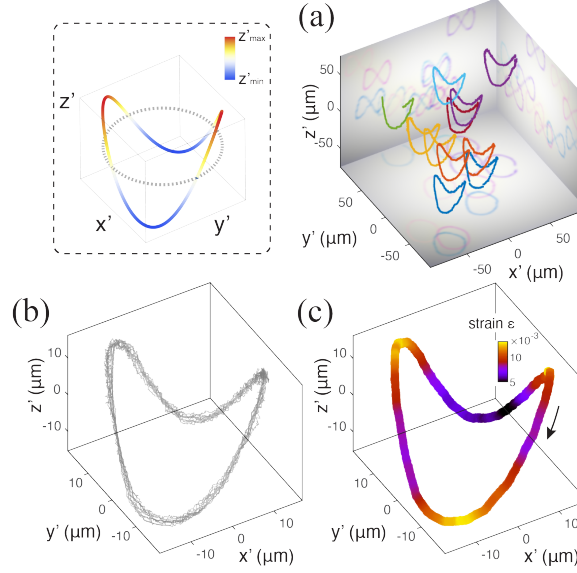
Figure 3.6: 3D stress-free and multiplexed manipulation. (a) A design of the 3D Lissajous pattern (inset, with 3D positions in color and 2D projections in gray) was realized in the flow by incorporating additional axial motion into the circular pattern [Fig. 3.5d], with all seeding particles in the view tracing out the desired 3D pattern (in 8 s). (b) Visualized trajectories (gray curves) of seeding particles (11 particles shown) within the 3D view (200 μm $\times$ 200 μm $\times$ 150 μm in $x' \times y' \times z'$) were overlaid and exhibited a fair degree of uniformity. (c) A characteristic strain ϵ computed along the manipulation path further confirms the uniformity (with ϵ bounded by 2%) of the manipulation flows.

path. We thus defined a characteristic strain based on the deviation from the mean trajectory, i.e., $\epsilon(t) =$ deformation/size $= \Delta \tilde{r}(t)/\Delta r(t)$, where $\Delta r \equiv \sqrt{\langle (\mathbf{r} - \langle \mathbf{r} \rangle) \cdot (\mathbf{r} - \langle \mathbf{r} \rangle) \rangle}$ and $\Delta \tilde{r}(t) \equiv \sqrt{\langle (\tilde{\mathbf{r}} - \langle \tilde{\mathbf{r}} \rangle) \cdot (\tilde{\mathbf{r}} - \langle \tilde{\mathbf{r}} \rangle) \rangle}$ are the fluctuations of displacements of all particles ($\mathbf{r}$) before (Fig. 3.6a) and that ($\tilde{\mathbf{r}}$) after (Fig. 3.6b) centering, with operators $\langle \cdot \rangle$ corresponding to spatial averages. As shown in Fig. 3.6c, such characteristic strains are of the order of $\epsilon \sim 10^{-2}$ for typical 3D manipulations, illustrating the nearly stress-free condition.

The agile flow responses to the controlling pattern in the phase space indicate a direct map of the phase space to the real velocity space. The previously mentioned control in phase space can thus be generalized to arbitrary flow motions to realize more sophisticated manipulation capabilities. To demonstrate this concept, we combine both continuous motions and discrete hops in the phase space (or the velocities) to manipulate, in a stress-free manner, individual particles for "printing" discrete letters (here, "UCM") onto the focal plane. Each letter was traced out by combining motions (along smooth curves) and hops (at the corners of the letter) in the phase space. The discrete gaps between adjacent letters were achieved by abruptly offsetting the fluid in the axial direction so that the previously focused particles were moved away from the focal plane before their reappearance for "printing" the next letter. As shown in Fig. 3.7a, this "printing" task can indeed be achieved in our stress-free microfluidic channel, which further demonstrates its versatile manipulation capabilities (Movie `MOV_05.mp4`).

3.4 Discussion

Our results show a substantial role for symmetry groups in classifying microfluidic functions. These symmetry-group-protected functions are insensitive to detailed geometries, which we exploited to realize 3D stress-free flows in a microfluidic device. Such flows are qualitatively different from all available micromanipulation approaches, where physical traps of certain forms must be present, resulting in stresses on the manipulated objects. Both the stress-free modes and the stressful modes can be characterized by distinct subgroups of a
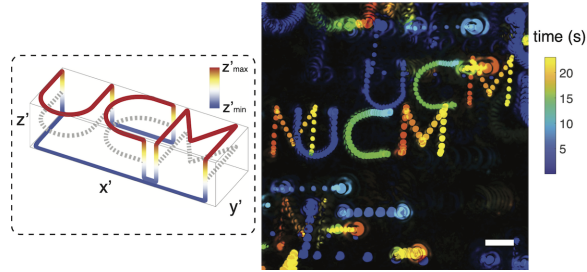
Figure 3.7: More complex 3D flow manipulations were demonstrated by rapidly imprinting the "UCM" (with its design shown in the inset) onto the focal plane by seeding particles, which are color-coded in time (over 23 s). Some of those particles initially out of the focal plane imprint the connecting lines (blue segments in the inset) between letters. The scale bar shows 20 μm.

group of polyhedral symmetry (possessed by the microfluidic device), suggesting independent transport and trapping in microfluidic manipulations.

From our experimental observations, these stress-free flows are demonstrated by extremely parallel trajectories of the manipulated particles, regardless of the detailed curvatures of the trajectories. This enables us to achieve truly multiplexed stress-free manipulations, a significant challenge for trap-based approaches. It is worth noting that our trajectories inevitably deviate from the ideal geometries due to the absence of feedback controls. Meanwhile, any potential differences (e.g., different flow resistances) among the six channels lead to channel-sensitive responses to applied pressures, which ultimately modifies our time-dependent flow patterns. Remarkably, these "defects" in manipulations do not alter the uniformity in the flows (with all particle trajectories remaining parallel), suggesting the robustness in the symmetry-protected flows.

Our work therefore opens up new avenues of experiments on microscopic phenomena that occur in truly stress-free flows. Combinations of the above subgroups easily lead to other subgroups with higher orders (e.g., the C4 subgroup of the D4 group), associated with flow characteristics more than the strain invariants at the center. Flow patterns belonging to these subgroups maybe coordinated in time to form a mutual impact on the manipulated flow, e.g., creating a "mean" vortex that is absent from steady potential flows. These advanced symmetry features and flow manipulation functions will be explored in our future work.

Chapter 4

Digital control of a symmetry-protected microfluidic manipulator

4.1 Introduction

The prevalence of microfluidic devices in research continues to grow as their applications grow and are refined[73]. An especially intriguing field, spurred on by the need not just for preparing an environment to be occupied but to be organized in space, is that of microfluidic manipulation[74]. Many excellent methods have been devised to achieve this goal, such as the Stokes trap[75] for flow-based control, nanogenerators[76, 77] for electrical control, or optical traps[78] for light-based control.

However, the nature of some methods of control require a level of ongoing involvement. For example, in some methods a position (or set of positions) may be specified by the user, leading to the controlling software physically adjusting the mechanisms of manipulation, checking the outcome of the physical adjustment, and restarting the cycle based on the difference in desired and expected outcomes. These closed loop devices based on position control have led to high precision control of microobjects[79]. Different feedback systems, of varying levels of complexity as needed during experiment, have been employed to meet these and similar experimental outcomes[80, 81]. However, by necessity these feedback systems require time to be invested during each control cycle to receive, analyze, and instruct based on available collected data.

Here, we discuss the technical implementation of digital control of a 6 channel symmetry-protected microfluidic manipulator[17]. (See Appendix B for a discussion of work done with a 4 channel device) By exploiting the large working zone available in this device, along with the separated directional and stressful modes, we achieve successful supervisor-free control of microobjects. The velocity based control used in the device allows for prescription of paths of arbitrary complexity in position and velocity without requiring a feedback loop. We first discuss the architecture of the controlling program to achieve full control of the hardware stack used with the device. Then we present a derivation of the pressure activation strategy using an abstraction of the device details to just fluid sources and sinks. Finally, we review path traversal choices included as features in the current pressure pump control program to achieve different physical outcomes. Overall, the software and hardware suite allows for supervisor-free microfluidic manipulation that allows for experimental implementation of different physical flow properties.

4.2 Pressure pump controller program

We make use of custom Python 3 code to control our experimental setup, with a GUI (Fig. 4.1), written using the tkinter Python package for developing with the Tcl/Tk GUI toolkit[82], acting as a front end to control two major backends, camera control and pressure pump control, as well as frame display, extraneous data management, and control of a Prior ProScan III stage.
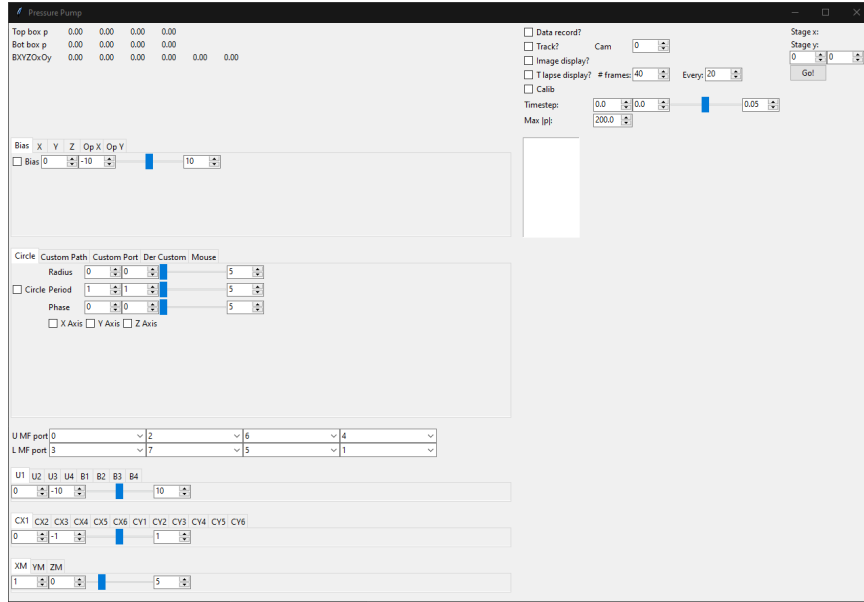
Figure 4.1: Pressure pump controller graphical user interface. Top left: Pressure pump readouts of port pressures and applied mode amounts. Top right: Various controls including image viewing and stage control. Middle: Individual mode controls and custom path generation inputs. Bottom: Various controls including port selection and manual port pressure settings.

4.2.1 Camera control

We make use of FLIR Grasshopper3 (GS3-U3-41C6M-C) and Andor Zyla (ZYLA-4.2P-USB3) cameras for imaging the interior of the microfluidic device. One or more FLIR Grasshopper3 cameras are connected by USB3 to the computer, and when used in plural are synchronized via the Python program for simultaneous frame capture. Frames are stored to a memory buffer which can be accessed by the frame display backends. For image storage, every frame is sent to a PyTorch Python package[83] queue backed by shared memory which can then be saved to a file on an SSD drive.

4.2.2 Pressure pump control

A variety of pressure pump controls are exposed to the user via the GUI, including raw access to pressures on each of the ports as an additive baseline, manipulation of the resistive matrix elements that perform the mapping from physical velocities to applied pressures, application of the pressure configurations that correspond to the modes of the 6-channel microfluidic device, custom time-dependent application of the directional x-,y-, and z-modes, custom time-dependent application of raw port values, and custom time-dependent planar motion.

All custom time-dependent modules take raw text in sympy Python package[84] function syntax that is then parsed for use according to its structure. A supplementary Python 3 program was written to take a basic language of path components, including time and 3D spatial instructions, that is human-friendly to write and translate it into the precise array sympy syntax needed for operation. When the sympy form is a path function, then its derivative is taken analytically and the velocity components are passed to conversion to the necessary pressures. When the sympy form is for raw port control, the form as a vector representing the 6 ports is parsed and the calculations directly applied as pressures on the ports. When the sympy form is for planar motion, such as a complex-valued function for conformal mapping, the real and imaginary values are taken and sent to the pressure pump.

The numpy Python package[85] is used both for direct computation stemming from all basic user input as well as a module for sympy to accelerate custom expressions from the user, and the numba Python package[86] is used for further acceleration of simpler portions of the pressure computation. These values are then sent to

the two Elveflow pressure pumps (Elveflow OB1 Mk3+) via USB3 as input. The pressure values are also read via USB3 off of the pressure pumps and displayed in the GUI. Both values sent to the pressure pumps as well as values read from the pressure pumps can be saved as a file. The amounts of each of the modes being sent to the pump from all user-input are displayed in the GUI in real time.

Testing the Elveflow pressure boxes under a wide variety of conditions, slow and rapid variation of pressures, has revealed a correspondingly varying adherence (Fig. 4.2, top) to the prescribed pressures (Fig. 4.2, middle) after including a noise term to overcome an issue when the boxes receive identical input pressure values over a period of time. An appreciable difference in set and read pressures is present but empirically of minor impact, with the major contribution to path deviation coming from the response-and-settling-time under rapid switching. We have found that while the expected mode dominates in what is applied to the microfluidic device (Fig. 4.2, bottom), that dominant mode does not necessarily stay applied with the desired time dependence, and can be accompanied by the other modes available for use on the microfluidic device.

4.2.3 Frame display

Two backends for frame display run for each attached camera. One backend displays the raw frame obtained by the camera from the relevant shared memory buffer. The second backend displays a composite image for aiding the visualization of the captured frames over time, such as when viewing a traced polygon. A user-controlled number of previous images are stored in a stack in memory on an Nvidia GPU using the cupy Python package[87] interface to CUDA. At each iteration of user-specified duration, the stack of images has the maximum intensity value found through all frames and the final image of those maximum values is displayed to the user. The OpenCV 2 Python package[88] is used to display all images at high frame rate.

4.3 Source and sink activation strategy derivation

We can approximate the flow configuration with a series of n point sources and sinks arranged with a geometry similar to the microfluidic device. In doing so we can determine the mandatory activation strategy for the ports on the actual experimental device with 6 channels to achieve a given velocity and strain rate outcome. (See Appendix B for an accompanying derivation of activation strategies for the 4 channel case in line with the work presented here)

The flow within the region in experiment bounded by the glass chamber with its center as the origin is approximated in the unbounded case by[18]

$$\mathbf{u}(\mathbf{r}) = \sum_{i=1}^{n} \frac{m_i}{4\pi} \frac{\mathbf{r} - \mathbf{r}'_i}{|\mathbf{r} - \mathbf{r}'_i|^3}, \tag{4.1}$$

where m_i are the strengths, including sign, of the point sources and sinks located at positions $\mathbf{r}'_i$. Volume preservation is maintained by the condition $\sum_{i=1}^{n} m_i = 0$. The rate of strain tensor is then

$$\dot{\gamma}(\mathbf{r}) = \frac{1}{2} \left(\nabla \mathbf{u} + (\nabla \mathbf{u})^\top \right) = \sum_{i=1}^{n} \frac{m_i}{4\pi} \left(\frac{\mathbf{I}}{|\mathbf{r} - \mathbf{r}'_i|^3} - 3 \frac{\left(\mathbf{r} - \mathbf{r}'_i\right)\left(\mathbf{r} - \mathbf{r}'_i\right)}{|\mathbf{r} - \mathbf{r}'_i|^5} \right), \tag{4.2}$$

where $\mathbf{I}$ is the identity matrix.

At the center of the chamber for point sources and sinks placed equidistant from the origin, Eq.s 4.1 and 4.2 reduce to

$$\mathbf{u}(\mathbf{0}) = \sum_{i=1}^{n} -\frac{m_i}{4\pi} \frac{\mathbf{r}'_i}{|\mathbf{r}'_i|^3}, \tag{4.3}$$

$$\dot{\gamma}(\mathbf{0}) = \sum_{i=1}^{n} -\frac{3m_i}{4\pi} \frac{\mathbf{r}'_i \mathbf{r}'_i}{|\mathbf{r}'_i|^5}. \tag{4.4}$$
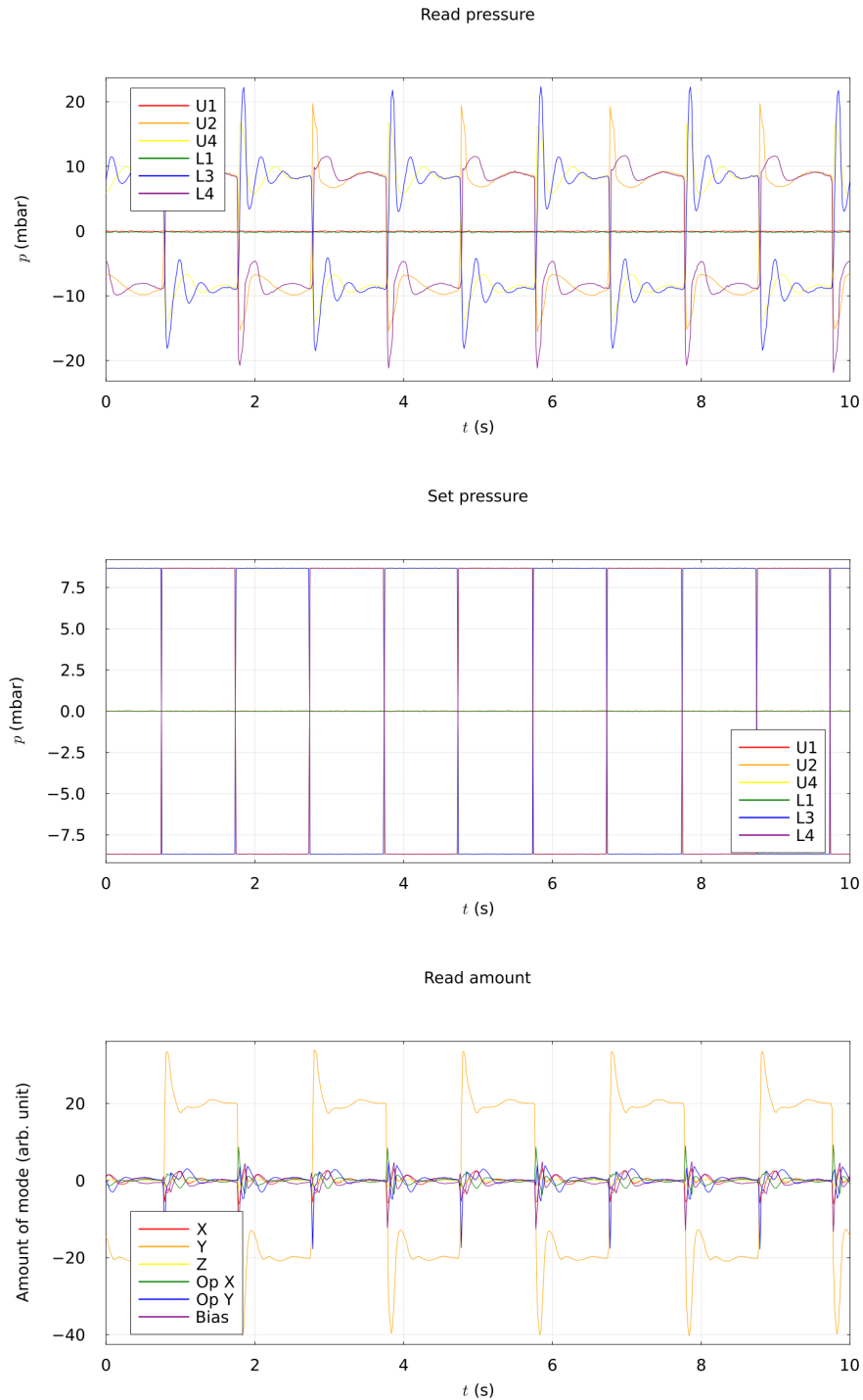
Figure 4.2: Analysis of pressures on the Elveflow boxes for an up/down ($+y/-y$) recurring pattern. Top (middle): Pressure read from (sent to) the Elveflow pressure boxes. Each line represents the pressure on a given port on the box. Bottom: Mode decomposition of received pressures in terms of the modes available to the 6 channel Stokes Wind Tunnel. All plots occur over the same 10 s period.

4.3.1 6 channel case

A symmetric simplification can be made by assuming every point source or sink of strength m_j at position $\mathbf{r}'_j$ has a point source or sink at a position mirrored across the center of the chamber. Then, the field and rate of strain at the center for any such pair of sources and sinks m_a and m_b, without assuming sign, can be written as

$$\mathbf{u}_{ab}(\mathbf{0}) = -\frac{(m_a - m_b)}{4\pi} \frac{\mathbf{r}'_a}{|\mathbf{r}'_a|^3} \tag{4.5}$$

$$= -\frac{1}{4\pi} \frac{\mathbf{r}'_a}{|\mathbf{r}'_a|^3} (1, -1) \cdot (m_a, m_b) \tag{4.6}$$

$$\dot{\gamma}_{ab}(\mathbf{0}) = -\frac{3}{4\pi} \frac{\mathbf{r}'_a \mathbf{r}'_a}{|\mathbf{r}'_a|^5} (1, 1) \cdot (m_a, m_b), \tag{4.7}$$

linear in the strengths. Since the phase space of choices of strength can be rewritten from two individual activation choices to a superposition of pair activations with the same strengths, including sign, and pair activations with opposite strengths, i.e.

$$(m_a, m_b) = m_a(1, 0) + m_b(0, 1) = m'_a(1, 1) + m'_b(1, -1), \tag{4.8}$$

we may consider separately the cases with the point sources and sinks conjoined as described.

For any equidistant configuration, substitution of Eq. 4.8 into Eq.s 4.6 and 4.7 shows reductions for the two choices of pair activation. In the case where every point source of strength m_j at $\mathbf{r}'_j$ has a mirrored point sink, the direction of velocity at the center is determined by

$$\mathbf{u}_{\text{opp pairs}}(\mathbf{0}) \propto \sum_{j \in \text{pairs}} -m_j \mathbf{r}'_j, \tag{4.9}$$

while the rate of strain vanishes at the center,

$$\dot{\gamma}_{\text{opp pairs}}(\mathbf{0}) = \mathbf{0}. \tag{4.10}$$

The trivial choice for achieving 3D flow control would necessitate a regular octahedron of exactly 6 point sources and sinks, arranged such that each pair aligns with the 3 Cartesian directions, i.e.

$$\mathbf{r}'_i \propto \pm \hat{x}, \pm \hat{y}, \pm \hat{z}. \tag{4.11}$$

Assigning a nonzero strength to any single pair would lead to a strainless flow along the axis of the pair at the center of the chamber. Then, to match our experimentally compatible device, that regular octahedron would be deformed such that no point would impede a view into the chamber along the vertical axis. This new octahedron would still maintain opposing points in pairs, with

$$\mathbf{r}'_i = a \left(\cos\left(60° (i - 1)\right) \hat{x} + \sin\left(60° (i - 1)\right) \hat{y} \right) \pm b\hat{z} \tag{4.12}$$

with upper sign for i odd and lower for even, where a and b are some positive lengths. Choosing $\mathbf{r}'_2, \mathbf{r}'_4,$ and $\mathbf{r}'_6$ to be representative of the pairs W.L.O.G., condition Eq. 4.9 for some flow direction $u_d \hat{x} + v_d \hat{y} + w_d \hat{z}$ yields the flow strengths

$$(m_2, m_4, m_6) \propto u_d \left(\frac{1}{3a}\right)(-1, 2, -1) + v_d \left(\frac{\sqrt{3}}{3a}\right)(-1, 0, 1) + w_d \left(\frac{1}{3b}\right)(-1, -1, -1) \tag{4.13}$$

and hence the full set of strengths can be written as

$$(m_1, m_2, m_3, m_4, m_5, m_6) \propto u'_d(-2, -1, 1, 2, 1, -1) + v'_d(0, -1, -1, 0, 1, 1) + w'_d(1, -1, 1, -1, 1, -1) \tag{4.14}$$

where the constants u'_d are proportional to the original u_d and share the same sign. The relative strengths of this set, including sign, correspond to the port conditions for the x-, y-, and z-flow modes presented in our previous work[17].

We now consider the second case for any equidistant configuration, where substitution of Eq. 4.8 into Eq.s 4.6 and 4.7 shows reductions for the next choice of pair activation. In the case where every point source of strength m_j at $\mathbf{r}'_j$ has a mirrored point source, the velocity vanishes at the center,

$$\mathbf{u}_{\text{same pairs}}(\mathbf{0}) = \mathbf{0}, \tag{4.15}$$

while the rate of strain at the center is determined by

$$\dot{\gamma}_{\text{same pairs}}(\mathbf{0}) \propto \sum_{j \in \text{pairs}} -m_j \mathbf{r}'_j \mathbf{r}'_j. \tag{4.16}$$

Choosing $\mathbf{r}'_2, \mathbf{r}'_4$, and $\mathbf{r}'_6$ to be representative of the pairs W.L.O.G., condition Eq. 4.16 for some strain rate tensor

$$\dot{\gamma}_{xxd}\hat{x}\hat{x} + \dot{\gamma}_{xyd}\hat{x}\hat{y} + \dot{\gamma}_{xzd}\hat{x}\hat{z} + \dot{\gamma}_{yxd}\hat{y}\hat{x} + \dot{\gamma}_{yyd}\hat{y}\hat{y} + \dot{\gamma}_{yzd}\hat{x}\hat{z} + \dot{\gamma}_{zxd}\hat{z}\hat{x} + \dot{\gamma}_{zyd}\hat{z}\hat{y} + \dot{\gamma}_{zzd}\hat{z}\hat{z} \tag{4.17}$$

yields the flow strength relations

$$-a^2\left(\frac{m_2}{4} + m_4 + \frac{m_6}{4}\right) = \dot{\gamma}_{xxd} \tag{4.18}$$

$$-\frac{\sqrt{3}a^2}{4}(m_2 - m_6) = \dot{\gamma}_{xyd} \tag{4.19}$$

$$-ab\left(\frac{m_2}{2} - m_4 + \frac{m_6}{2}\right) = \dot{\gamma}_{xzd} \tag{4.20}$$

$$-\frac{3a^2}{4}(m_2 + m_6) = \dot{\gamma}_{yyd} \tag{4.21}$$

$$-b^2(m_2 + m_4 + m_6) = \dot{\gamma}_{zzd} \tag{4.22}$$

$$-\frac{\sqrt{3}ab}{2}(m_2 - m_6) = \dot{\gamma}_{yzd}, \tag{4.23}$$

where use is made of the symmetric property of the tensor to omit repetitive quantities. Combining Eq.s 4.19 and 4.23 because of their similarity and then rearranging we have

$$m_2 - m_6 = -\dot{\gamma}'_{xyd} - \dot{\gamma}'_{yzd} = \dot{\gamma}'_A, \tag{4.24}$$

where we use primes to denote quantities proportional to their unprimed counterparts, including the same sign, and then denote the final expression as a single A quantity. We further rearrange Eq. 4.20 to have

$$\frac{m_2}{2} - m_4 + \frac{m_6}{2} = -\dot{\gamma}'_{xzd} = \dot{\gamma}'_B, \tag{4.25}$$

following the same labeling convention as before. Finally, we combine Eq.s 4.18, 4.21, and 4.22, and utilizing the traceless property of the strain rate tensor we have

$$m_2 + m_4 + m_6 = 0, \tag{4.26}$$

prompting us to note as an aside the trivial result of Eq. 4.22 vanishing on the left side, preventing any activation strategy from resulting in $\dot{\gamma}_{zzd}$ at the center.

Summarizing the reductions, we have

$$m_2 - m_6 = \dot{\gamma}'_A \tag{4.27}$$

$$\frac{m_2}{2} - m_4 + \frac{m_6}{2} = \dot{\gamma}'_B \tag{4.28}$$

$$m_2 + m_4 + m_6 = 0, \tag{4.29}$$

giving the solution

$$(m_2, m_4, m_6) = \frac{\dot{\gamma}'_A}{2} (1, 0, -1) + \frac{\dot{\gamma}'_B}{3} (1, -2, 1). \tag{4.30}$$

From this we see already mutually exclusive strain rate components, and referring back to Eq.s 4.18-4.23 we further see the two source activation choices lead to additional strain rate tensor components: Substituting in the A source activation choice (i.e. $(m_2, m_4, m_6) \propto (1, 0, -1)$) has the immediate monopoly on $\dot{\gamma}_{xyd}$ and $\dot{\gamma}_{yzd}$ (c.f. Eq. 4.24), but substituting in the B source activation choice (i.e. $(m_2, m_4, m_6) \propto (1, -2, 1)$) has the immediate monopoly on $\dot{\gamma}_{xzd}$ (c.f. Eq. 4.25) as well as $\dot{\gamma}_{xxd}$ (c.f. Eq. 4.18) and $\dot{\gamma}_{yyd}$ (c.f. Eq. 4.21). Visualizing these respective strain rate tensor components in matrix form, we have for the A and B activation choices respectively

$$[m]_A \rightarrow \begin{pmatrix} 0 & X & 0 \\ X & 0 & X \\ 0 & X & 0 \end{pmatrix}, [m]_B \rightarrow \begin{pmatrix} X & 0 & X \\ 0 & X & 0 \\ X & 0 & 0 \end{pmatrix}, \tag{4.31}$$

where X's represent components allowed to be finite when not made null by symmetry protection. These results are in agreement with our symmetry analysis presented in Chapter 2 and Appendix C.

4.4 Time dependent path formulation

Having presented an activation strategy for strainless 3D manipulation, we now consider the movement of microobjects in space. As our device is based on velocity control, it is concerned with the necessary velocities which can be obtained from the time-dependent path formulation.

We begin with a straightforward formulation of paths that is linear in time, requiring 2 constraints to match the start position and end position. A line segment between start and end locations $\mathbf{r}_i, \mathbf{r}_f$, respectively, with start and end times t_i, t_f, respectively, has the representation

$$\mathbf{r}(t) = \frac{t_f - t}{t_f - t_i} \mathbf{r}_i + \frac{t - t_i}{t_f - t_i} \mathbf{r}_f, \tag{4.32}$$

with the velocity trivially given by

$$\mathbf{v}(t) = \frac{\mathbf{r}_f - \mathbf{r}_i}{t_f - t_i}. \tag{4.33}$$

As an example of a planar square, the set of points $(1, 0), (1, 1), (0, 1), (0, 0)$ traversed in a counterclockwise, closed fashion with one unit of time per line segment has the representation

$$\mathbf{r}(t) = \begin{cases} (1 - t)(1, 0) + (t - 0)(1, 1) & 0 \le t < 1 \\ (2 - t)(1, 1) + (t - 1)(0, 1) & 1 \le t < 2 \\ (3 - t)(0, 1) + (t - 2)(0, 0) & 2 \le t < 3 \\ (4 - t)(0, 0) + (t - 3)(1, 0) & 3 \le t < 4 \end{cases}, \tag{4.34}$$

and the corresponding velocity given by

$$\mathbf{v}(t) = \begin{cases} (0, 1) & 0 \le t < 1 \\ (-1, 0) & 1 \le t < 2 \\ (0, -1) & 2 \le t < 3 \\ (1, 0) & 3 \le t < 4 \end{cases}. \tag{4.35}$$

Higher order time dependence can be used, with increasing control over physical aspects for the trajectory. To eliminate the discontinuity in the velocities at the vertices of two intersecting line segments, which would

avoid a large transition of pressure from one time step to the next, the formulation between the times t_i, t_f may be given by

$$\mathbf{r}(t) = P_{3,i}(t)\mathbf{r}_i + P_{3,f}(t)\mathbf{r}_f, \tag{4.36}$$

where the quantities P_3 are cubic order polynomial functions of t chosen to impose the boundary condition $\mathbf{v}(t_i) = \mathbf{v}(t_f) = \mathbf{0}$ (two more constraints on top of the original two for position). It can be shown by linear algebra that the end expression takes the form

$$\mathbf{r}(t) = P_{3,\text{fall}}\left(t_{\text{rise}}(t)\right)\mathbf{r}_i + P_{3,\text{rise}}\left(t_{\text{rise}}(t)\right)\mathbf{r}_f, \tag{4.37}$$

where $P_{3,\text{fall}}(t) = 2t^3 - 3t^2 + 1$ and $P_{3,\text{rise}}(t) = -2t^3 + 3t^2$ are the relevant cubic polynomials and $t_{\text{rise}}(t) = \frac{t-t_i}{t_f-t_i}$. The piecewise function for position previously given in the linear case (Eq. 4.34) can easily have its time dependence modified to make use of this imposition of null velocity at the vertices, and the velocity will be quadratic in form but continuous at the vertices.

A higher order time dependence can still further be derived, next eliminating the discontinuity in the derivatives of the velocity, and thus further smoothing out the transitions being made by the pressure pumps. Logically, to add two more constraints, quintic order polynomials would be required,

$$\mathbf{r}(t) = P_{5,i}(t)\mathbf{r}_i + P_{5,f}(t)\mathbf{r}_f, \tag{4.38}$$

where the quantities P_5 are quintic order polynomial functions of t chosen to impose the boundary condition $\mathbf{v}(t_i) = \mathbf{v}(t_f) = \mathbf{0}, \mathbf{v}'(t_i) = \mathbf{v}'(t_f) = \mathbf{0}$. It can be shown by linear algebra that the end expression takes the form

$$\mathbf{r}(t) = P_{5,\text{fall}}\left(t_{\text{rise}}(t)\right)\mathbf{r}_i + P_{5,\text{rise}}\left(t_{\text{rise}}(t)\right)\mathbf{r}_f, \tag{4.39}$$

where $P_{3,\text{fall}}(t) = -6t^5 + 15t^4 - 10t^3 + 1$ and $P_{5,\text{rise}}(t) = 6t^5 - 15t^4 + 10t^3$ are the relevant quintic polynomials. The piecewise function for position previously given in the linear case (Eq. 4.34) can easily have its time dependence modified to make use of this imposition of null velocity at the vertices and null derivatives of the velocity, and the velocity will be quartic in form but continuous and differentiable at the vertices.

4.4.1 Constant angular velocity along line segment of path

We next consider paths with a smooth variation of velocity. Choosing, W.L.O.G., a line segment between planar points $(x_1, y_1, 0), (x_2, y_2, 0)$, we write down the position vector in the plane $\mathbf{r} = (x, y, 0)$. Combining the usual expressions for polar coordinates with the standard equations for lines,

$$x = r\cos\theta \tag{4.40}$$
$$y = r\sin\theta \tag{4.41}$$
$$y - y_1 = m(x - x_1) \tag{4.42}$$
$$m = \frac{y_2 - y_1}{x_2 - x_1}, \tag{4.43}$$

we express the radial coordinate r as

$$r = \frac{y_1(x_2 - x_1) - x_1(y_2 - y_1)}{\sin\theta(x_2 - x_1) - \cos\theta(y_2 - y_1)}. \tag{4.44}$$

Thus the final expression of the path in Cartesian vector components but in polar coordinates can be given as $\mathbf{r}(\theta) = (r\cos\theta, r\sin\theta, 0)$ with r given by Eq. 4.44.

By expressing this in terms of θ, the angular sweep of, as an example, a regular polygon centered on the origin can be directly controlled to enforce constant angular velocity ω while moving along the path, i.e. $\theta = \omega t$. The resulting shape of passive tracer particles can then be imaged (Fig.s 4.3-4.5).

Figure 4.3: Time lapse image of 2 µm latex tracer particles moved inside microfluidic manipulator tracing out a square with constant angular velocity. Window size is 188 µm × 188 µm.

Figure 4.4: Time lapse image of 2 µm latex tracer particles moved inside microfluidic manipulator tracing out a hexagon with constant angular velocity. Window size is 188 µm × 188 µm.
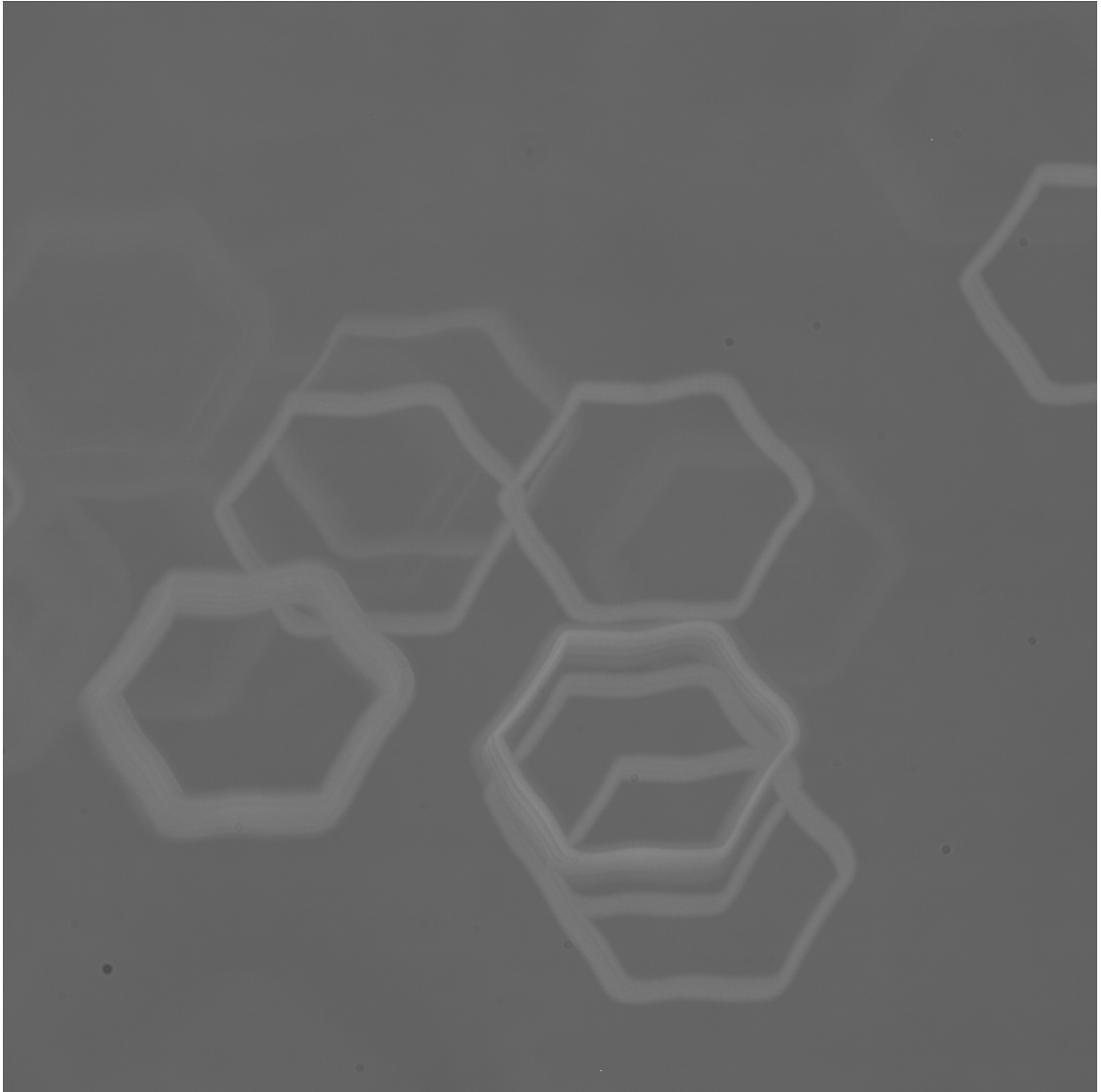
Figure 4.5: Time lapse image of 2 µm latex tracer particles moved inside microfluidic manipulator tracing out a octagon with constant angular velocity. Window size is 188 µm × 188 µm.

4.5 Conformal mapping path formulation

We next consider another way to map the smooth navigation of pressures in a circular fashion to an arbitrary collection of line segments creating a closed path, via conformal mapping. In our case, as an example we choose to map between the unit circle, expressed in complex space by $z \propto \exp(2\pi t i/T), 0 \leq t \leq T$ for some period T, and a closed polygon in complex space $f(z)$ with the set of n vertices z_k, with k an integer denoting a given vertex. The polygonal path has as its derivative[89]

$$f'(z) \propto \prod_k \left(1 - \frac{z}{z_k}\right)^{a_k - 1}, \tag{4.45}$$

where $a_k \pi$ is the set of interior angles of the polygon. As a geometric consequence, $\sum_k (a_k - 1) = -2$, and we have the specific equivalence $a_k - 1 = -2/n$ in our regular polygon example. Considering the time dependence of this mapping, we have the time derivative

$$\dot{f}(z) = f'(z)\dot{z} \propto \exp\left(\frac{2\pi t i}{T}\right) \prod_k \left(1 - \frac{\exp\left(\frac{2\pi t i}{T}\right)}{z_k}\right)^{-2/n}. \tag{4.46}$$

From inspection, the derivative can achieve the greatest magnitude when rounding the corners of the polygon. Choosing the vertices z_k for a square centered on the origin as an explicit example, up to a constant of proportionality and a phase, we may substitute $z_k \propto \exp(2\pi k i/4), 0 \leq k \leq 3$ to arrive at the final expression. By taking the real and imaginary components of Eq. 4.46, we have the planar components of velocity to then provide to the pressure pumps. The resulting shape of passive tracer particles can then be imaged to show the experimentally integrated result of the velocity components (Fig.s 4.6-4.10). As expected, the tracer particles move most rapidly when rounding the corners of the polygon as revealed by motion between frames of camera capture. Some waviness is visible in the tracing particles when directing along the side of the shape.

4.6 Discussion

We have presented a digital control suite for achieving supervisor-free microfluidic control over microobjects. It is able to accommodate the many physically distinguished situations by using symmetry-protected flow modes within the microfluidic manipulator. We show a general means of deriving those velocity and strain rate capacities using simple point sources and sinks that can then be used by the program. A number of path generation techniques have been developed to achieve velocity-based control for arbitrarily complex paths with the computer program, each with different ways to traverse the points in space.

More work is open for improving the quality of this supervision-free control. For example, due to imperfections in the pressure application and geometry of microfluidic chip design, small errors are present that disrupt the theoretically strainless flow while remaining practically so for certain experimental requirements. The waving visible in, for example, paths such as the square traversed with conformal mapping (Fig. 4.7) likewise indicates errors due to some mechanical oscillation, perhaps in the path from the pressure pumps through the air in the plastic tubing down to the fluid reservoirs on the device. Such errors could be approached in a number of ways. By analyzing the robustness of any waving a cancellation pressure curve could be calculated and added to the pressure settings of the pump. Additionally, offsets from the prescribed path could be determined in real time as shown with the optical supervision feedback loop in Chapter 3, albeit at the cost of slower run times.

Additionally, by improving the pressure application and geometry of design, the extent of precision in space and time can be increased and better adherence to the generated paths can be obtained. For the former improvement, alternative pressure sources with different trade-offs between absolute pressure range and pressure resolution are one place for future investigation. For the latter improvement, alternative means of fabricating the microfluidic device, such as channels made with standard polydimethylsiloxane (PDMS) molding techniques[90] or by laser engraving of glass[91], could enable tighter tolerances in desired channel geometry and thus have better symmetry.
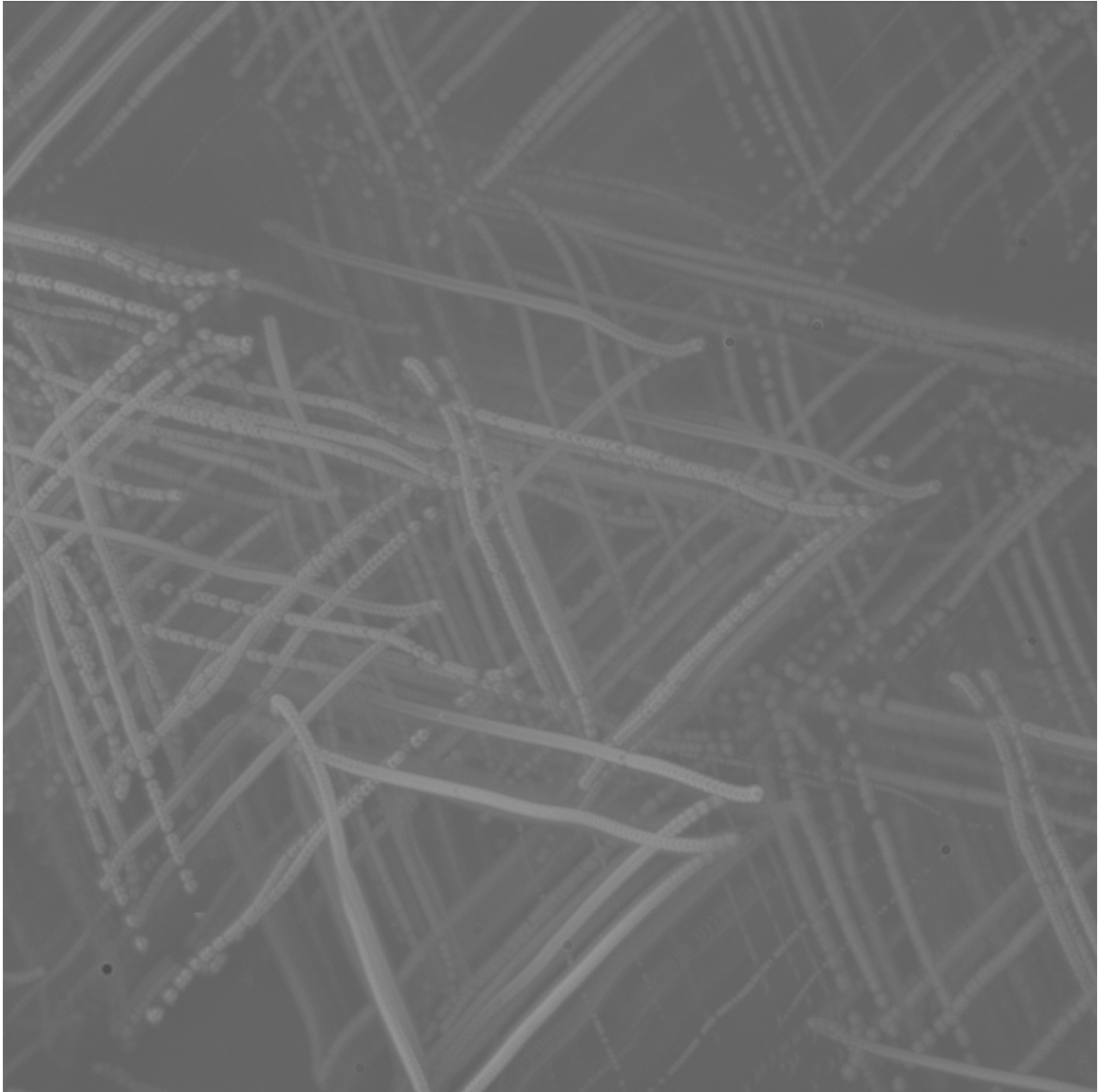
Figure 4.6: Time lapse image of 2 µm latex tracer particles moved inside microfluidic manipulator tracing out an experimentally integrated triangle via conformal mapping. Window size is 188 µm × 188 µm.
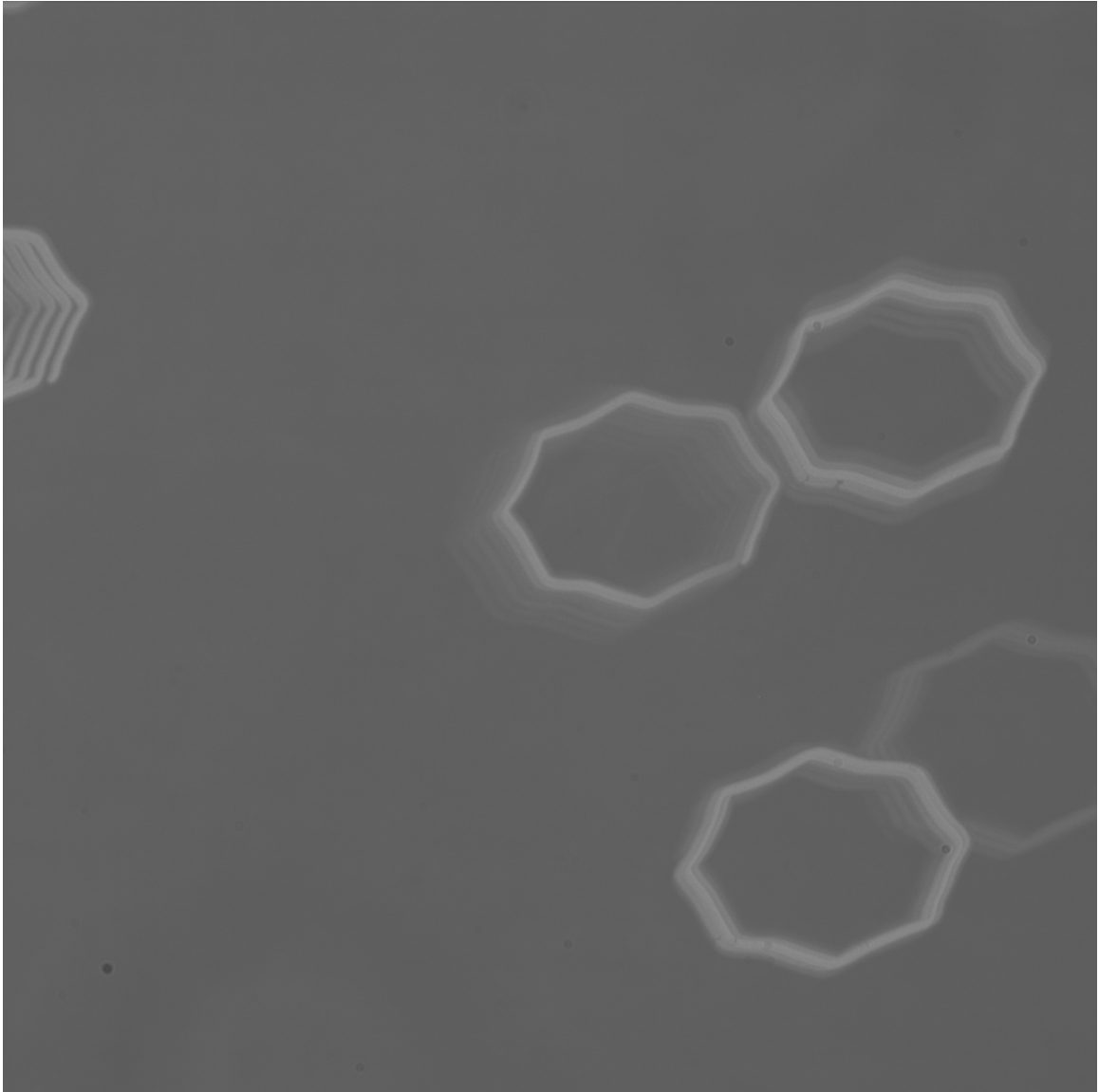
Figure 4.7: Time lapse image of 2 µm latex tracer particles moved inside microfluidic manipulator tracing out an experimentally integrated square via conformal mapping. Window size is 188 µm × 188 µm.
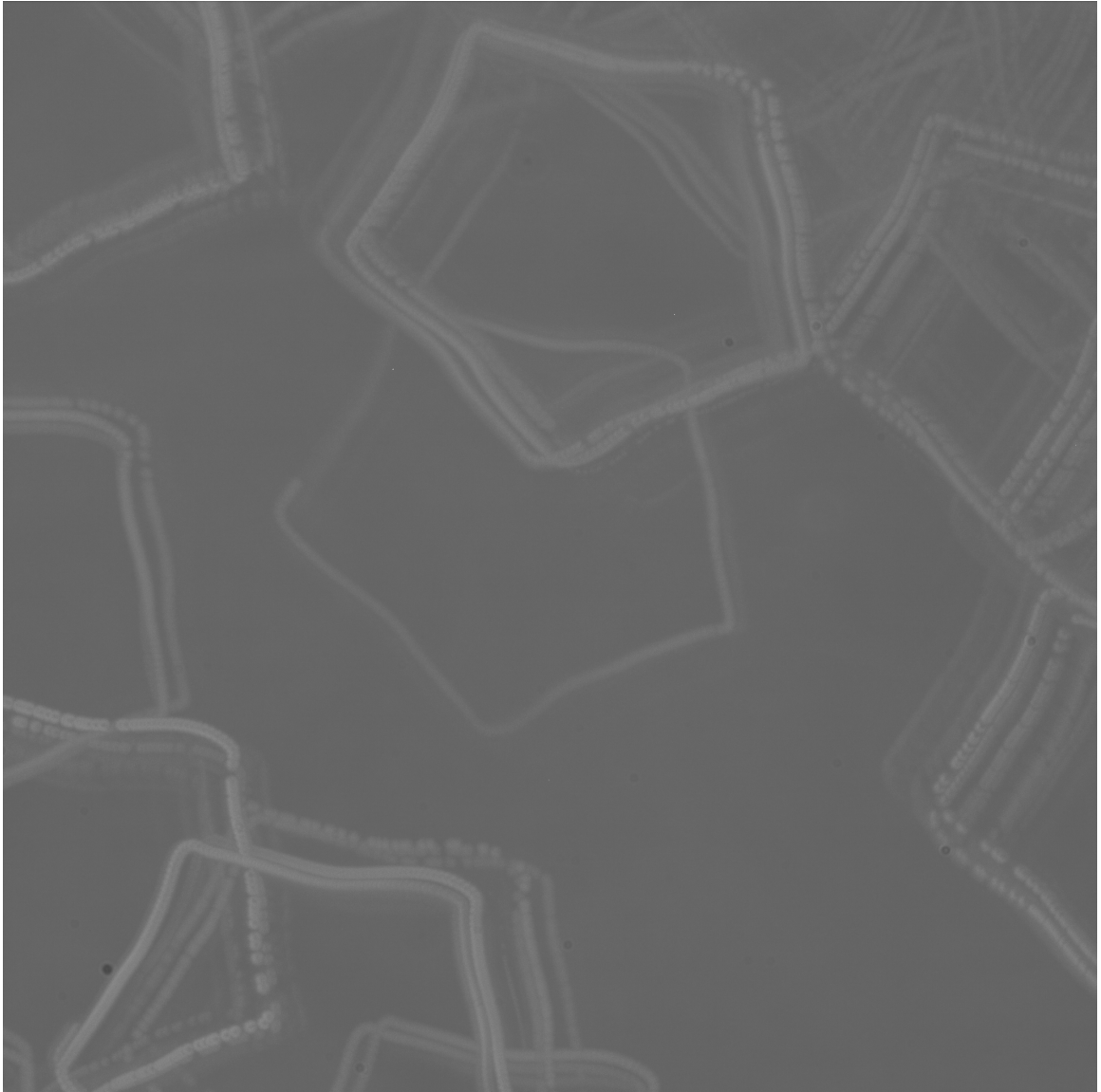
Figure 4.8: Time lapse image of 2 µm latex tracer particles moved inside microfluidic manipulator tracing out an experimentally integrated pentagon via conformal mapping. Window size is 188 µm × 188 µm.
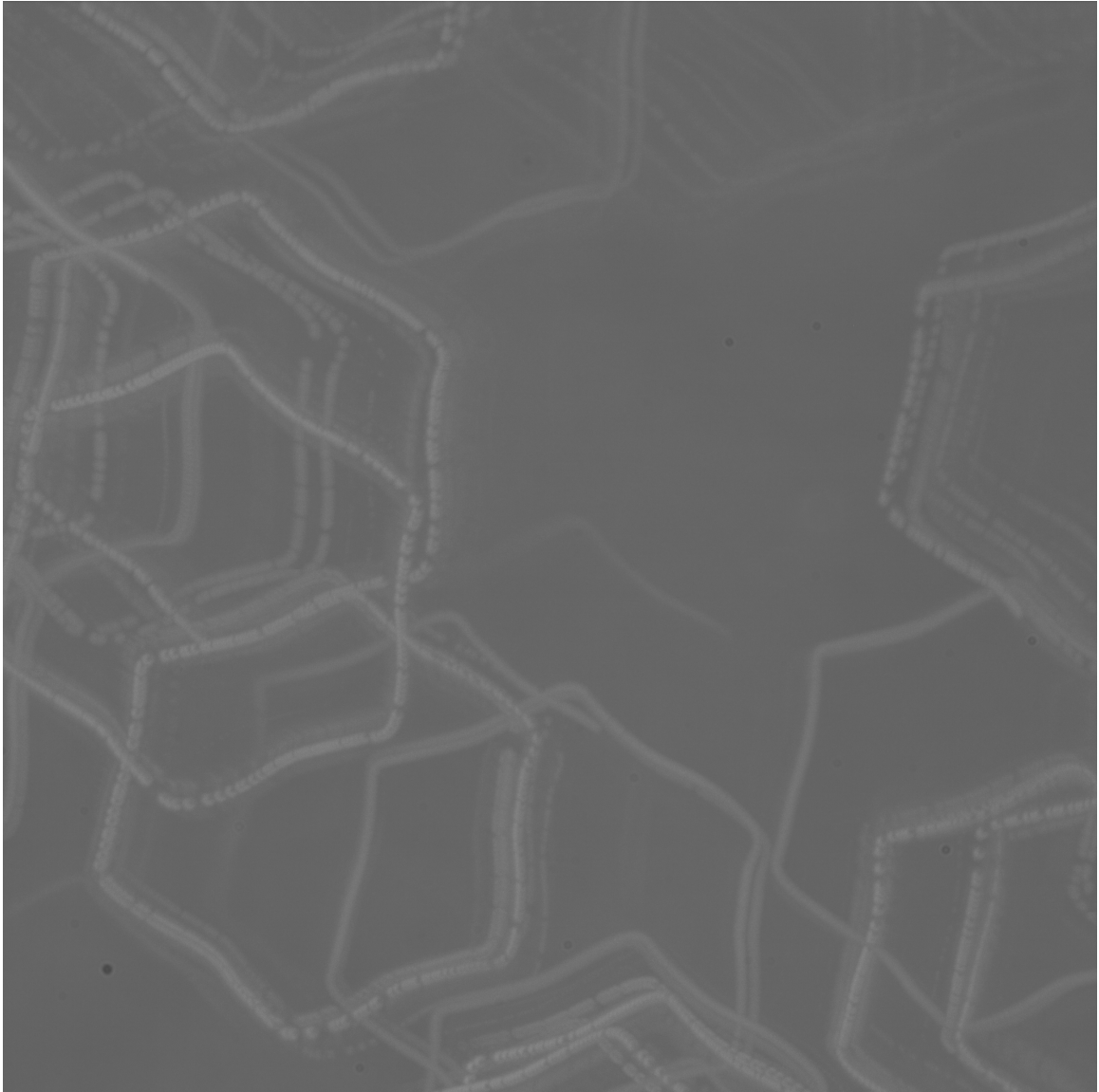
Figure 4.9: Time lapse image of 2 µm latex tracer particles moved inside microfluidic manipulator tracing out an experimentally integrated hexagon via conformal mapping. Window size is 188 µm × 188 µm.
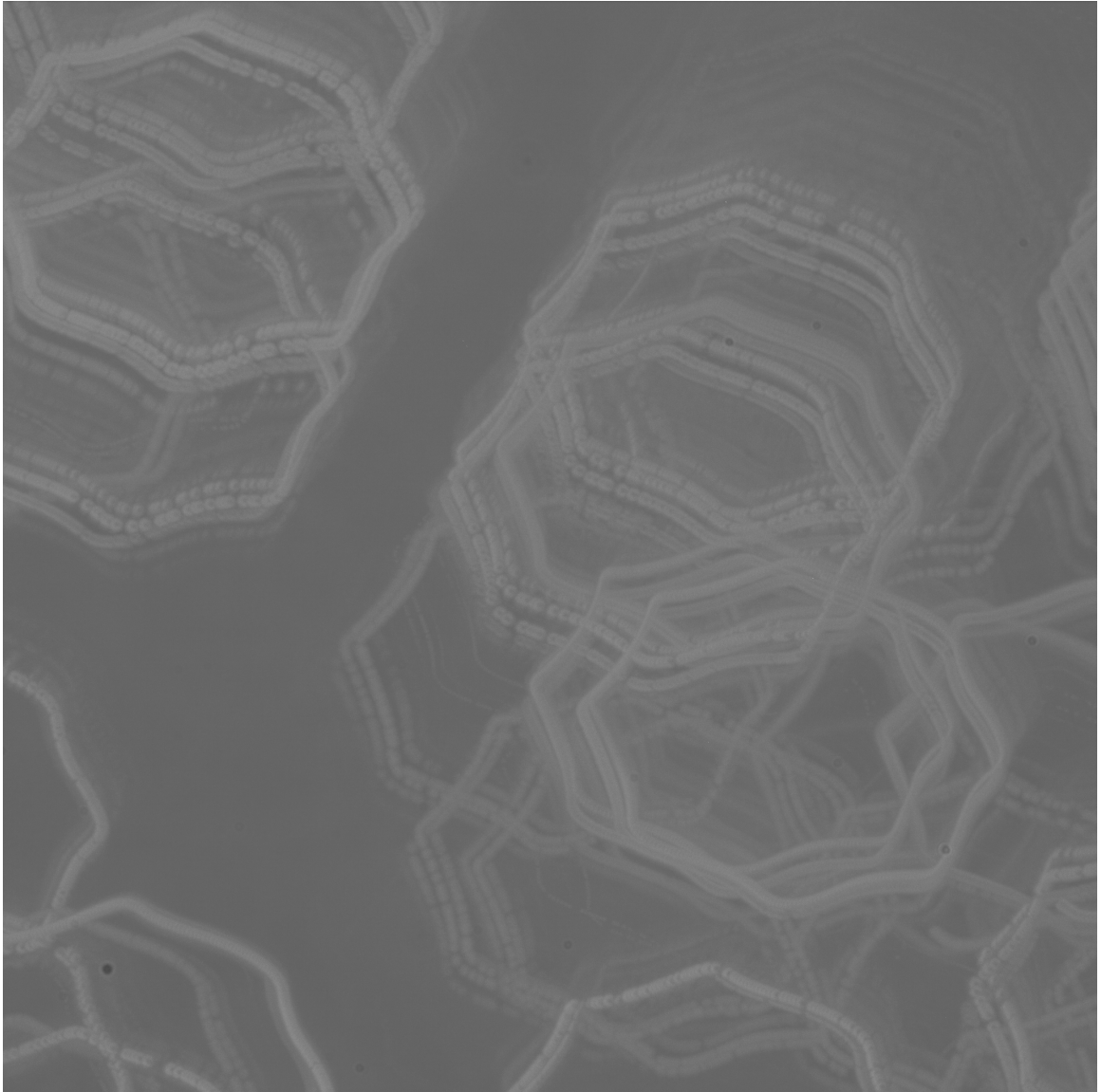
Figure 4.10: Time lapse image of 2 μm latex tracer particles moved inside microfluidic manipulator tracing out an experimentally integrated octagon via conformal mapping. Window size is 188 μm × 188 μm.

We anticipate the place of our microfluidic system to satisfy the ever increasing need for high throughput microfluidic systems[92, 93]. By its very nature our system can control large numbers of particles, manipulating the bulk fluid and hence all particles entrained within, and improvements to the control without implementing supervision to avoid delays would enhance its use for high throughput applications. Further, adding complexity with more microfluidic channels too has the potential to increase its usefulness by enabling further fine-tuning of the properties of the flow, enriching its capability beyond the present symmetry-protected separation of direction and strain.

Appendix A

Additional information for Symmetry-group-protected microfluidics for multiplexed stress-free manipulations

A.1   Experimental Methods

Microfluidic fabrication and its assembly for microscope observations. The microfluidic channel was fabricated as a stack of glass sheets (0.13 - 1 mm thick), with each containing a special pattern of channels. We made the design of these sheets through a computer assisted design (CAD) software (Autodesk Fusion 360), which were then sent to Citrogene for fabrications of these customized sheets in borosilicate glass and their integration into one single multilayer microfluidic chip (using optically clear adhesives). The overall exterior dimension of the microfluidic chip is compact, here, 62 mm × 22 mm × 2.7 mm in x, y, and z, comparable to the footprint of a typical glass slide. The chip was also designed to be self-enclosed, leaving only 6 small pores (1 mm in diameter) open for accessing the microfluidic flows. A 0.13 mm thick glass sheet at the bottom layer sealed the microfluidic channels and enabled high optical quality for conventional microscope observations. Before being connected to a multi-channel pump, the glass chip was mounted to a customized adapter for better sealing results.

Multiple-channel flow controls. Flows within the multilayer microfluidic channel were generated by two 4-channel microfluidic flow controllers (Elveflow OB1 MK3+) with each channel's pressure regulated independently between −0.9 and 1 bar relative to the atmospheric pressure. A custom program (written in Python) was used to modulate the pressures on each channel and record the microscope image in real time. To accommodate the finite resolution of our pressure controllers, here 120 μbar, we used a water-glycerol mixture to increase the viscosity of the fluid in the microfluidic channel, which maintained the flow speed within a reasonable range for microscope observations while using a decent fraction of the pressure range.

Microscope imaging and three-dimensional flow reconstructions. The microfluidic flows were visualized by mixing the fluid with polystyrene beads (2 μm in diameter) as seeding particles, imaged under an inverted microscope (Nikon Eclipse Ti2) at a 60× magnification, operated in its phase-contrast mode. These phase-contrast images were recorded by a USB Scientific CMOS (sCMOS) video camera (Andor Zyla 4.2) in full resolution (2048 × 2048 pixels) at 50 frames per second (FPS). The diffraction pattern of each seeding particle was visible within a range of 160 μm along the optical axis, which were calibrated to restore the axial positions of all seeding particles in the view [94], forming a sizable (at least 200 μm × 200 μm × 100 μm) visible zone of the 3D flow field.
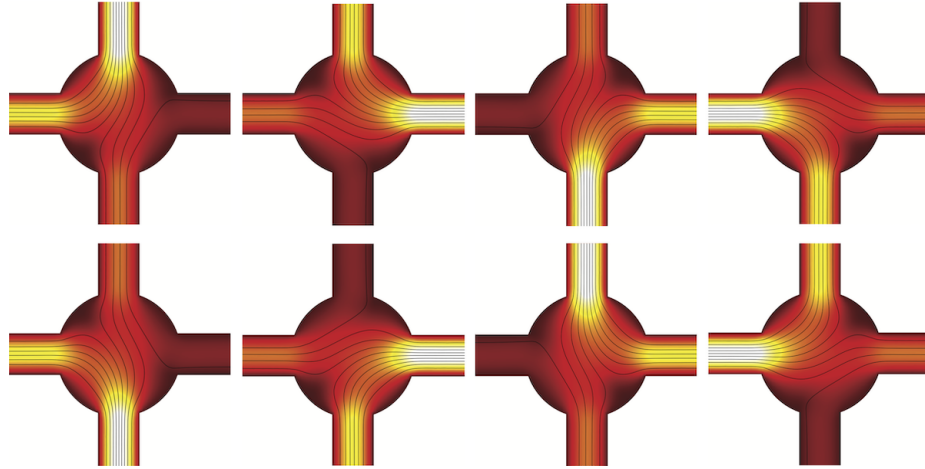
Figure A.1: Symmetry in a four-channel microfluidic junction. A total of eight equivalent flow patterns (regardless of rotation and reflection) are accessible in the same microfluidic junction, representing a D4 symmetry.

A.2   Microfluidic representations of symmetry groups

The possible ways of generating essentially equivalent follow patterns (regarding their functions) define the symmetry of a microfluidic device. For instance, a random flow (with the same pattern) can be generated in a total of eight different ways in a 4-channel cross junction (Supplementary Fig. A.1). These eight ways compose the symmetry group of a dihedral-4 (D4) symmetry [95]. A subset within this group can also be arranged to form a smaller group of symmetry, a subgroup of the D4 group. For instance, either the upper or the lower row forms a cyclic-4 (C4) symmetry, with each element accessible through a 4-fold rotation. A pair of adjacent elements along the vertical or the horizontal direction forms a D1 subgroup (for the reflection symmetry along the horizontal axis). A pair of the adjacent elements along the diagonals also forms a D1 subgroup, however, for a reflection along a certain 45-degree axis.

A.3   Symmetries in the strain-rate invariant

We consider a junction in a microfluidic device actuated by a set of infinitesimal sources or sinks and ignore the detailed boundary condition. The flow can thus be characterized by a potential flow set by fluid sources [18]. For a 2D junction, the flow velocity $\mathbf{u}$ can be determined from a potential ϕ as [13, 63]

$$\mathbf{u}(\mathbf{r}) = \boldsymbol{\nabla}\phi(\mathbf{r}), \tag{A.1}$$

$$\phi(\mathbf{r}) = \sum_{i=1}^{N} q_i \ln(|\mathbf{r} - \mathbf{r}_i|), \tag{A.2}$$

where q_i and $\mathbf{r}_i = (x_i, y_i)$ are the magnitude and location of each source, respectively. Consequently,

$$\mathbf{u}(\mathbf{r}) = \sum_{i=1}^{N} q_i \frac{\mathbf{r} - \mathbf{r}_i}{|\mathbf{r} - \mathbf{r}_i|^2} \tag{A.3}$$

The rate of strain tensor of the flow is thus

$$\dot{\gamma} = \frac{1}{2}\left[\boldsymbol{\nabla}\mathbf{u} + (\boldsymbol{\nabla}\mathbf{u})^{\top}\right] \tag{A.4}$$

$$\dot{\gamma} = \sum_{i=1}^{N} \frac{q_i}{|\mathbf{r} - \mathbf{r}_i|^2} \left[\mathbf{I} - 2\frac{(\mathbf{r} - \mathbf{r}_i)(\mathbf{r} - \mathbf{r}_i)}{|\mathbf{r} - \mathbf{r}_i|^2} \right] \tag{A.5}$$

Since a function of a microfluidic device should be independent of the choice of coordinates, we consider the invariant of the rate of strain tensor [72]. The first non-trivial invariant is its second-order invariant

$$I_2 = -\frac{1}{2}\text{Tr}(\dot{\gamma}^2) \tag{A.6}$$

From the scaling, it can be shown that the invariant I_2 has a quadratic form of q_i, i.e.,

$$I_2(\mathbf{r}) = \mathbf{q}^{\top} \cdot \mathbf{L}(\mathbf{r}) \cdot \mathbf{q} = \sum_{i,j=1}^{N} L_{ij}(\mathbf{r} - \mathbf{r}_i, \mathbf{r} - \mathbf{r}_j)q_i q_j. \tag{A.7}$$

where L_{ij} is a function of $\mathbf{r} - \mathbf{r}_i$ and $\mathbf{r} - \mathbf{r}_j$, which can be obtained explicitly by the above expressions.

Explicit construction of the second-order invariant is straightforward. Squaring Eq. A.5, we find

$$\dot{\gamma}^2 = \sum_{i,j} \frac{q_i q_j}{|\mathbf{r} - \mathbf{r}_i|^2 |\mathbf{r} - \mathbf{r}_j|^2} \left[\mathbf{I} - 2\frac{(\mathbf{r} - \mathbf{r}_i)(\mathbf{r} - \mathbf{r}_i)}{|\mathbf{r} - \mathbf{r}_i|^2} - 2\frac{(\mathbf{r} - \mathbf{r}_j)(\mathbf{r} - \mathbf{r}_j)}{|\mathbf{r} - \mathbf{r}_j|^2} \right.$$
$$\left. +4\frac{(\mathbf{r} - \mathbf{r}_i)(\mathbf{r} - \mathbf{r}_i) \cdot (\mathbf{r} - \mathbf{r}_j)(\mathbf{r} - \mathbf{r}_j)}{|\mathbf{r} - \mathbf{r}_i|^2 |\mathbf{r} - \mathbf{r}_j|^2} \right]. \tag{A.8}$$

Then, taking the trace we conclude:

$$I_2 = -\frac{1}{2}\text{Tr}\left(\dot{\gamma}^2\right) = \sum_{i,j} -\frac{q_i q_j}{2 |\mathbf{r} - \mathbf{r}_i|^2 |\mathbf{r} - \mathbf{r}_j|^2} \left[-1 + 4\frac{[(\mathbf{r} - \mathbf{r}_i) \cdot (\mathbf{r} - \mathbf{r}_j)]^2}{|\mathbf{r} - \mathbf{r}_i|^2 |\mathbf{r} - \mathbf{r}_j|^2} \right]. \tag{A.9}$$

Finding those independent flow modes (functions) thus becomes an eigenvalue problem. The symmetries of a microfluidic junction are embedded in the $\mathbf{L}(\mathbf{r})$ matrix. We consider here the invariant at the center of the junction, $I_2(\mathbf{0})$, where most symmetries in a device must apply.

For fluid sources lying on the four corners of a square, the matrix $\mathbf{L}(\mathbf{0})$ complies with the symmetries of a square, i.e., the D_4 group. The $\mathbf{L}(\mathbf{0})$ matrix that satisfies this symmetry group can be represented by

$$\mathbf{L}(\mathbf{0}) = \begin{bmatrix} 0 & a & b & a \\ a & 0 & a & b \\ b & a & 0 & a \\ a & b & a & 0 \end{bmatrix} \tag{A.10}$$

Such a matrix belongs to the category of circulant matrices [96], and the eigenvectors are expressed in the following:

$$v_1 = \frac{1}{\sqrt{2}}(1, 0, -1, 0)$$

$$v_2 = \frac{1}{\sqrt{2}}(0, 1, 0, -1)$$

$$v_3 = \frac{1}{2}(1, -1, 1, -1)$$

$$v_4 = \frac{1}{2}(1, 1, 1, 1)$$

Here, the first two modes are degenerate, corresponding to two dipole moments in orthogonal directions. The third mode corresponds to a quadrupole. The fourth mode is trivial and is excluded due to its contradiction with the continuity condition (for incompressible flows). It is worth noting that the diagonal zeros in $\mathbf{L}(0)$ can be replaced by any values, which only offset all eigenvalues by a constant.

The matrix $\mathbf{L}(0)$ can be explicitly found. We take as a choice of fluid locations a radial displacement $l/\sqrt{2}$ (for a square with lateral length l)

$$\mathbf{r}_1 = l/\sqrt{2}\hat{x} \tag{A.11}$$

$$\mathbf{r}_2 = l/\sqrt{2}\hat{y} \tag{A.12}$$

$$\mathbf{r}_3 = -l/\sqrt{2}\hat{x} \tag{A.13}$$

$$\mathbf{r}_4 = -l/\sqrt{2}\hat{y}. \tag{A.14}$$

From Eq. A.9, these locations yield

$$\mathbf{L}(0) = -\frac{2}{l^4}\begin{bmatrix} 3 & -1 & 3 & -1 \\ -1 & 3 & -1 & 3 \\ 3 & -1 & 3 & -1 \\ -1 & 3 & -1 & 3 \end{bmatrix} \tag{A.15}$$

$$= -\frac{2}{l^4}\left(3\mathbf{I} + \begin{bmatrix} 0 & -1 & 3 & -1 \\ -1 & 0 & -1 & 3 \\ 3 & -1 & 0 & -1 \\ -1 & 3 & -1 & 0 \end{bmatrix}\right), \tag{A.16}$$

thus matching the anticipated form of Eq. A.10 with an additional constant multiple of the identity matrix.
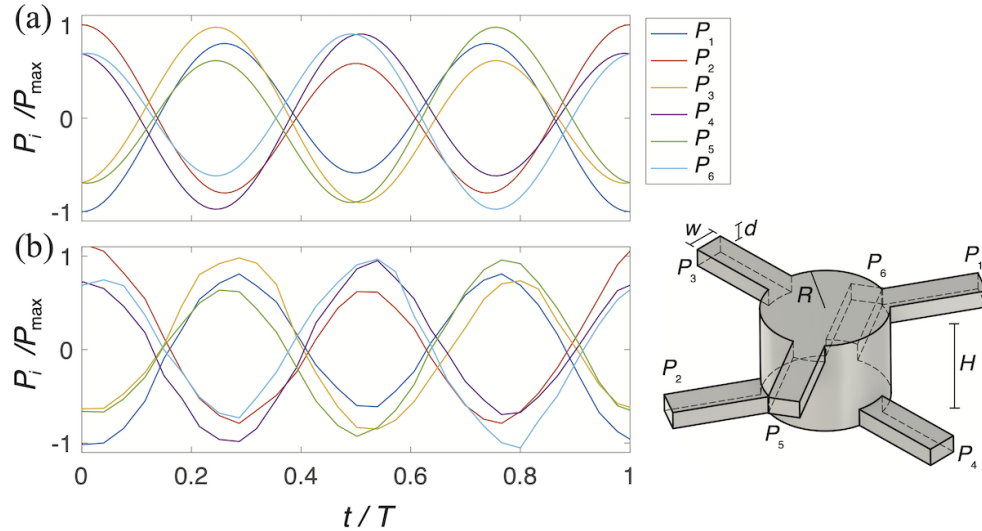
Figure A.2: Pressure regulations for stress-free microfluidic flows. (a) Six smooth time-dependent pressure curves P_1 - P_6, normalized by the maximal pressure $P_{max} = 11$ mbar, were designed (as functions of time t) and applied to a 6-channel microfluidic device (inset). Here, the curves correspond to the ideal ones for generating a 3D Lissajous flow (with a period $T = 8$ s). (b) The actual pressures monitored (by the pressure regulator) during the experiment show a consistent pattern.

A.4 Dynamic stress-free flow generations

To realize a dynamic stress-free flow pattern, we superimpose the three orthogonal dipole-flow modes along the principal axes of an octahedron [x, y, and z in Fig. 3.4a], with their coefficients (c_1, c_2, c_3) determined in the 3D phase space. On octahedral vertices, the charge assignments for these three orthogonal dipoles are respectively $(-1, 1, 0, 0, 0, 0)$, $(0, 0, -1, 1, 0, 0)$, and $(0, 0, 0, 0, -1, 1)$, corresponding to the pressure setting on six microfluidic ports. Since the axes of the microscope observation [x', y', and z' in Fig. 3.4a] are along the unit vectors $\frac{1}{\sqrt{6}}(2, -1, -1)$, $\frac{1}{\sqrt{2}}(0, 1, -1)$, and $\frac{1}{\sqrt{3}}(1, 1, 1)$ respectively in the phase space, the corresponding pressure settings $(\mathbf{P}_{x'}, \mathbf{P}_{y'}, \mathbf{P}_{z'})$ for three orthogonal flow modes along these directions are given by

$$
\begin{pmatrix} \mathbf{P}_{x'} \\ \mathbf{P}_{y'} \\ \mathbf{P}_{z'} \end{pmatrix} = \begin{pmatrix} \frac{1}{\sqrt{6}} & 0 & 0 \\ 0 & \frac{1}{\sqrt{2}} & 0 \\ 0 & 0 & \frac{1}{\sqrt{3}} \end{pmatrix} \cdot \begin{pmatrix} 2 & -1 & -1 \\ 0 & 1 & -1 \\ 1 & 1 & 1 \end{pmatrix} \cdot \begin{pmatrix} -1 & 1 & 0 & 0 & 0 & 0 \\ 0 & 0 & -1 & 1 & 0 & 0 \\ 0 & 0 & 0 & 0 & -1 & 1 \end{pmatrix}
$$

$$
= \begin{pmatrix} \frac{1}{\sqrt{6}} & 0 & 0 \\ 0 & \frac{1}{\sqrt{2}} & 0 \\ 0 & 0 & \frac{1}{\sqrt{3}} \end{pmatrix} \cdot \begin{pmatrix} -2 & 2 & 1 & -1 & 1 & -1 \\ 0 & 0 & -1 & 1 & 1 & -1 \\ -1 & 1 & -1 & 1 & -1 & 1 \end{pmatrix}. \tag{A.17}
$$

For a stress-free flow at given velocity $\mathbf{v}(t) = (v_{x'}, v_{y'}, v_{z'})$, the pressures on six ports $\mathbf{P}(t) = (P_1(t), P_2(t), \cdots, P_6(t))$ can be expressed as

$$
\mathbf{P}(t) = \mathbf{v}(t)^\top \cdot \begin{pmatrix} \sigma_{x'} & 0 & 0 \\ 0 & \sigma_{y'} & 0 \\ 0 & 0 & \sigma_{z'} \end{pmatrix} \cdot \begin{pmatrix} \mathbf{P}_{x'} \\ \mathbf{P}_{y'} \\ \mathbf{P}_{z'} \end{pmatrix}, \tag{A.18}
$$

where the middle diagonal matrix is the resistance matrix of the channel at the center region. It can be easily shown that these diagonal elements ($\sigma_{x'}, \sigma_{y'}, \sigma_{z'}$) are identical for perfect octahedral symmetries. *In situ*, these elements are expected to be subjected to boundary geometries and detailed fluid properties, which can be calibrated experimentally. In our microfluidic system, these geometries (illustrated in the inset of Supplementary Fig. A.2) are given by the radius ($R = 1$ mm) and height ($H = 1.6$ mm) of the middle cylindrical chamber and the cross section ($w \times d = 0.5 \times 0.3$ mm^2) of the channels. For the glycerol solution (99.6%) used in this experiment, the corresponding resistance matrix elements are $\sigma_{x'} \approx 0.22$ mbar·s/μm, $\sigma_{y'} \approx 0.19$ mbar·s/μm, and $\sigma_{z'} \approx 0.68$ mbar·s/μm. We attribute this significantly higher resistance along the axial (z') direction to the higher constraints that were applied to the axial flows by the noslip top and bottom surfaces of the cylindrical chamber.

To demonstrate the capability of such stress-free flows for dynamic manipulations, we use the above algorithm to determine the pressure setting $\mathbf{P}(t)$ for a time-dependent 3D flow velocity $\mathbf{v}(t)$. Using the 3D Lissajous flow as an example, its velocity can be prescribed by $\mathbf{v}(t) = (a\cos(\omega t), a\sin(\omega t), b\cos(2\omega t))$. Given the ratio b/a and the angular frequency ω (here, $b/a = 1.78$ and $\omega = 0.79$ rad/s), the pressures on every port are readily computed by the above equation (Eq. A.17), which are shown in Fig. A.2a. These computed pressure curves are fed into a USB-based multi-channel pressure regulator in real-time (controlled by a computer) through custom software. The actual pressures applied to the six ports of the microfluidic device are also measured by the regulator through the same software [Fig. A.2b], shown in great agreement with the previously computed values [Fig. A.2a].

Appendix B

4 channel Stokes wind tunnel work

The first geometry analyzed was the case of 4 channels, the simplest way to exert control with the two layer system. It was seen that for modes in plane with the channels, the streamlines extend smoothly through the center of the chamber (Fig. B.1a), indicating a low amount of shear present for the flow mode. Examining the change for shape deviations from an aspect ratio of unity, $\tilde{\gamma}_{xz}$ remains fairly uniformly $O(1)$ in the central region of the chamber (Fig. B.1b, and inset).
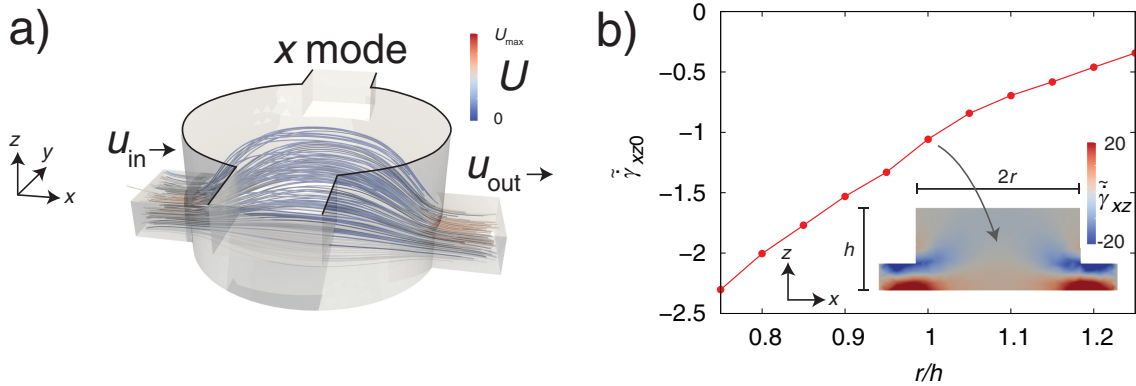
Figure B.1: a) Streamlines from FEM simulations of the 4 channel Stokes wind tunnel. Coloring denotes flow speed. Scale bar shows the range from 0 (blue) to maximum speed (red). Black lines along the upper side of the tunnel guide the reader's eye as to the shape. b) The resulting normalized shear strain rate component $\tilde{\gamma}_{xz}$ at the center of the chamber for the x-mode, for different aspect ratios. Inset shows relevant geometrical quantities and a cross section of the x-z plane of the tunnel. Scale bar shows $\tilde{\gamma}_{xz}$ for the cross section ranging from most negative (blue) to most positive (red). Grey arrow shows location of data point corresponding to center of inset.

Any spreading of flow lines, and hence the amount of shearing, could be controlled by constricting the region in which they may pass. By introducing cylindrically symmetric depressions to the top and bottom of the central chamber that preserve a flat surface, such shearing reduction may be achieved while still allowing for microscope observation (Fig. B.2a,b). Increasing the depth of these depressions does allow for a reduction in $\tilde{\gamma}_{xz}$ to $O(0.1)$, again for a fairly uniform region in the central chamber (Fig. B.2c).

Another chamber shape that preserves microscope viewability but still confines flow lines is achieved with partial depressions, here swept out only in line with the channels in the top and bottom layers (Fig. B.3a,b). Varying the depth leads to $\tilde{\gamma}_{xz}$ in the range of $O(0.1 - 1)$ through a fairly uniform region (Fig. B.3c).

B.1 4 channel symmetry analysis

We here present symmetry analysis for the 4 channel system in like manner to that in our previous work for the 6 channel case[17]. Beginning with the x-flow mode, we derive two sets of flow field equalities. The first set comes from taking the 4 channel system and performing a reflection about the x-z plane, under which no change is made to the flow field:

$$\begin{cases} u(x,y,z) = u(x,-y,z), \\ v(x,y,z) = -v(x,-y,z), \\ w(x,y,z) = w(x,-y,z). \end{cases} \tag{B.1}$$

The second set comes from a reflection about the y-z plane, followed by time reversal which brings the flow field back to its original configuration:

$$\begin{cases} u(x,y,z) = u(-x,y,z), \\ v(x,y,z) = -v(-x,y,z), \\ w(x,y,z) = -w(-x,y,z). \end{cases} \tag{B.2}$$

From these two sets of flow field equalities it is found that, for the velocity, only the u component survives at the center while v and w vanish. For the strain rate tensor, only $\dot{\gamma}_{xz}$ survives while all other components vanish.

Next we analyze the 4 channel y-flow mode. With a y-z plane reflection under which no change is made to the flow field, we have

$$\begin{cases} u(x,y,z) = -u(-x,y,z), \\ v(x,y,z) = v(-x,y,z), \\ w(x,y,z) = -w(-x,y,z). \end{cases} \tag{B.3}$$

Then, with an x-z plane reflection followed by a time reversal under which no change is made to the flow field, we have

$$\begin{cases} u(x,y,z) = -u(-x,y,z), \\ v(x,y,z) = v(-x,y,z), \\ w(x,y,z) = -w(-x,y,z). \end{cases} \tag{B.4}$$

From these two sets of flow field equalities it is found that, for the velocity, only the v component survives at the center while u and w vanish. For the strain rate tensor, only $\dot{\gamma}_{yz}$ survives while all other components vanish.

Finally we analyze the 4 channel z-flow mode. With a y-z plane reflection under which no change is made to the flow field, we have

$$\begin{cases} u(x,y,z) = -u(x,y,z), \\ v(x,y,z) = v(-x,y,z), \\ w(x,y,z) = w(-x,y,z). \end{cases} \tag{B.5}$$

Then, with an x-z plane reflection under which no change is made to the flow field, we have

$$\begin{cases} u(x,y,z) = u(x,-y,z), \\ v(x,y,z) = -v(x,-y,z), \\ w(x,y,z) = w(x,-y,z). \end{cases} \tag{B.6}$$

Finally, with a rotation about the line $y = x, z = 0$ followed by time reversal under which no change is made to the flow field, we have

$$\begin{cases} u(x,y,z) = u(y,x,-z), \\ v(x,y,z) = v(y,x,-z), \\ w(x,y,z) = w(x,y,-z). \end{cases} \tag{B.7}$$

From these three sets of flow field equalities it is found that, for the velocity, only the w component survives at the center while u and v vanish. For the strain rate tensor, only $\dot{\gamma}_{xx}$ and $\dot{\gamma}_{yy}$ survive while all other components vanish.

B.2   Source and sink activation strategy derivation

For the 4 channel case we use pairs of sources and sinks to derive the activation strategies, but we cannot take the pairs to be radial opposites of each other because the vertices of the tetrahedral arrangement do not possess that symmetry as the octahedron had. As such, we must use all point sources/sinks in the calculation rather than just working with the pertinent half as in Chapter 4. Their locations are taken to be

$$\mathbf{r}'_1 = a\hat{x} - b\hat{z} \tag{B.8}$$

$$\mathbf{r}'_2 = a\hat{y} + b\hat{z} \tag{B.9}$$

$$\mathbf{r}'_3 = -a\hat{x} - b\hat{z} \tag{B.10}$$

$$\mathbf{r}'_4 = -a\hat{y} + b\hat{z}. \tag{B.11}$$

For the case of point sources having opposing sinks, we take W.L.O.G. $m_3 = -m_1$ and $m_4 = -m_2$. From Eq. 4.3, setting it equal to the direction of flow velocity $u_d\hat{x} + v_d\hat{y} + w_d\hat{z}$, we arrive at the proportionality

$$(m_1, m_2) \propto -\frac{u}{2a}(1,0) - \frac{v}{2a}(0,1). \tag{B.12}$$

With the same conditions, Eq. 4.4 equated to some strain rate tensor

$$\dot{\gamma}_{xxd}\hat{x}\hat{x} + \dot{\gamma}_{xyd}\hat{x}\hat{y} + \dot{\gamma}_{xzd}\hat{x}\hat{z} + \dot{\gamma}_{yxd}\hat{y}\hat{x} + \dot{\gamma}_{yyd}\hat{y}\hat{y} + \dot{\gamma}_{yzd}\hat{x}\hat{z} + \dot{\gamma}_{zxd}\hat{z}\hat{x} + \dot{\gamma}_{zyd}\hat{z}\hat{y} + \dot{\gamma}_{zzd}\hat{z}\hat{z} \tag{B.13}$$

gives

$$(m_1, m_2) \propto \frac{\dot{\gamma}_{xzd}}{2ab}(1,0) - \frac{\dot{\gamma}_{yzd}}{2ab}(0,1). \tag{B.14}$$

Now we consider the case of point sources having opposing sources, W.L.O.G. $m_3 = m_1$ and $m_4 = m_2$. Following an identical procedure, we arrive first at the result for velocity,

$$2b(m_1 - m_2) \propto w_d. \tag{B.15}$$

We momentarily move on to the strain rate tensor result,

$$-2m_1 a^2 = \dot{\gamma}'_{xxd} \tag{B.16}$$

$$-2m_2 a^2 = \dot{\gamma}'_{yyd} \tag{B.17}$$

$$-2m_1 b^2 - 2m_2 b^2 = \dot{\gamma}'_{zzd}, \tag{B.18}$$

where the primes denote proportionality to the original unprimed components by an identical factor. Noting the traceless nature of the strain rate tensor, the sum of all three equations gives

$$m_1 + m_2 = 0, \tag{B.19}$$

hence Eq. B.18 is trivially null on the left hand side, prohibiting any activation strategy from yielding that component. The requisite activation strategy by Eq. B.19, $(m_1, m_2) \propto (1, -1)$, thus has the components $\dot{\gamma}_{xxd}$ and $\dot{\gamma}_{yyd}$ (c.f. Eq.s B.16 and B.17). This activation strategy, by Eq. B.15, only activates the w_d component.
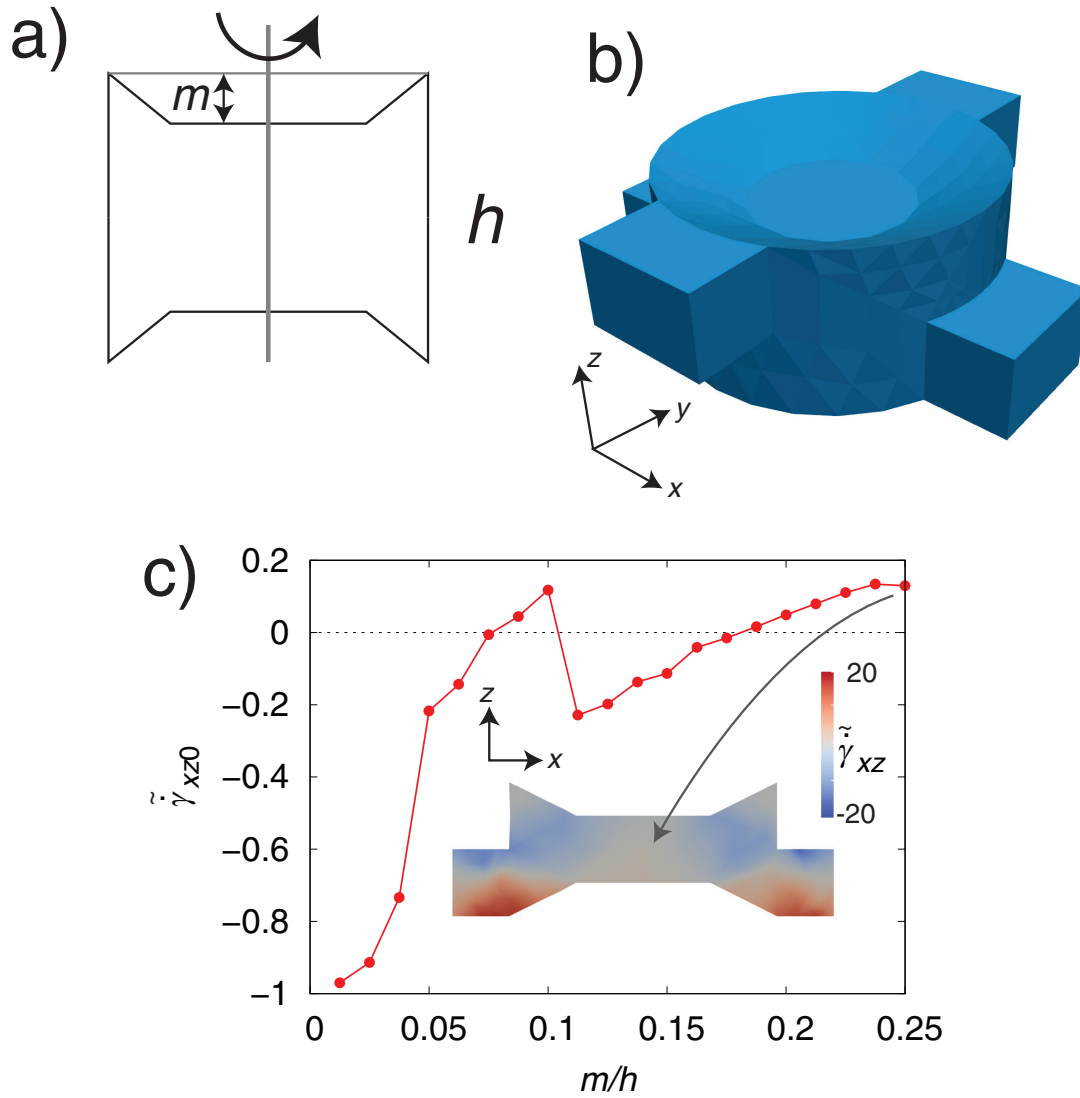
Figure B.2: a) Outline showing the relevant geometric quantities of a cross section of the depressed tunnel. Black lines show cross section that is symmetric about the vertical grey line axis. Depression depth is measured from the top of the depression marked by the horizontal grey line. b) 3-dimensional version of the symmetric depression geometry. The same depression viewed in the top is present in the bottom of the tunnel (not visible). c) The resulting normalized shear strain rate component $\tilde{\dot{\gamma}}_{xz}$ at the center of the chamber for the x-mode, for different aspect ratios. Inset shows relevant geometrical quantities and a cross section of the x-z plane of the tunnel. Scale bar shows $\tilde{\dot{\gamma}}_{xz}$ for the cross section ranging from most negative (blue) to most positive (red). Grey arrow shows location of data point corresponding to center of inset.
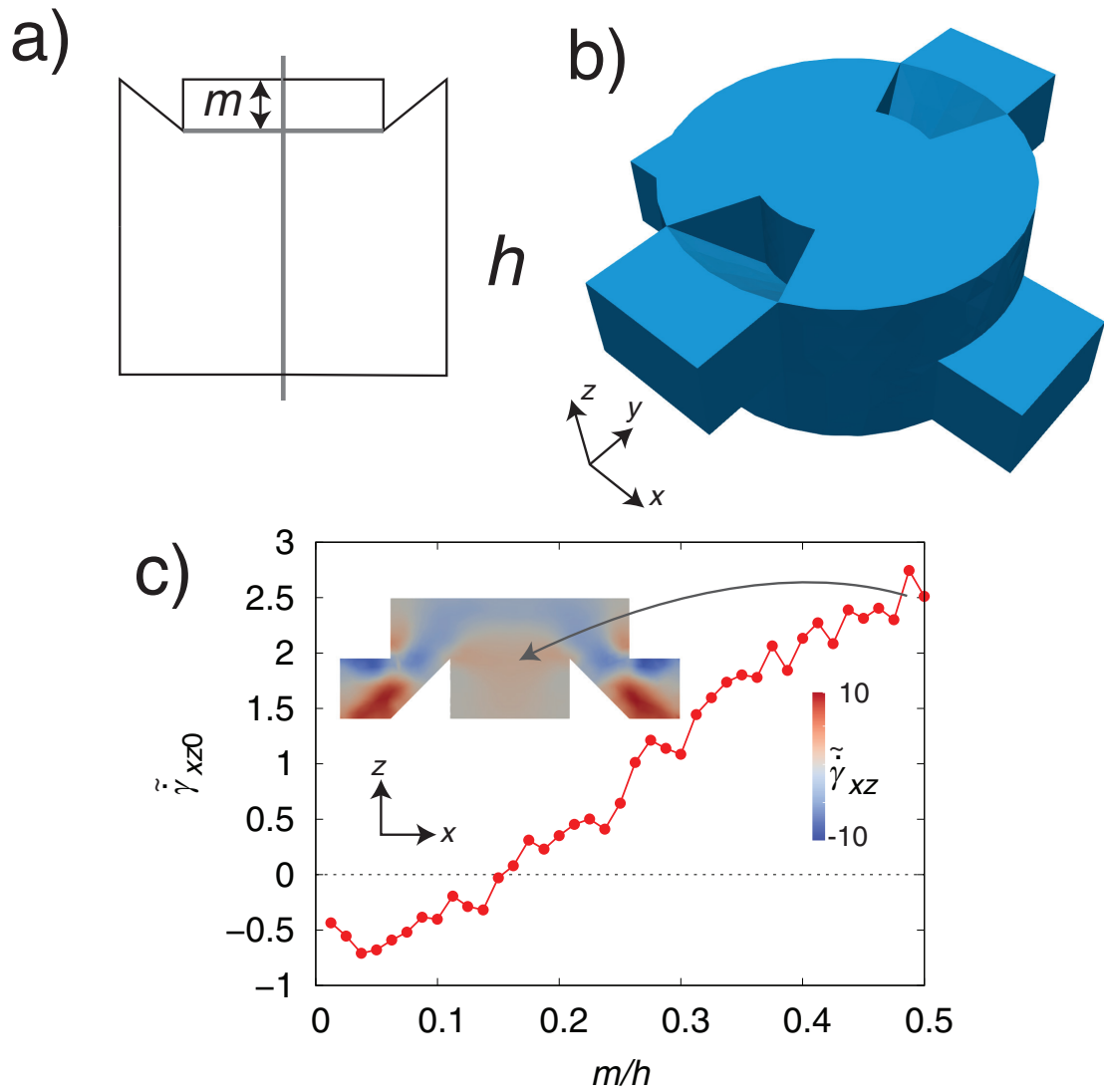
Figure B.3: a) Outline showing the relevant geometric quantities of one cross section of the partially depressed tunnel. Black lines show a cross section that is partially symmetric about the vertical grey line axis. Depression depth is measured from the bottom of the depression marked by the horizontal grey line. b) 3-dimensional version of the symmetric depression geometry. The same depression viewed in the top is present, but rotated about 90°, in the bottom of the tunnel (not visible). c) The resulting normalized shear strain rate component $\tilde{\dot{\gamma}}_{xz}$ at the center of the chamber for the x-mode, for different aspect ratios. Inset shows relevant geometrical quantities and a cross section of the x-z plane of the tunnel. Scale bar shows $\tilde{\dot{\gamma}}_{xz}$ for the cross section ranging from most negative (blue) to most positive (red). Grey arrow shows location of data point corresponding to center of inset.

Appendix C

Additional 6 channel symmetry arguments

In addition to the 6 channel symmetry arguments presented in our previous work[17], we present here the arguments showing the modes are symmetry protected to perform their respective functions, three strainless modes each having a single component of velocity activated at the center and two strainful modes each having both no components of velocity and mutually exclusive components of the rate of strain tensor activated at the center. We refer the reader to our conventions as described in Chapter 2.

We first address the y-flow mode as it will be useful for further analysis. Restating one set of velocity relations for the y-flow mode as derived in our previous work, we have

$$\begin{cases} u(x, y, z) = -u(-x, y, -z), \\ v(x, y, z) = v(-x, y, -z), \\ w(x, y, z) = -w(-x, y, -z). \end{cases} \tag{C.1}$$

Trivially, then, at the center of the device, $(x, y, z) = (0, 0, 0)$, we have $u(0, 0, 0) = w(0, 0, 0) = 0$. Thus the y-flow mode is protected by symmetry, only ever allowing the possibility of a nonzero v component at the center.

Having established those relations, we use them to address the x-flow mode. We note that the x-flow mode can be viewed as the superposition of two y-like modes: One by taking the y-flow mode rotated by $-120°$ about the z-axis, and one by taking the y-flow mode mirrored about the y-z plane and rotated $-60°$ about the z-axis. Each of those y-like modes will possess the same two null flow components, the w component and the relative u component after the specified transformations, at the center as the original y-flow mode. Respectively, the only nonzero components allowed point in the $-60°$ and $60°$ directions in the x-y plane. Hence, the superposition will also have the superposition of those components, perfectly cancelling out the v component and leaving behind only the u component. Thus the x-flow mode is protected by symmetry, only ever allowing the possibility of a nonzero u component at the center.

Next we address the z-flow mode. We assume the x-y component of the flow field at the origin points in an arbitrary direction. Then we rotate the chamber by $120°$ about the z-axis, thus rotating with it the direction of the in-plane vector by $120°$. However, under that rotation the flow configuration is identical to the original position. Hence, there can be no x-y component, $u(0, 0, 0) = v(0, 0, 0) = 0$. The z-flow mode is protected by symmetry, only ever allowing the possibility of a nonzero w component at the center. This completes the description of symmetry protection for the three directional modes, as the previous work covers their null strain rate tensor components at the center.

We add one final detail regarding the opposing x-flow mode. Following identical logic to the above argument for the null w component of the x-flow mode, we write the opposing x-flow mode as the superposition of two opposing y-like modes: One by taking the opposing y-flow mode rotated by $-120°$ about the z-axis, and one by taking the opposing y-flow mode mirrored about the y-z plane and rotated $-60°$ about the z-axis. Because each of those opposing y-like modes has a null $\dot{\gamma}_{zz}$ component, their superposition, not changing the flow

fields along the z-axis under reflection and rotations, must likewise have a null $\dot{\gamma}_{zz}$ component. This result tightens up our symmetry protected components of the strain rate tensor, complementing the abstracted flow analysis.

Bibliography

[1] Richard P Feynman. "Plenty of Room at the Bottom". In: *APS annual meeting*. Little Brown Boston, MA, USA. 1959, pp. 1–7.

[2] Chris Toumey. "Plenty of room, plenty of history". In: *Nature Nanotechnology* 4.12 (Dec. 2009), pp. 783–784. ISSN: 1748-3395. DOI: 10.1038/nnano.2009.357. URL: http://dx.doi.org/10.1038/nnano.2009.357.

[3] Matthew C. Asplund, Jeremy A. Johnson, and James E. Patterson. "The 2018 Nobel Prize in Physics: optical tweezers and chirped pulse amplification". In: *Analytical and Bioanalytical Chemistry* 411.20 (May 2019), pp. 5001–5005. ISSN: 1618-2650. DOI: 10.1007/s00216-019-01913-z. URL: http://dx.doi.org/10.1007/s00216-019-01913-z.

[4] Quang Minh Ta and Chien Chern Cheah. "Cooperative and mobile manipulation of multiple microscopic objects based on micro-hands and laser-stage control". In: *Automatica* 98 (2018), pp. 201–214. ISSN: 0005-1098. DOI: https://doi.org/10.1016/j.automatica.2018.09.011. URL: https://www.sciencedirect.com/science/article/pii/S0005109818304369.

[5] Fatih Akkoyun, Sinan Gucluer, and Adem Ozcelik. "Potential of the acoustic micromanipulation technologies for biomedical research". In: *Biomicrofluidics* 15.6 (Nov. 2021), p. 061301. ISSN: 1932-1058. DOI: 10.1063/5.0073596. eprint: https://pubs.aip.org/aip/bmf/article-pdf/doi/10.1063/5.0073596/13899769/061301_1_online.pdf. URL: https://doi.org/10.1063/5.0073596.

[6] Nadine Aubry and Pushpendra Singh. "Physics underlying controlled self-assembly of micro- and nanoparticles at a two-fluid interface using an electric field". In: *Phys. Rev. E* 77 (5 May 2008), p. 056302. DOI: 10.1103/PhysRevE.77.056302. URL: https://link.aps.org/doi/10.1103/PhysRevE.77.056302.

[7] Simone Schuerle et al. "Three-Dimensional Magnetic Manipulation of Micro- and Nanostructures for Applications in Life Sciences". In: *IEEE Transactions on Magnetics* 49.1 (2013), pp. 321–330. DOI: 10.1109/TMAG.2012.2224693.

[8] Zhuang Zhi Chong et al. "Active droplet generation in microfluidics". In: *Lab Chip* 16 (1 2016), pp. 35–58. DOI: 10.1039/C5LC01012H. URL: http://dx.doi.org/10.1039/C5LC01012H.

[9] Daniel Therriault, Scott R. White, and Jennifer A. Lewis. "Chaotic mixing in three-dimensional microvascular networks fabricated by direct-write assembly". In: *Nature Materials* 2.4 (Mar. 2003), pp. 265–271. ISSN: 1476-4660. DOI: 10.1038/nmat863. URL: http://dx.doi.org/10.1038/nmat863.

[10] Anamika Maurya et al. "Microfluidics geometries involved in effective blood plasma separation". In: *Microfluidics and Nanofluidics* 26.10 (Sept. 2022). ISSN: 1613-4990. DOI: 10.1007/s10404-022-02578-4. URL: http://dx.doi.org/10.1007/s10404-022-02578-4.

[11] Geoffrey Ingram Taylor. "The formation of emulsions in definable fields of flow". In: *Proceedings of the Royal Society of London. Series A, Containing Papers of a Mathematical and Physical Character* 146.858 (1934), pp. 501–523. DOI: 10.1098/rspa.1934.0169. eprint: https://royalsocietypublishing.org/doi/pdf/10.1098/rspa.1934.0169. URL: https://royalsocietypublishing.org/doi/abs/10.1098/rspa.1934.0169.

[12] S. D. Hudson et al. "Microfluidic analog of the four-roll mill". In: *Applied Physics Letters* 85.2 (July 2004), pp. 335–337. ISSN: 0003-6951. DOI: `10.1063/1.1767594`. eprint: `https://pubs.aip.org/aip/apl/article-pdf/85/2/335/18590948/335\_1\_online.pdf`. URL: `https://doi.org/10.1063/1.1767594`.

[13] Anish Shenoy, Christopher V. Rao, and Charles M. Schroeder. "Stokes trap for multiplexed particle manipulation and assembly using fluidics". In: *Proceedings of the National Academy of Sciences* 113.15 (Apr. 2016), pp. 3976–3981. ISSN: 0027-8424, 1091-6490. DOI: `10.1073/pnas.1525162113`. URL: `http://www.pnas.org/lookup/doi/10.1073/pnas.1525162113` (visited on 07/23/2017).

[14] Michael Q. Tu et al. "3D manipulation and dynamics of soft materials in 3D flows". en. In: *Journal of Rheology* 67.4 (2023), p. 877. ISSN: 0148-6055, 1520-8516. DOI: `10.1122/8.0000600`. (Visited on 08/09/2023).

[15] K Svoboda and S M Block. "Biological Applications of Optical Forces". In: *Annual Review of Biophysics* 23.Volume 23, 1994 (1994), pp. 247–285. ISSN: 1936-1238. DOI: `https://doi.org/10.1146/annurev.bb.23.060194.001335`. URL: `https://www.annualreviews.org/content/journals/10.1146/annurev.bb.23.060194.001335`.

[16] Bin Liu and Jeremias Gonzalez. "Bundled slender-body theory for elongated geometries in swimming bacteria". In: *Phys. Rev. Fluids* 5 (5 May 2020), p. 053102. DOI: `10.1103/PhysRevFluids.5.053102`. URL: `https://link.aps.org/doi/10.1103/PhysRevFluids.5.053102`.

[17] Jeremias Gonzalez and Bin Liu. "Symmetry-based nonperturbative micromanipulation in a three-dimensional microfluidic device". en. In: *Physical Review Fluids* 5.4 (Apr. 2020), p. 044202. ISSN: 2469-990X. DOI: `10.1103/PhysRevFluids.5.044202`. URL: `https://link.aps.org/doi/10.1103/PhysRevFluids.5.044202` (visited on 08/09/2020).

[18] G. K. Batchelor. *An introduction to fluid dynamics*. Cambridge: Cambridge University Press, 2000. ISBN: 978-0-511-80095-5. DOI: `10.1017/CBO9780511800955`. URL: `http://ebooks.cambridge.org/ref/id/CBO9780511800955` (visited on 07/24/2019).

[19] E. M. Purcell. "Life at low Reynolds number". In: *American Journal of Physics* 45.1 (Jan. 1977), pp. 3–11. ISSN: 0002-9505. DOI: `10.1119/1.10903`. URL: `https://aapt.scitation.org/doi/abs/10.1119/1.10903` (visited on 01/15/2020).

[20] Gwynn J. Elfring and Eric Lauga. "Hydrodynamic phase locking of swimming microorganisms". In: *Physical Review Letters* 103.8 (Aug. 2009), p. 088101. DOI: `10.1103/PhysRevLett.103.088101`. URL: `https://link.aps.org/doi/10.1103/PhysRevLett.103.088101` (visited on 01/12/2020).

[21] Eric Lauga, Abraham D. Stroock, and Howard A. Stone. "Three-dimensional flows in slowly varying planar geometries". In: *Physics of Fluids* 16.8 (July 2004), pp. 3051–3062. ISSN: 1070-6631. DOI: `10.1063/1.1760105`. URL: `https://aip.scitation.org/doi/abs/10.1063/1.1760105` (visited on 01/15/2020).

[22] Xiaoxiao Xu, Zhenyu Li, and Arye Nehorai. "Finite element simulations of hydrodynamic trapping in microfluidic particle-trap array systems". In: *Biomicrofluidics* 7.5 (Sept. 2013), p. 054108. ISSN: 1932-1058. DOI: `10.1063/1.4822030`. URL: `http://aip.scitation.org/doi/10.1063/1.4822030` (visited on 01/11/2020).

[23] Pamela N. Nge, Chad I. Rogers, and Adam T. Woolley. "Advances in microfluidic materials, functions, integration, and applications". In: *Chemical Reviews* 113.4 (Apr. 2013), pp. 2550–2583. ISSN: 0009-2665. DOI: `10.1021/cr300337x`. URL: `https://doi.org/10.1021/cr300337x` (visited on 01/15/2020).

[24] Lorenzo Capretto et al. "Micromixing within microfluidic devices". In: *Microfluidics: Technologies and Applications*. Ed. by Bingcheng Lin. Topics in Current Chemistry. Berlin, Heidelberg: Springer, 2011, pp. 27–68. ISBN: 978-3-642-23050-9. DOI: `10.1007/128_2011_150`. URL: `https://doi.org/10.1007/128_2011_150` (visited on 01/15/2020).

[25] Eric Lauga and Thomas R Powers. "The hydrodynamics of swimming microorganisms". In: *Reports on Progress in Physics* 72.9 (Sept. 2009), p. 096601. ISSN: 0034-4885, 1361-6633. DOI: `10.1088/0034-4885/72/9/096601`. URL: `http://stacks.iop.org/0034-4885/72/i=9/a=096601?key=crossref.736a5c13368e75b7395f94099aead8e4` (visited on 04/12/2019).

[26] Keir C. Neuman and Steven M. Block. "Optical trapping". In: *Review of Scientific Instruments* 75.9 (Sept. 2004), pp. 2787–2809. ISSN: 0034-6748, 1089-7623. DOI: `10.1063/1.1785844`. URL: `http://aip.scitation.org/doi/10.1063/1.1785844` (visited on 01/11/2020).

[27] T. T. Perkins. "Single polymer dynamics in an elongational flow". In: *Science* 276.5321 (June 1997), pp. 2016–2021. ISSN: 00368075, 10959203. DOI: `10.1126/science.276.5321.2016`. URL: `http://www.sciencemag.org/cgi/doi/10.1126/science.276.5321.2016` (visited on 01/06/2020).

[28] Unė G. Būtaitė et al. "Indirect optical trapping using light driven micro-rotors for reconfigurable hydrodynamic manipulation". In: *Nature Communications* 10.1 (Mar. 2019), p. 1215. ISSN: 2041-1723. DOI: `10.1038/s41467-019-08968-7`. URL: `https://doi.org/10.1038/s41467-019-08968-7`.

[29] Krisna C. Bhargava, Bryant Thompson, and Noah Malmstadt. "Discrete elements for 3D microfluidics". In: *Proceedings of the National Academy of Sciences* 111.42 (Oct. 2014), pp. 15013–15018. ISSN: 0027-8424, 1091-6490. DOI: `10.1073/pnas.1414764111`. URL: `https://www.pnas.org/content/111/42/15013` (visited on 01/12/2020).

[30] Kevin Vittayarukskul and Abraham Phillip Lee. "A truly Lego ® -like modular microfluidics platform". In: *Journal of Micromechanics and Microengineering* 27.3 (Mar. 2017), p. 035004. ISSN: 0960-1317, 1361-6439. DOI: `10.1088/1361-6439/aa53ed`. URL: `http://stacks.iop.org/0960-1317/27/i=3/a=035004?key=crossref.335563c535b4c8352b8b15db271ce6c8` (visited on 01/04/2020).

[31] S. J. Haward et al. "Microfluidic analog of an opposed-jets device". In: *Applied Physics Letters* 114.22 (June 2019), p. 223701. ISSN: 0003-6951, 1077-3118. DOI: `10.1063/1.5097850`. URL: `http://aip.scitation.org/doi/10.1063/1.5097850` (visited on 06/19/2019).

[32] Christophe Geuzaine and Jean-François Remacle. "Gmsh: A 3-D finite element mesh generator with built-in pre- and post-processing facilities". In: *International Journal for Numerical Methods in Engineering* 79.11 (Sept. 2009), pp. 1309–1331. ISSN: 00295981, 10970207. DOI: `10.1002/nme.2579`. URL: `http://doi.wiley.com/10.1002/nme.2579` (visited on 06/20/2019).

[33] F. Hecht. "New development in freefem++". In: *Journal of Numerical Mathematics* 20.3-4 (Jan. 2012), pp. 251–266. ISSN: 1569-3953, 1570-2820. DOI: `10.1515/jnum-2012-0013`. URL: `https://www.degruyter.com/view/j/jnma.2012.20.issue-3-4/jnum-2012-0013/jnum-2012-0013.xml` (visited on 06/21/2019).

[34] Charles D. Hansen and Chris R. Johnson, eds. *The visualization handbook*. Amsterdam ; Boston: Elsevier-Butterworth Heinemann, 2005. ISBN: 978-0-12-387582-2.

[35] O. C. Zienkiewicz, Robert L. Taylor, and David Fox. *The finite element method for solid and structural mechanics*. 7th ed. Amsterdam ; Boston: Elsevier-Butterworth Heinemann, 2014. ISBN: 978-1-85617-634-7.

[36] A. Groisman and V. Steinberg. "Elastic turbulence in a polymer solution flow". In: *Nature* 405.6782 (May 2000), pp. 53–55. ISSN: 1476-4687. DOI: `10.1038/35011019`. URL: `https://www.nature.com/articles/35011019` (visited on 01/14/2020).

[37] P. E. Arratia et al. "Elastic instabilities of polymer solutions in cross-channel flow". In: *Physical Review Letters* 96.14 (Apr. 2006), p. 144502. DOI: `10.1103/PhysRevLett.96.144502`. URL: `https://link.aps.org/doi/10.1103/PhysRevLett.96.144502` (visited on 01/14/2020).

[38] Chia-Wen Chang et al. "A polydimethylsiloxane–polycarbonate hybrid microfluidic device capable of generating perpendicular chemical and oxygen gradients for cell culture studies". In: *Lab Chip* 14.19 (2014), pp. 3762–3772. ISSN: 1473-0197, 1473-0189. DOI: 10.1039/C4LC00732H. URL: http://xlink.rsc.org/?DOI=C4LC00732H (visited on 01/10/2020).

[39] Koji Sugioka and Ya Cheng. "Femtosecond laser three-dimensional micro- and nanofabrication". In: *Applied Physics Reviews* 1.4 (Dec. 2014), p. 041303. ISSN: 1931-9401. DOI: 10.1063/1.4904320. URL: http://aip.scitation.org/doi/10.1063/1.4904320 (visited on 01/10/2020).

[40] Ho Nam Chan et al. "Direct, one-step molding of 3D-printed structures for convenient fabrication of truly 3D PDMS microfluidic chips". In: *Microfluidics and Nanofluidics* 19.1 (July 2015), pp. 9–18. ISSN: 1613-4990. DOI: 10.1007/s10404-014-1542-4. URL: https://doi.org/10.1007/s10404-014-1542-4 (visited on 01/12/2020).

[41] George Barker Jeffery and Louis Napoleon George Filon. "The motion of ellipsoidal particles immersed in a viscous fluid". In: *Proceedings of the Royal Society of London. Series A* 102.715 (Nov. 1922), pp. 161–179. DOI: 10.1098/rspa.1922.0078. URL: https://royalsocietypublishing.org/doi/abs/10.1098/rspa.1922.0078 (visited on 01/14/2020).

[42] William M. Durham, John O. Kessler, and Roman Stocker. "Disruption of vertical motility by shear triggers formation of thin phytoplankton layers". In: *Science* 323.5917 (Feb. 2009), pp. 1067–1070. ISSN: 0036-8075, 1095-9203. DOI: 10.1126/science.1167334. URL: https://science.sciencemag.org/content/323/5917/1067 (visited on 01/14/2020).

[43] Marcos et al. "Bacterial rheotaxis". In: *Proceedings of the National Academy of Sciences* 109.13 (Mar. 2012), pp. 4780–4785. ISSN: 0027-8424, 1091-6490. DOI: 10.1073/pnas.1120955109. URL: https://www.pnas.org/content/109/13/4780 (visited on 01/14/2020).

[44] Jeremias Gonzalez, Ajay Gopinathan, and Bin Liu. "Symmetry-group-protected microfluidics". In: *Physical Review Research* (2024). In press.

[45] Todd M. Squires and Stephen R. Quake. "Microfluidics: Fluid physics at the nanoliter scale". en. In: *Reviews of Modern Physics* 77.3 (Oct. 2005), pp. 977–1026. ISSN: 0034-6861, 1539-0756. DOI: 10.1103/RevModPhys.77.977. URL: https://link.aps.org/doi/10.1103/RevModPhys.77.977 (visited on 07/29/2022).

[46] George M. Whitesides. "The origins and the future of microfluidics". en. In: *Nature* 442.7101 (July 2006), pp. 368–373. ISSN: 0028-0836, 1476-4687. DOI: 10.1038/nature05058. URL: http://www.nature.com/articles/nature05058 (visited on 07/15/2022).

[47] Daniel Mark et al. "Microfluidic lab-on-a-chip platforms: requirements, characteristics and applications". en. In: *Chemical Society Reviews* 39.3 (2010), p. 1153. ISSN: 0306-0012, 1460-4744. DOI: 10.1039/b820557b. URL: http://xlink.rsc.org/?DOI=b820557b (visited on 07/15/2022).

[48] Sarah Battat, David A. Weitz, and George M. Whitesides. "Nonlinear Phenomena in Microfluidics". en. In: *Chemical Reviews* 122.7 (Apr. 2022), pp. 6921–6937. ISSN: 0009-2665, 1520-6890. DOI: 10.1021/acs.chemrev.1c00985. URL: https://pubs.acs.org/doi/10.1021/acs.chemrev.1c00985 (visited on 07/15/2022).

[49] Andreas Manz et al. "Planar chips technology for miniaturization and integration of separation techniques into monitoring systems". en. In: *Journal of Chromatography A* 593.1-2 (Feb. 1992), pp. 253–258. ISSN: 00219673. DOI: 10.1016/0021-9673(92)80293-4. URL: https://linkinghub.elsevier.com/retrieve/pii/0021967392802934 (visited on 07/29/2022).

[50] X. Mao, J. R/ Waldeisen, and T. J. Huang. ""Microfluidic drifting"–implementing three-dimensional hydrodynamic focusing with a single-layer planar microfluidic device". English. In: *Lab on a Chip* 7.10 (2007), p. 1260. ISSN: 1473-0197, 1473-0189. DOI: 10.1039/b711155j.

[51]   K. Drescher et al. "Biofilm streamers cause catastrophic disruption of flow with consequences for environmental and medical systems". English. In: *Proceedings of the National Academy of Sciences of the United States of America* 110.11 (Mar. 2013), pp. 4345–4350. ISSN: 0027-8424, 1091-6490. DOI: 10.1073/pnas.1300321110.

[52]   Piotr Garstecki et al. "Formation of monodisperse bubbles in a microfluidic flow-focusing device". en. In: *Applied Physics Letters* 85.13 (Sept. 2004), pp. 2649–2651. ISSN: 0003-6951, 1077-3118. DOI: 10.1063/1.1796526. URL: http://aip.scitation.org/doi/10.1063/1.1796526 (visited on 07/29/2022).

[53]   E. Amstad, S. S. Datta, and D. A. Weitz. "The microfluidic post-array device: high throughput production of single emulsion drops". en. In: *Lab on a Chip* 14.4 (2014), pp. 705–709. ISSN: 1473-0197, 1473-0189. DOI: 10.1039/C3LC51213D. (Visited on 08/17/2023).

[54]   Govind V. Kaigala, Robert D. Lovchik, and Emmanuel Delamarche. "Microfluidics in the "open space" for performing localized chemistry on biological interfaces". en. In: *Angewandte Chemie International Edition* 51.45 (Nov. 2012), pp. 11224–11240. ISSN: 14337851. DOI: 10.1002/anie.201201798. URL: http://doi.wiley.com/10.1002/anie.201201798 (visited on 07/18/2019).

[55]   K. C. Bhargava, B. Thompson, and N. Malmstadt. "Discrete Elements for 3D Microfluidics". English. In: *Proceedings of the National Academy of Sciences of the United States of America* 111.42 (Oct. 2014), pp. 15013–15018. ISSN: 0027-8424, 1091-6490. DOI: 10.1073/pnas.1414764111.

[56]   Anthony K. Au et al. "3D-Printed Microfluidics". en. In: *Angewandte Chemie International Edition* 55.12 (Mar. 2016), pp. 3862–3881. ISSN: 14337851. DOI: 10.1002/anie.201504382. URL: https://onlinelibrary.wiley.com/doi/10.1002/anie.201504382 (visited on 10/13/2022).

[57]   Koki Takahashi et al. "Stainless microfluidic probe with 2D-array microapertures". en. In: *AIP Advances* 11.1 (Jan. 2021), p. 015331. ISSN: 2158-3226. DOI: 10.1063/5.0014119. URL: http://aip.scitation.org/doi/10.1063/5.0014119 (visited on 10/13/2022).

[58]   H. S. M. Coxeter. *Regular polytopes*. 3d ed. New York: Dover Publications, 1973. ISBN: 978-0-486-61480-9.

[59]   David J. Gross. "The role of symmetry in fundamental physics". en. In: *Proceedings of the National Academy of Sciences of the United States of America* 93.25 (Dec. 1996), pp. 14256–14259. ISSN: 0027-8424, 1091-6490. DOI: 10.1073/pnas.93.25.14256. URL: https://pnas.org/doi/full/10.1073/pnas.93.25.14256 (visited on 10/13/2022).

[60]   Roya Zandi et al. "Origin of icosahedral symmetry in viruses". en. In: *Proceedings of the National Academy of Sciences of the United States of America* 101.44 (Nov. 2004), pp. 15556–15560. ISSN: 0027-8424, 1091-6490. DOI: 10.1073/pnas.0405844101. (Visited on 08/17/2023).

[61]   E. M. Purcell. "Life at low Reynolds number". English. In: *American Journal of Physics* 45.1 (Jan. 1977), pp. 3–11. ISSN: 0002-9505, 1943-2909. DOI: 10.1119/1.10903.

[62]   Allison P. Berke et al. "Hydrodynamic Attraction of Swimming Microorganisms by Surfaces". en. In: *Physical Review Letters* 101.3 (July 2008), p. 038102. ISSN: 0031-9007, 1079-7114. DOI: 10.1103/PhysRevLett.101.038102. URL: https://link.aps.org/doi/10.1103/PhysRevLett.101.038102 (visited on 04/25/2022).

[63]   Pierre-Alexandre Goyette et al. "Microfluidic multipoles theory and applications". en. In: *Nature Communications* 10.1 (Dec. 2019), p. 1781. ISSN: 2041-1723. DOI: 10.1038/s41467-019-09740-7. (Visited on 07/15/2022).

[64]   Wen-Zhen Fang et al. "Data-Driven Intelligent Manipulation of Particles in Microfluidics". en. In: *Advanced Science* (Dec. 2022), p. 2205382. ISSN: 2198-3844, 2198-3844. DOI: 10.1002/advs.202205382. (Visited on 02/08/2023).

[65]   A. Ashkin et al. "Observation of a single-beam gradient force optical trap for dielectric particles". en. In: *Optics Letters* 11.5 (May 1986), p. 288. ISSN: 0146-9592, 1539-4794. DOI: 10.1364/OL.11.000288. URL: https://opg.optica.org/abstract.cfm?URI=ol-11-5-288 (visited on 10/13/2022).

[66] Junru Wu. "Acoustical tweezers". en. In: *The Journal of the Acoustical Society of America* 89.5 (1991), pp. 2140–2143. ISSN: 0001-4966, 1520-8524. DOI: `10.1121/1.400907`. (Visited on 08/09/2023).

[67] David G Grier. "Optical tweezers in colloid and interface science". en. In: *Current Opinion in Colloid & Interface Science* 2.3 (June 1997), pp. 264–270. ISSN: 13590294. DOI: `10.1016/S1359-0294(97)80034-9`. (Visited on 08/17/2023).

[68] Qiyue Luan et al. "Microfluidic systems for hydrodynamic trapping of cells and clusters". In: *Biomicrofluidics* 14.3 (2020), p. 031502.

[69] Anish Shenoy et al. "Flow Topology During Multiplexed Particle Manipulation Using a Stokes Trap". en. In: *Physical Review Applied* 12.5 (Nov. 2019), p. 054010. ISSN: 2331-7019. DOI: `10.1103/PhysRevApplied.12.054010`. (Visited on 08/09/2023).

[70] The stress distribution is intrinsic to the far-field hyperbolic topology because any offset from the hyperbolic point, such as with a minimal planar extensional flow [18], is equivalent to adding a mean flow that imposes zero stress. For instance, taking that example flow velocity $\mathbf{v} \propto x\hat{x} - y\hat{y}$, the strain rate is found to be $\dot{\gamma} \propto \hat{x}\hat{x} - \hat{y}\hat{y}$. A displaced field, i.e. $\mathbf{v} \propto (x - a_x)\hat{x} - (y - a_y)\hat{y}$ for some physical displacement of the center (a_x, a_y), is trivially seen to separate into the original field with an added mean flow, and the strain rate is identical and likewise invariant.

[71] P. B. Pal. *A physicist's introduction to algebraic structures: vector spaces, groups, topological spaces and more*. Cambridge, United Kingdom: Cambridge University Press, 2019. ISBN: 978-1-108-49220-1 978-1-108-72911-6.

[72] A. J. M. Spencer. *Continuum mechanics*. Longman mathematical texts. London ; New York: Longman, 1980. ISBN: 978-0-582-44282-5.

[73] Mohammad Irfan Hajam and Mohammad Mohsin Khan. "Microfluidics: a concise review of the history, principles, design, applications, and future outlook". In: *Biomaterials Science* (2024).

[74] Shuaizhong Zhang et al. "A concise review of microfluidic particle manipulation methods". In: *Microfluidics and Nanofluidics* 24.4 (2020), p. 24.

[75] Anish Shenoy, Christopher V Rao, and Charles M Schroeder. "Stokes trap for multiplexed particle manipulation and assembly using fluidics". In: *Proceedings of the National Academy of Sciences* 113.15 (2016), pp. 3976–3981.

[76] Junjie Yu et al. "Self-powered droplet manipulation system for microfluidics based on triboelectric nanogenerator harvesting rotary energy". In: *Lab Chip* 21 (2 2021), pp. 284–295. DOI: `10.1039/D0LC00994F`. URL: `http://dx.doi.org/10.1039/D0LC00994F`.

[77] Luming Zhao et al. "Application of nanogenerators in self-powered microfluidic systems". In: *Nano Energy* 123 (2024), p. 109432. ISSN: 2211-2855. DOI: `https://doi.org/10.1016/j.nanoen.2024.109432`. URL: `https://www.sciencedirect.com/science/article/pii/S2211285524001800`.

[78] Chi Zhang et al. "Determining intrinsic potentials and validating optical binding forces between colloidal particles using optical tweezers". In: *Nature Communications* 15.1 (2024), p. 1020.

[79] Anish Shenoy et al. "Flow Topology During Multiplexed Particle Manipulation Using a Stokes Trap". In: *Phys. Rev. Appl.* 12 (5 Nov. 2019), p. 054010. DOI: `10.1103/PhysRevApplied.12.054010`. URL: `https://link.aps.org/doi/10.1103/PhysRevApplied.12.054010`.

[80] D.Q. Mayne et al. "Constrained model predictive control: Stability and optimality". In: *Automatica* 36.6 (2000), pp. 789–814. ISSN: 0005-1098. DOI: `https://doi.org/10.1016/S0005-1098(99)00214-9`. URL: `https://www.sciencedirect.com/science/article/pii/S0005109899002149`.

[81] Ningquan Wang et al. "Closed-loop feedback control of microfluidic cell manipulation via deep-learning integrated sensor networks". In: *Lab Chip* 21 (10 2021), pp. 1916–1928. DOI: `10.1039/D1LC00076D`. URL: `http://dx.doi.org/10.1039/D1LC00076D`.

[82] John K Ousterhout et al. *Tcl: An embeddable command language*. Citeseer, 1989.

[83] Adam Paszke et al. "Pytorch: An imperative style, high-performance deep learning library". In: *Advances in neural information processing systems* 32 (2019).

[84] Aaron Meurer et al. "SymPy: symbolic computing in Python". In: *PeerJ Computer Science* 3 (Jan. 2017), e103. ISSN: 2376-5992. DOI: `10.7717/peerj-cs.103`. URL: `https://doi.org/10.7717/peerj-cs.103`.

[85] Charles R. Harris et al. "Array programming with NumPy". In: *Nature* 585.7825 (Sept. 2020), pp. 357–362. DOI: `10.1038/s41586-020-2649-2`. URL: `https://doi.org/10.1038/s41586-020-2649-2`.

[86] Siu Kwan Lam, Antoine Pitrou, and Stanley Seibert. "Numba: a LLVM-based Python JIT compiler". In: *Proceedings of the Second Workshop on the LLVM Compiler Infrastructure in HPC*. LLVM '15. Austin, Texas: Association for Computing Machinery, 2015. ISBN: 9781450340052. DOI: `10.1145/2833157.2833162`. URL: `https://doi.org/10.1145/2833157.2833162`.

[87] Ryosuke Okuta et al. "CuPy: A NumPy-Compatible Library for NVIDIA GPU Calculations". In: *Proceedings of Workshop on Machine Learning Systems (LearningSys) in The Thirty-first Annual Conference on Neural Information Processing Systems (NIPS)*. 2017. URL: `http://learningsys.org/nips17/assets/papers/paper_16.pdf`.

[88] G. Bradski. "The OpenCV Library". In: *Dr. Dobb's Journal of Software Tools* (2000).

[89] Tobin A. Driscoll and Lloyd N. Trefethen. *Schwarz-Christoffel Mapping*. Cambridge Monographs on Applied and Computational Mathematics. Cambridge University Press, 2002. DOI: `10.1017/CBO9780511546808`.

[90] Kiran Raj M and Suman Chakraborty. "PDMS microfluidics: A mini review". In: *Journal of Applied Polymer Science* 137.27 (2020), p. 48958. DOI: `https://doi.org/10.1002/app.48958`. eprint: `https://onlinelibrary.wiley.com/doi/pdf/10.1002/app.48958`. URL: `https://onlinelibrary.wiley.com/doi/abs/10.1002/app.48958`.

[91] Tao Wang et al. "Fabricating Microstructures on Glass for Microfluidic Chips by Glass Molding Process". In: *Micromachines* 9.6 (2018). ISSN: 2072-666X. DOI: `10.3390/mi9060269`. URL: `https://www.mdpi.com/2072-666X/9/6/269`.

[92] Zhen-Yi Hong et al. "High-speed micro-particle manipulation in a microfluidic chip by directional femtosecond laser impulse". In: *Sensors and Actuators A: Physical* 297 (Oct. 2019), p. 111566. ISSN: 0924-4247. DOI: `10.1016/j.sna.2019.111566`. URL: `https://www.sciencedirect.com/science/article/pii/S0924424719307368` (visited on 03/22/2024).

[93] Chao Liu and Guoqing Hu. "High-Throughput Particle Manipulation Based on Hydrodynamic Effects in Microchannels". en. In: *Micromachines* 8.3 (Mar. 2017). Number: 3 Publisher: Multidisciplinary Digital Publishing Institute, p. 73. ISSN: 2072-666X. DOI: `10.3390/mi8030073`. URL: `https://www.mdpi.com/2072-666X/8/3/73` (visited on 03/22/2024).

[94] K.M. Taute et al. "High-throughput 3D tracking of bacteria on a standard phase contrast microscope". In: *Nature Communications* 6.1 (Dec. 2015). ISSN: 2041-1723. DOI: `10.1038/ncomms9776`. URL: `http://www.nature.com/articles/ncomms9776` (visited on 02/21/2018).

[95] Joseph Gallian. *Contemporary Abstract Algebra*. en. Ed. by Joseph A. Gallian. 10th ed. Chapman and Hall/CRC, Jan. 2021. ISBN: 978-1-00-314233-1. DOI: `10.1201/9781003142331`. (Visited on 02/07/2023).

[96] Philip J. Davis. *Circulant matrices*. Pure and applied mathematics. New York: Wiley, 1979. ISBN: 978-0-471-05771-0.